VILNIUS UNIVERSITY
CENTER FOR PHYSICAL SCIENCES AND TECHNOLOGY

Austėja Diktanaitė

Synthesis and Investigation of the Multicomponent Oxides

DOCTORAL DISSERTATION

Natural Sciences,
Chemistry N 003

VILNIUS 2023

This dissertation was written between 2018 and 2023 at Vilnius University, Faculty of Chemistry and Geosciences.

Academic supervisor:
Dr. Artūras, Žalga (Vilnius University, Natural Sciences, Chemistry – N 003).

This doctoral dissertation will be defended in a public meeting of the Dissertation Defense Panel:
Chairman – Assoc. Prof. Dr. Justina Gaidukevič (Vilnius University, Natural Sciences, Chemistry – N 003).

Members:
Assoc. Prof. Dr. Inga Grigaravičiūtė (Vilnius University, Natural Sciences, Chemistry – N 003),
Dr. Olga Kizinievič (Vilnius Gediminas Technical University, Technological Sciences, Materials Engineering – T 008)
Dr. Anatoli Popov (University of Latvia, Natural Sciences, Physics – P 002).
Prof. Habil. Dr. Rimantas Ramanauskas (Center for Physical Sciences and Technology, Natural Sciences, Chemistry – P 002).

The dissertation shall be defended at a public meeting of the Dissertation Defense Panel at 14 (hour) on 1st of December, 2023 at the Inorganic Chemistry Auditorium (141) at the Faculty of Chemistry and Geosciences of Vilnius University.
Address: Naugarduko str. 24, LT-03225, Vilnius, Lithuania, tel. +370 5 219 3108; e-mail: info@chgf.vu.lt

The text of this dissertation can be accessed at the Library of Vilnius University and at the Library of FTMC, as well as on the website of Vilnius University: www.vu.lt/lt/naujienos/ivykiu-kalendorius

VILNIAUS UNIVERSITETAS
FIZINIŲ IR TECHNOLOGIJOS MOKSLŲ CENTRAS

Austėja Diktanaitė

Daugiakomponenčių oksidų sintezė ir tyrimas

DAKTARO DISERTACIJA

Gamtos mokslai,
Chemija N 003

VILNIUS 2023

Disertacija rengta 2018 – 2023 metais Vilniaus universiteto Chemijos ir geomokslų fakultete.

Mokslinis vadovas:
Dr. Artūras Žalga (Vilniaus universitetas, gamtos mokslai, chemija – N 003).

Pirmininkė:
Doc. dr. Justina Gaidukevič (Vilniaus universitetas, gamtos mokslai, chemija – N 003).

Gynimo taryba:
Doc. dr. Inga Grigaravičiūtė (Vilniaus universitetas, gamtos mokslai, chemija – N 003),
Dr. Olga Kizinievič (Vilniaus Gedimino technikos universitetas, technologijos mokslai, medžiagų Inžinerija – T 008),
Dr. Anatoli Popov (Latvijos universitetas, gamtos mokslai, fizika – P 002),
Prof. habil. dr. Rimantas Ramanauskas (Fizinių ir technologijos mokslų centras, gamtos mokslai, chemija – P 002).

Disertacija ginama viešame Gynimo tarybos posėdyje 2023 m. gruodžio mėn. 1 d. 14 val. Vilniaus universiteto Chemijos ir geomokslų fakulteto Neorganinės chemijos auditorijoje (141). Adresas: Naugarduko g. 24, LT-03225, Vilnius, Lietuva, tel. +370 5 219 3108; el. paštas info@chgf.vu.lt.

Disertaciją galima peržiūrėti Vilniaus universiteto ir FTMC Chemijos instituto bibliotekose ir VU interneto svetainėje adresu: https://www.vu.lt/naujienos/ivykiu-kalendorius

ABSTRACT

Multicomponent oxide materials have become an inseparable part of our everyday life. Over the last few decades, many researchers have investigated multicomponent oxide materials to better understand their properties and apply them to create a more ecological, affordable, and safer world. $M^I AlMo_2O_8$, $Li_{3x}La_{2/3-x}TiO_3$, and $Bi_2O_3 - V_2O_5$ are the perfect example of these materials.

$M^I AlMo_2O_8$ alkali metal aluminum molybdates (where M = Li, Na, K, Rb, and Cs) have not been investigated as widely as the other two compounds, but they did attract promising attention due to their ferro elastic phase transitions and ability to be hosts for rare-earth ions and transition metals. These compounds may be used for tunable lasers and optical instruments where high accuracy is required. In contrast, lithium lanthanum titanates ($Li_{3x}La_{2/3-x}TiO_3$) of an ABO_3 perovskite structure with cation deficiency at the A-sites exhibit very high ionic conductivity and have a wide range of known possible applications. Starting with everyday items, such as cell phones and electric car batteries, followed by big industries like oil drilling and food production, and ending with a couple of unexpected applications – ocean exploration and nuclear equipment. Bismuth vanadate compounds have been greatly associated with green technology - water splitting in particular - due to their relatively low-cost synthesis, excellent durability in various environments, and non-toxicity. Interestingly, bismuth vanadate materials can also be used in medicine due to their strong antibacterial and anti-viral properties. These applications are only possible if we understand and control the synthesis and properties of these ceramics.

The multicomponent oxides with the general formulas of $M^I AlMo_2O_8$, $Li_{3x}La_{2/3-x}TiO_3$, and $Bi_2O_3 - V_2O_5$ have been prepared by the aqueous tartaric acid-assisted sol-gel preparation technique. While many studies usually explore EDTA or citric acid use in sol-gel synthesis, in this study, a less common reagent has been chosen. Tartaric acid has been selected as the chelating agent that interacts with the ligand during both dissolution in water, and sol-gel formation. Tartaric acid has a lot of useful properties, such as decomposition at low temperatures, leaving behind minimal carbon-containing residues, and helping to maintain the pH of the solution. And, most importantly, tartaric acid is produced from natural resources such as grapes or bananas, and it's low-cost and not harmful to humans or the environment.

To understand the thermal decomposition of the prepared materials, thermogravimetric and differential scanning calorimetry (TGA-DSC) analysis

was completed using STA 6000 Perkin-Elmer instrument. X-ray diffraction (XRD) patterns were recorded in the air at room temperature by employing a powder X-ray diffractometer Rigaku MiniFlex II. The Rietveld refinement of the obtained patterns was completed to evaluate the crystalline phase composition. The scanning electron microscopes (SEM) Hitachi SU-70 and Hitachi TM3000 were used to study the surface morphology and microstructure of the obtained ceramic samples, and energy-dispersive X-ray spectroscopy (EDS) was applied to determine the elemental composition of $Bi_2O_3 \cdot V_2O_5$ ceramics. Perkin-Elmer Frontier FT-IR spectrometer was used to estimate the characteristic vibrations of the functional groups.

The thermal analysis of multicomponent oxide tartrate gel precursors proved a few significant points: 1. The formation of the obtained ceramics is highly dependent on the molar ratio of the initial reactants in the reaction mixture; 2. The final oxidation of metal tartrate residues highly depends on the atmosphere environment; 3. The decomposition of tartaric acid is seen up to 300 °C of temperature and occurred independently in either the oxidative, or inert environment; 4. The deficiency of the tartaric acid during the sol-gel process strongly affects the homogeneity of the final gel precursor. The XRD patterns and FT-IR transmittance spectra both seconded the previously made statement that the final composition of the crystalline phases highly depends on the molar composition of the initial reagents. It also showed that the number of impurities can be decreased by increasing the heat-treatment temperature. SEM micrographs corresponded to the XRD data and showed some irregular shape formations, which are most likely the result of the decomposition of unreacted tartaric acid. All three multicomponent oxide tartrate gels did not exhibit well-seen cracks or hollows. The electrical conductivity evaluation confirmed that the ionic conductivity is majorly affected by the crystalline structure of the materials.

The data obtained correspond with each other well and give a better understanding of the synthesized materials and their potential use. It also shows that reaction conditions, such as temperature, the molar ratio of initial materials, and the amount of chelating agent can highly influence the final product, its structure, and, therefore, its characteristics.

TABLE OF CONTENTS

LIST OF ABBREVATIONS

COD	Crystallography open database
DSC	Differential scanning calorimetry
EDS	Energy-dispersive X-ray spectroscopy
FTIR	Fourier-transform infrared spectroscopy
Hep2C	Human epidermoid carcinoma cells; type 2; clone C
HRTEM	High-resolution transmission electron microscopy
ICSD	The inorganic crystal structure database
LLTO	Lithium lanthanum titanate
SEM	Scanning electron microscopy
SG	Sol-gel method
SS	Solid-state method
TA	Tartaric acid
$TCID_{50}$	Tissue culture infectious dose; 50% tissue culture
TGA	Thermogravimetric analysis
TSSG	Top-seeded solution growth
USP	Ultrasonic spray pyrolysis
XRD	X-ray diffraction analysis

INTRODUCTION

It would be hard to find an industry that would not, at some point, benefit from multicomponent crystalline oxides. Cell phones [1, 2], laptops [3], electric and hybrid cars [4], pressure sensors, optical lasers [5], food fermentation [6], pH indicators [7], gas sensors [8], water-splitting [9], ocean exploration [10], medicine [11], or even nuclear equipment [10] – these are only a few possible applications of lithium aluminium molybdate oxides, lithium lanthanum titanium oxides, and bismuth vanadium oxides. These materials play a major role in many different scientific fields and industries due to their unique structure and superior properties, making our everyday lives safer, more affordable, and more sustainable.

Currently widely used lithium primary batteries, containing flammable solvents and contributing to environmental waste, could potentially be replaced by 5-10 times longer lasting [12] and safer batteries [13], improved by lithium lanthanum titanium oxides (LLTO). LLTO of a perovskite structure have a very high ionic conductivity and low activation energy [14], which makes them well-fitting for longer lasting, safer energy storing device production. Their chemical stability and the ability to withstand harsh pH [7] conditions allow LLTO materials to be used in the oil drilling industry to detect hydrogen sulphide gas and could prevent fatalities that had happened in the recent past [15].

With the world population reaching 8 billion [16], finding ways to produce clean, renewable energy has become an unavoidable task. Wind and solar energy production are efficient ways to produce renewable energy, however, they are still harmful to the environment – wind turbines are known to cause fatalities to wildlife [17], while solar energy production comes with solvent, oil, and hazardous waste [18]. Monoclinic scheelite $BiVO_4$ could be used as a photoanode to solve these issues by producing renewable energy via water-splitting [9]. Due to its small energy gap [19], good conductivity [1], and great chemical stability [20], bismuth vanadium oxide could play a key role in producing clean, renewable energy that does not negatively impact the environment.

Alkali metal aluminium molybdates, while not yet widely explored, show a lot of potential in optical applications due to their optical and ferroelastic properties [21, 22]. Doped with rare-earth ions, they have the potential to be used in tunable laser applications [23], when high accuracy and repeatability is required.

These multicomponent oxides present opportunities to highly improve our lives, however, this is only possible if we understand their structure, properties, and the syntheses behind them.

The main aim of this Ph. D. thesis includes the application of an aqueous sol-gel preparation technique for the preparation of the homogeneous metal tartrate gel precursors and the characterization of the different single-phase multicomponent oxides. Given the limited publications on this synthesis used for $LiAlMo_2O_8$, $Li_{0.35}La_{0.55}TiO_3$ and $5Bi_2O_3 \cdot V_2O_5$ preparation, the corresponding tasks were formulated as follows:

1. The use of the aqueous tartaric acid-assisted sol-gel synthesis method for the preparation of three different multicomponent systems: $LiAlMo_2O_8$, $Li_{0.35}La_{0.55}TiO_3$ and $5Bi_2O_3 \cdot V_2O_5$.
2. The design of the possible decomposition mechanism for tartaric acid and detailed investigation of the thermal decomposition of the corresponding metal tartrate gel precursors using thermogravimetric and differential scanning calorimetric analysis.
3. The observation of the formation of the final multicomponent metal oxides crystalline phases by applying the X-Ray diffraction method.
4. The determination of the surface morphology of the obtained ceramics heated-treated at different temperatures by scanning electron microscopy.
5. The demonstration and validation of the physical properties for the corresponding crystalline composition of the obtained ceramics by impedance spectroscopy.

Statements to be defended:

1. For the first time the aqueous tartaric acid-assisted sol-gel synthesis technique was successfully proposed for the preparation of $LiAlMo_2O_8$, $Li_{0.35}La_{0.55}TiO_3$, and $5Bi_2O_3 \cdot V_2O_5$ multicomponent oxides.

2. TGA–DSC analysis is a powerful and suitable tool for both the investigation of decomposition mechanisms of Li–Al–Mo–O, Li–La–Ti–O and Bi–V–O tartrate gel precursors and the estimation of the crystallization processes of the final $LiAlMo_2O_8$, $Li_{0.35}La_{0.55}TiO_3$, and $5Bi_2O_3 \cdot V_2O_5$ ceramic materials.

3. The nature of the complexing agent is the critical stage in the sol-gel process, which strongly influences the morphological, structural, and electrical properties of obtained compounds.

4. The heat-treatment has significant influence on both the thermal decomposition of synthesized gel precursors and crystallization of the final ceramics.

5. The combination of thermal analysis and different characterization techniques is a useful tool that enables the demonstration of interesting relations between chemical and physical properties of obtained ceramics.

1. LITERATURE OVERVIEW

This chapter of the thesis briefly reviews the structural regularities of the corresponding multicomponent oxides, the possibilities of the syntheses techniques, and the characteristics of the obtained properties.

1.1. $M^IAlMo_2O_8$, $Li_{3x}La_{2/3-x}TiO_3$ and $Bi_2O_3 – V_2O_5$ ceramics and their crystalline structures

For decades, ceramic materials have been given a lot of interest in many different industries and have become essential in our everyday life. From cell phone batteries to life-saving gas sensors, ceramic materials have shown a lot of potential to replace the currently used more expensive and harmful alternatives, due to their powerful conducting abilities, great stability in high temperatures and air, substantial hydrophobic properties, and unique crystalline structures. $M^IAlMo_2O_8$, $Li_{3x}La_{2/3-x}xTiO_3$, and $Bi_2O_3 – V_2O_5$ are great examples of such ceramics, and they share certain similarities in their behavior. The crystal structure of these ceramics plays a key role in their properties and potential application.

$M^IAlMo_2O_8$ double molybdates (M = Li, Na, K, Rb, and Ce) have monoclinic, triclinic, and hexagonal lattice crystal structures [24-26]. $LiAlMo_2O_8$ compounds have the triclinic crystal structure with the space group P-1, with the LiO_5 trigonal bipyramid and MoO_4 tetrahedra, connected by the shared oxigen atoms with the AlO_6 octahedra [27]. $NaAlMo_2O_8$ crystallizes into a monoclinic crystal lattice that has a C12/c1(15) space group designation. $KAlMo_2O_8$, $RbAlMo_2O_8$, $CsAlMo_2O_8$ crystallize into hexagonal lattice crystal structures [28-30].

Lithium lanthanum titanate ($Li_{3x}La_{2/3-x}TiO_3$; LLTO) of an ABO_3 perovskite structure with cation deficiency at the A-sites is a very powerful conductor with a high bulk ionic conductivity ($\sim 10^{-3}$ Scm^{-1} at room temperature) [31]. The ionic conductivity highly depends on the size of the A-site ion cation, lithium and vacancy concentration, and the nature of the B – O bond. In this case, lanthanum is chosen as the A-site, but if it were replaced by some other rare earth metal that has a smaller ionic radius than La, then the ion conductivity of the structure would be much lower. The type of the perovskite structure also influences the ionic conductivity. For example, the tetragonal structure shows lower conductivity than the same bulk composition cubic structure [32]. Perovskite structure contributes to their ferroelectric properties, which is also why LLTO compounds are considered another good

substitution for solid-state batteries, which are safer than currently used standard lithium-ion batteries [33].

$Bi_2O_3 – V_2O_5$ has a fluorite-type superstructure and has four structure types (α-phase, δ-phase, β-phase, and γ-phase). δ-phase of Bi_2O_3 is considered to be one of the best conductors because of its oxygen vacancies. In comparison, α-phase has very little ionic conductivity [34]. The layered structure of $Bi_2O_3 – V_2O_5$ provides migration pathways for the charge oxygen ions or vacancies within the material [35]. The modulation of electrical conductivity and ion transport is allowed by increasing the concentration of V_2O_5 due to the phase transition of $BiVO_4$ from monoclinic scheelite type to that of tetragonal scheelite type [36].

Despite having rather different crystal structures, $M^ILaMo_2O_8$, $Li_{3x}La_{2/3−x}TiO_3$, and $Bi_2O_3 – V_2O_5$ ceramics share some similarities. The presence of corner-sharing octahedra in these three types of ceramics provides structural stability and efficient ion transport. In addition, they all exhibit an ability to modulate their electrical properties by controlling composition, doping, and oxidation/reduction states. $Li_{3x}La_{2/3−x}TiO_3$ and $Bi_2O_3 – V_2O_5$ ceramics have pathways for the migration of charge carriers due to their layered structure, which improves electrical conductivity. By understanding and controlling the crystal structure of these ceramics, we can influence their properties and improve their applications in many industries.

1.1.1. Crystal structures of $M^IAlMo_2O_8$ and $Li_3AlMo_3O_{12}$ compounds

The general formula for lithium, sodium, potassium, rubidium, and cesium aluminum molybdates is $MAlMo_2O_8$ (M = Li, Na, K, Rb, and Ce), nonetheless, the arrangement of individual atoms in the crystal structure is distinguishable. Potassium and cesium aluminum molybdates crystallize into a trigonal structure, $NaAlMo_2O_8$ – monoclinic, $RbAlMo_2O_8$ – hexagonal, while $LiAlMo_2O_8$ is characterized by an irregular triclinic elementary cage in the crystal structure. The trilateral oxide $Li_3AlMo_3O_{12}$ crystallizes into a crystalline compound with an orthorhombic elementary lattice system. A brief overview of the crystal structures of these compounds will be given, which were used to identify the resulting crystalline compounds by X-ray diffractograms.

Lithium aluminum molybdate ($LiAlMo_2O_8$) crystallizes into a triclinic structure that has a P–1(2) space group designation. The space group notation P–1(2) represents the lattice system, crystallographic system, and atomic

distribution. In this case, Fig. 1 shows the unit cell of the triclinic crystal lattice of $LiAlMo_2O_8$ [37].
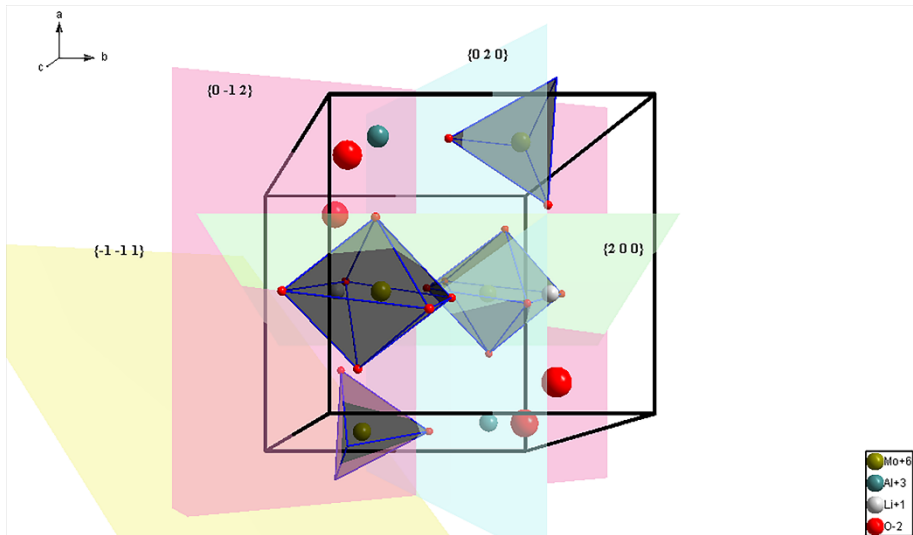
Fig. 1 Triclinic crystal structure for $LiAlMo_2O_8$ composition [37]

The parameters of the triclinic lattice are determined by the general notation: $a \neq b \neq c$; $\alpha \neq \beta \neq \gamma \neq 90^o$, where a, b, and c are the lattice parameters and α, γ and β are the angles between them. For $LiAlMo_2O_8$ a=7.10(3) Å, b = 7.25(5) Å, c = 6.67(5) Å, α = 111.0(5) °, β = 105.0(5) °, γ = 90.0(5) ° [37].

The most intense crystal planes corresponding to this lattice presented in the triclinic unit cell of $LiAlMo_2O_8$ are also shown in Fig. 1, corresponding to the amount of certain crystallographic planes estimated by the intensity of their peaks. The more intense the peak is, the more corresponding planes are in the crystal lattice.

Lithium aluminium molybdate corresponds to the composition of the $Li_3AlMo_3O_{12}$ compound, which crystallizes into an orthorhombic crystal structure with the Pnma(62) space group designation. This multicomponent oxide is an example of the well known lyonsite structure type, the general formula of which can be written as $A_{16}B_{12}O_{48}$. Because this structure can accomodate cationic mixing as well as cationic vacancies, a wide range of chemical compositions can adopt this structure type. In this case, Fig. 2 shows the unit cell of the orthorhombic crystal lattice for the $Li_3AlMo_3O_{12}$ crystalline compound [38]. The parameters of the orthorhombic lattice are determined by the general notation: $a \neq b \neq c$; $\alpha = \beta = \gamma = 90^o$, where a, b, and c are the lattice parameters and α, γ, and β are the angles between them. For example, $Li_3AlMo_3O_{12}$ the parameters are a = 5.0372 Å, b = 10.3200 Å, c = 17.2720 Å

[39]. The orthorhombic crystal structure of lithium aluminum molybdate (Li$_3$AlMo$_3$O$_{12}$) is significantly more regular compared to LiAlMo$_2$O$_8$, therefore, when measuring the diffraction, the number of characteristic peaks recorded is also lower.
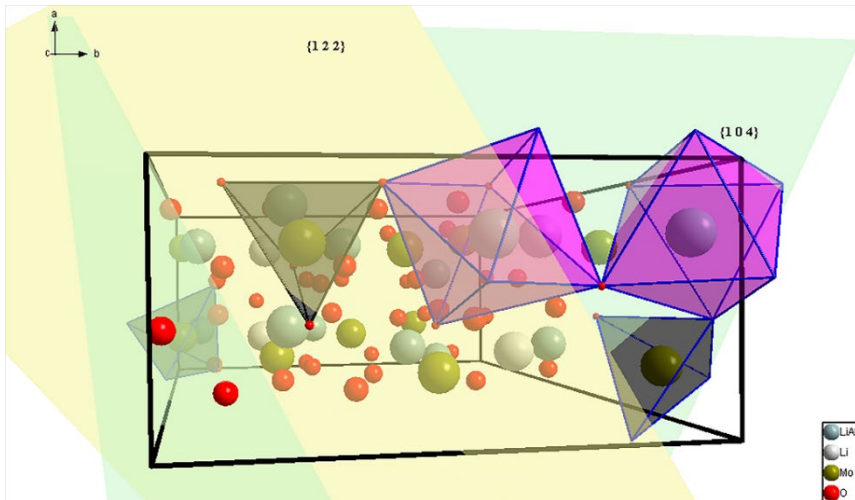
Fig. 2 Orthorhombic crystal structure for Li$_3$AlMo$_3$O$_{12}$ composition [38]

Sodium aluminum molybdate (NaAlMo$_2$O$_8$) crystallizes into a monoclinic crystal lattice that has a C12/c1(15) space group designation. The unit cell of the monoclinic crystal lattice of NaAlMo$_2$O$_8$ is presented in Fig. 3 [40].
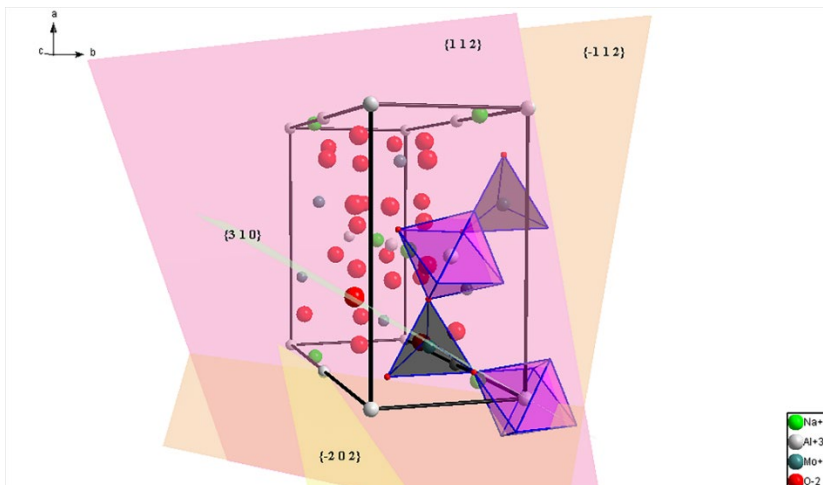
Fig. 3 Monoclinic crystal structure for NaAlMo$_2$O$_8$ composition

The parameters of the monoclinic lattice are determined by the general notation: $a \neq b \neq c$; $\alpha = \beta = \gamma = 90^{\circ}$, where a, b, and c are the lattice parameters and α, γ, and β are the angles between them. For $NaAl(MoO_4)_2$, the unit-cell parameters $a = 9.59$ Å, $b = 5.37$ Å, $c = 13.14$ Å, and $\beta = 90.1^{\circ}$ were reported by Klevtsov et al. in 1975 [41].

The crystal structure of $NaAlMo_2O_8$ is formed by infinite sheets composed of AlO_6 octahedra, corner-linked to slightly distorted MoO_4 tetrahedra (Figs. 4 and 5).
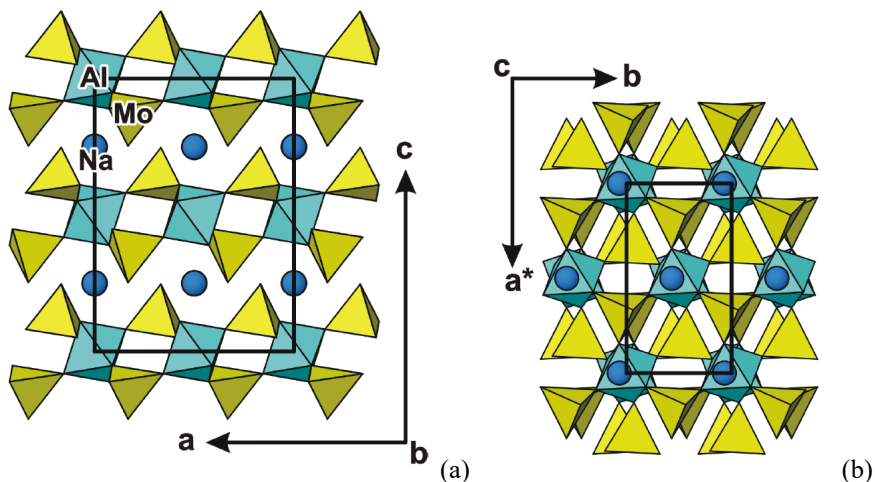
Fig. 4 The layered crystal structure of $NaAlMo_2O_8$ in views (a) along [010] and (b) along [001]. AlO_6 octahedra are corner-connected to MoO_4 tetrahedra to form sheets separated by eight-coordinated Na atoms (dark-blue spheres). The pseudo-orthorhombic unit cell is outlined [40]
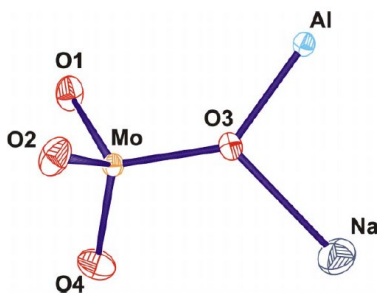
Fig. 5 View of the seven atoms in the asymmetric unit of $NaAlMo_2O8$, shown with ellipsoids at the 70% probability level [40]

These sheets are stacked parallel to (001) and are separated from each other by eight-coordinated interlayer Na atoms (Fig. 4). Average Na–O, Al–O and Mo–O bond lengths are 2.648, 1.890, and 1.762 Å, respectively [40].

Potassium aluminum molybdate ($KAlMo_2O_8$) crystallizes in a trigonal/rhombohedral crystal lattice, which has the P–3m1(164) space group designation. Fig. 6 shows the unit cell of the rhombohedral crystal lattice of $KAlMo_2O_8$ [42].
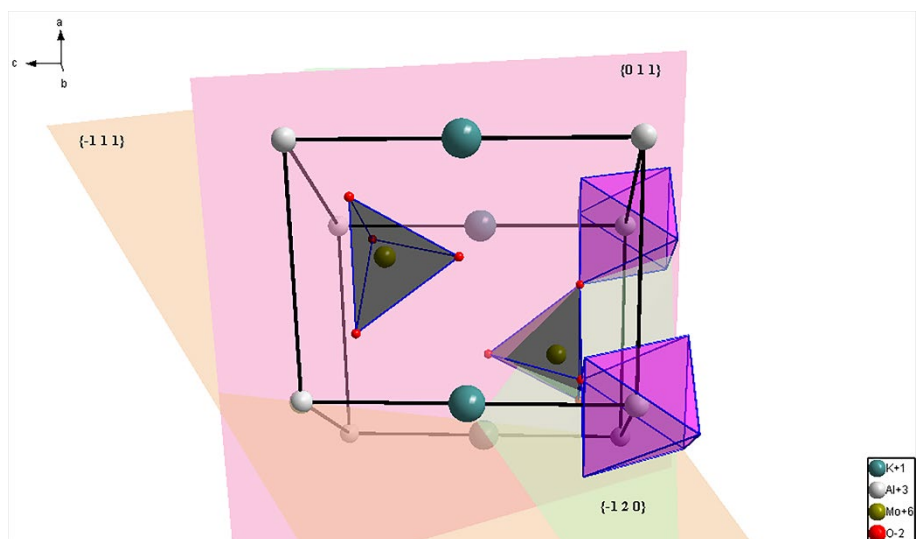
Fig. 6 Trigonal/rhombohedral crystal structure for $KAlMo_2O_8$ composition

The parameters of the rhombohedral lattice are determined by the general notation: $a = b = c$; $\alpha = \beta = \gamma \neq 90°$, where a, b, and c are the lattice parameters and α, γ, and β are the angles between them. For example, the parameters of $KAlMo_2O_8$ are a=5.545(3) Å, c=7.070(5) Å, $\alpha = \beta = 90°$, $\gamma = 120°$ [42].

Like potassium aluminum molybdate, the crystal structure of $RbAlMo_2O_8$ and $CsAlMo_2O_8$ phases is described by the P–3M1(D_{3d}^3) space group with one formula per unit cell. The trigonal unit cell dimensions are: a=5.542 Å and c=7.490 Å for $RbAlMo_2O_8$ and a=5.551 Å and c=8.037 Å for $CsAlMo_2O_8$ [43]. These structures consists of $[AlMo_2O_8^-]_n$ layers perpendicular to the trigonal c-axis with the either rubidium or caesium cations between the layers. Each layer is built up from MoO_4 tetrahedra and AlO_6 octahedra; each octahedron shares its six corners with six MoO_4 tetrahedra. Fig. 7 shows the unit cell of the rhombohedral crystal lattice of $CsAlMo_2O_8$, which is uniform to $KAlMo_2O_8$ compound [44].
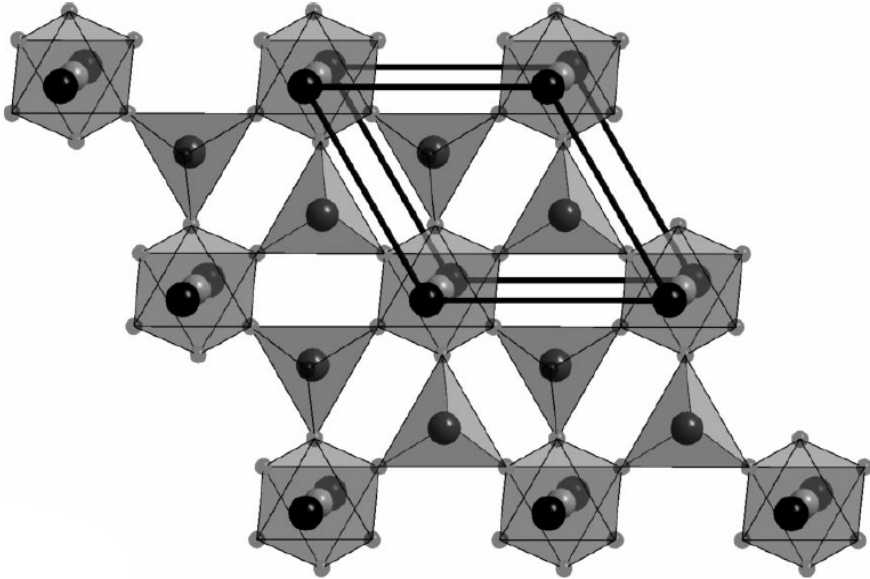
Fig. 7 View of CsAl(MoO₄)₂, approximately down the c axis [44]

In consonance with this data, it can be stated that $KAlMo_2O_8$, $RbAlMo_2O_8$, $CsAlMo_2O_8$ crystallize into hexagonal elementary lattice crystal structures, while lithium aluminum molybdates and sodium aluminum molybdates are more identified by more deviating structures: triclinic and monoclinic.

1.1.2. Overview of lithium lanthanum titanate crystalline phases

In recent years, the study of the alkaline earth titanates and many other compounds with a similar perovskite structure has aroused much interest [45]. The field of the lithium ion-conducting materials has been widely studied because of their potential applications for solid electrolytes in high energy batteries and other electrochemical devices [46].

1.1.2.1. $Li_{0.3}La_{0.567}TiO_3$ crystal structure

$Li_{0.3}La_{0.567}TiO_3$ is a perovskite-type oxide with the space group determined to be I4/mcm. At ambient temperature, $Li_{0.3}La_{0.567}TiO_3$ has the tetragonal perovskite superstructure and $\sqrt{2}a_p$ x $\sqrt{2}a_p$ x $\sqrt{2}a_p$ lattice, the parameters of which are: a = 5.48027 Å, c = 7.75591 Å, Z = 4. The corresponding unite cell is presented in Fig. 8. At approximately 600 °C, the unit cells change into a_p x a_p x a_p cells, and the superlattice reflections disappear [47].
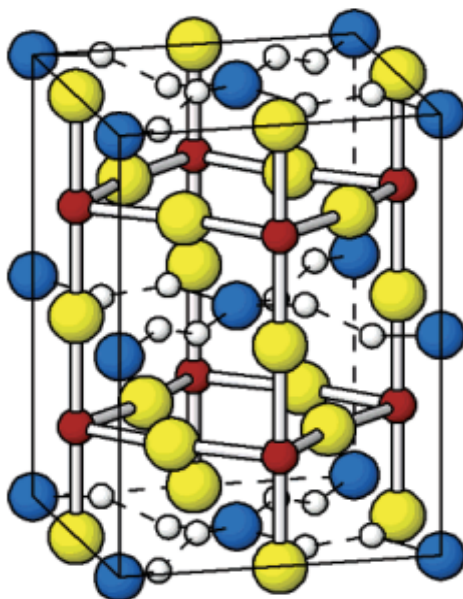
Fig. 8 Unit cell of the I4/mcm structure of $Li_{0.3}La_{0.567}TiO_3$ [47]
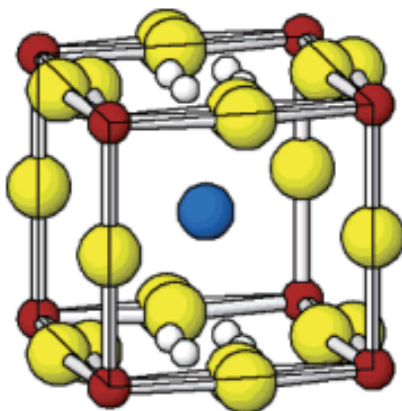
Fig. 9 Unit cell of the P4/mmm structure of $Li_{0.3}La_{0.567}TiO_3$ at 650 °C [47]

The differences between these lattices are reflected by comparing Figs. 8 and 9. Thus, at 650 °C degrees, a tetragonal pseudo-cubic P4/mmm structure was determined, with the unit cell parameters of a = 3.89644 Å, c = 3.89748 Å, and Z = 1. This indicates that the crystal structure properties of $Li_{0.3}La_{0.567}TiO_3$ highly depend on the thermal conditions [47].

1.1.2.2. $Li_{20}La_{24}Ti_5O_{56}$ crystal structure

$Li_{20}La_{24}Ti_5O_{56}$ is a highly complex perovskite structure (Fig. 10), which has a strong tetragonal sub-cell, which parameters are a = 13.244 Å, c = 7.463 Å, and it has the space group of P4/mbm [48].
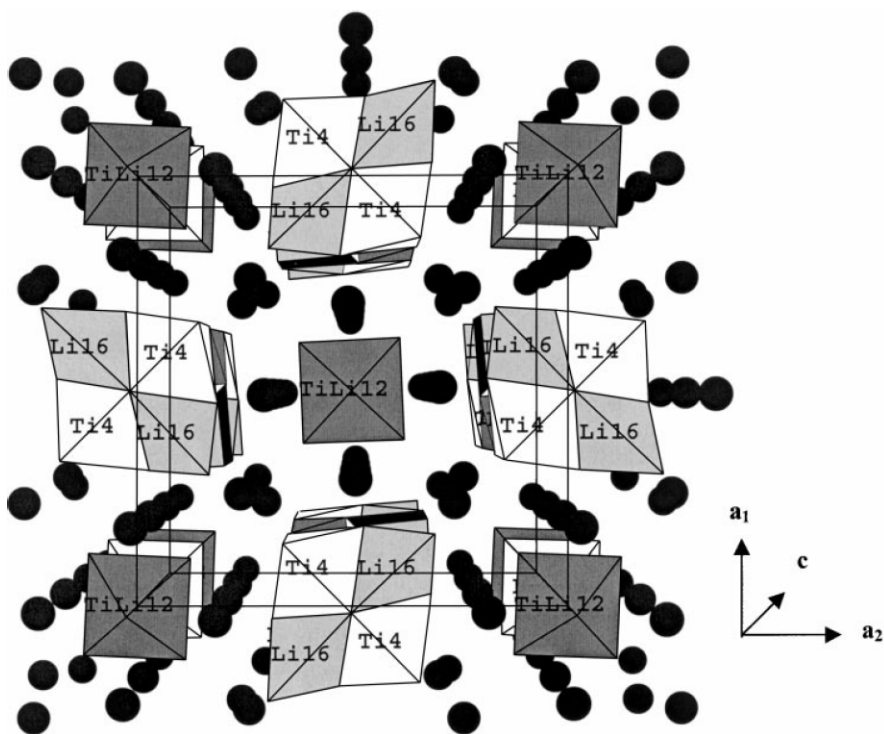
Fig. 10 Perspective view down [001] of $Li_{20}La_{24}Ti_5O_{56}$ with Ti and Li polyhedra indicated [48]

The sub-cell has two alternating columns: a perovskite-like structure with lithium and titanium in alternating octahedral sites, and another structure – half of which is occupied in pairs by lithium, and the other half of tetrahedral

sites collapse and contains either a single octahedral site occupied by titanium, or a single tetrahedral site occupied by lithium [48].

1.1.2.3. $Li_{0.16}La_{0.62}TiO_3$ crystal structure

$Li_{0.16}La_{0.62}TiO_3$ is a perovskite-type of structure, which has an orthorhombic unit with a space group of Cmmm. This structure is similar to the other perovskite compounds but has the presence of lanthanum and lithium ions in the crystal lattice. The structure has a TiO_6 octahedra that is tilted along the b-axis, lanthanum along the c-axis, and lithium in two positions of the A-site. The crystal structure of $Li_{0.16}La_{0.62}TiO_3$ is shown in Fig. 11 [49].
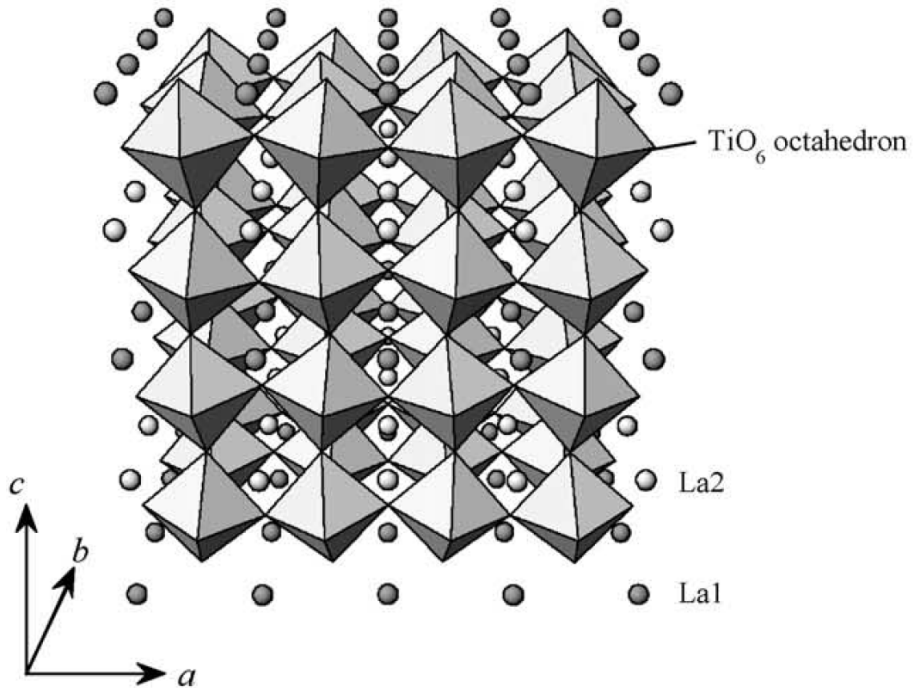
Fig. 11 Crystal structure of $Li_{0.16}La_{0.62}TiO_3$ from the perspective of the TiO_6 octahedral framework [49]

The superstructure has the parameters of $a \approx 2a_p \times b \approx 2a_p \times c \approx 2a_p$. compound has a layered perovskite-type structure consisting of the La-rich (001) La1–O1 layer, the (004) Ti–O layer, and the La-deficient (002) La2–O2 layer, Ti–O layer, and (3) the La-deficient (002) La2–O2 layer. The La-rich

La1–O1 and La-deficient La2–O2 layers are alternatively arranged along the c axis, while the TiO_6 octahedron has anti-phase tilting along the b axis [50].

Figure 12 also shows the crystal structure of $Li_{0.16}La_{0.62}TiO_3$ at room temperature depicted using the refined crystal parameters. The Li cation is located at the Wycoff $2c$ site of the *Cmmm* structure: $^1/_2$, 0.0, ½. Since the Li cations are not located at the $4j$ A-site proposed in the literature but at the $2c$ site, the chemical formula of the title compound is not $(La_{0.62},Li_{0.16},(Va_{A\text{-site}})_{0.22})_{A\text{-site}}TiO_3$ but $(La_{0.62},(Va_{A\text{-site}})_{0.38})_{A\text{-site}}(Li_{0.16},(Va_{2c})_{0.09})_{2c}TiO_3$. Here $Va_{A\text{-site}}$ denotes the vacancy at the A-site. $(La_{0.62},Li_{0.16},(Va_{A\text{-site}})_{0.22})_{A\text{-site}}$ means that the La atom, Li atom, and $Va_{A\text{-site}}$ exist at the A-site of the pseudo ABO_3 perovskite-type structure and their occupancies are 0.62, 0.16, and 0.22, respectively [50].

La1-O1 layer
(001) plane

Ti-O layer

La2-O2 layer
(002) plane

Ti-O layer

La1-O1 layer
(001) plane

2 Å
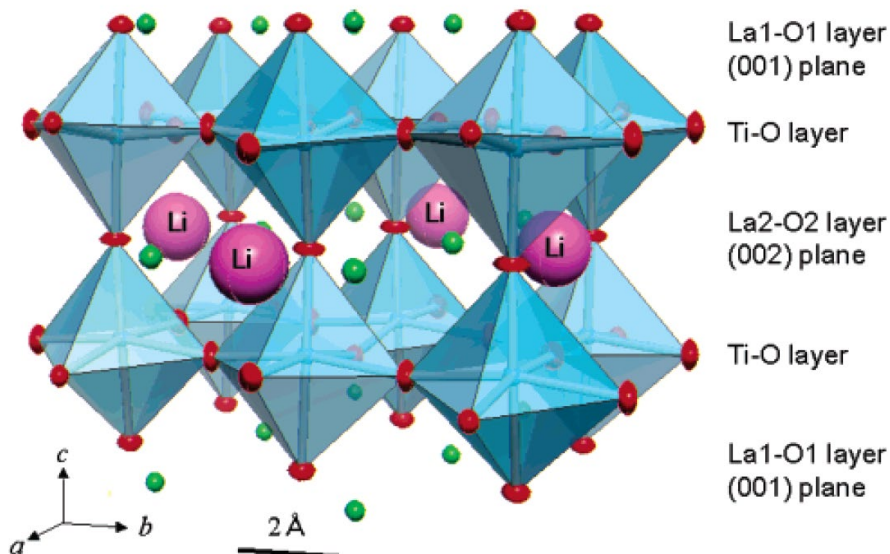
Fig. 12 Crystal structure of the layered perovskite-type lanthanum titanate $Li_{0.16}La_{0.62}TiO_3$ depicted using crystal parameters obtained by the Rietveld analysis of the neutron-diffraction data measured at room temperature. The pink, green, and blue spheres and red ellipsoids denote Li, La, Ti, and oxygen ions, respectively. The blue square is a TiO_6 octahedron [50]

The large atomic displacement parameter of the Li cation indicates the positional disorder and suggests its diffusion. The Li cations are located on the (002) La2–O2 layer (Fig. 12), suggesting that the Li cations two-dimensionally diffuse on the La deficient layer [50].

1.1.2.4. Li$_{1/3}$LaTi$_{2/3}$O$_3$ crystal structure

The system La$_2$O$_3$–Li$_2$O–TiO$_2$ has received considerable interest because it contains the perovskite solid solution of stoichiometry Li$_{1/2-3x}$La$_{1/2+x}$TiO$_3$ which has an extremely high lithium ion conductivity, optimised at $\sim 10^{-3}$ ohm^{-1} cm^{-1} at 25 °C for $x \sim 0.08$. An additional phase, that is also believed to be perovskite related, of stoichiometry Li$_{1/3}$LaTi$_{2/3}$O$_3$ has been reported. Li$_{1/3}$LaTi$_{2/3}$O$_3$ has monoclinic perovskite structure, where lanthanum occupies 9-coordinate A sites, and the B sites contain either titanium alone, or a disordered mixture of lithium and titanium (ratio 2:1). The crystal structure projection of the ab plane is shown in Fig. 13 [51].
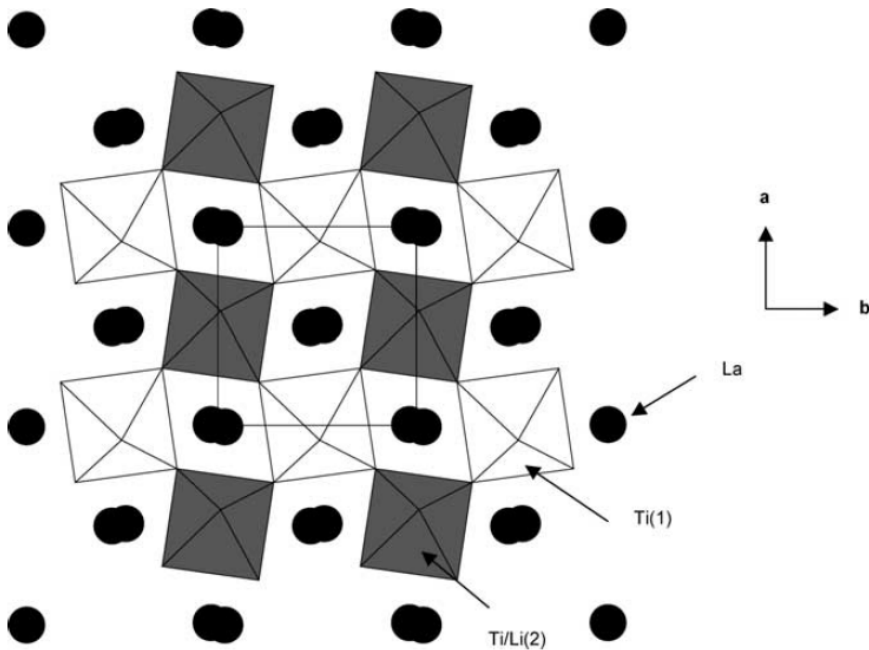
Fig. 13 Crystal structure projection for composition of Li$_{1/3}$LaTi$_{2/3}$O$_3$ [51]

The parameters of the structure are determined by these values: a = 5.5639 Å, b = 5.5688 Å, c = 7.8490 Å, β = 89.834°. The space group is P21/c [51].

At temperatures between 1175 °C and 1185 °C, the 1:2 ordered structure was examined to transform directly into a disordered perovskite and have orthorhombic cell with a space group of Pbnm. The ordered form of Li$_{1/3}$LaTi$_{2/3}$O$_3$ was recovered by annealing at 1100-1150 °C. The ordered structure also seems to depend on the excess of lithium – additionally adding

10% of Li when preparing $Li_{1/3}LaTi_{2/3}O_3$ has shown to cause the disorder of the perovskite product [52].

1.1.2.5. $Li_{0.18}La_{0.61}TiO_3$ crystal structure

$Li_{0.18}La_{0.61}TiO_3$ has an orthorhombic double perovskite structure ($2a_p$, $2a_p$, $2a_p$) with a space group of Cmmm. At low temperature, lanthanum and vacancy rich planes alternate along [001] direction, while the TiO_6 octahedra are tilted around the b-axis. At higher temperature, approximately 773 K, the octahedral tilting decreases, and the more orderly structure forms [53]. The corresponding structural changes are illustrated in Fig. 14. The octahedral distortion and the octahedral tilting along the b-axis is clearly observed in the low temperature phase. Differences on La coordination in z/c = 0 (fully occupied) and 0.5 (partially occupied) planes are illustrated.
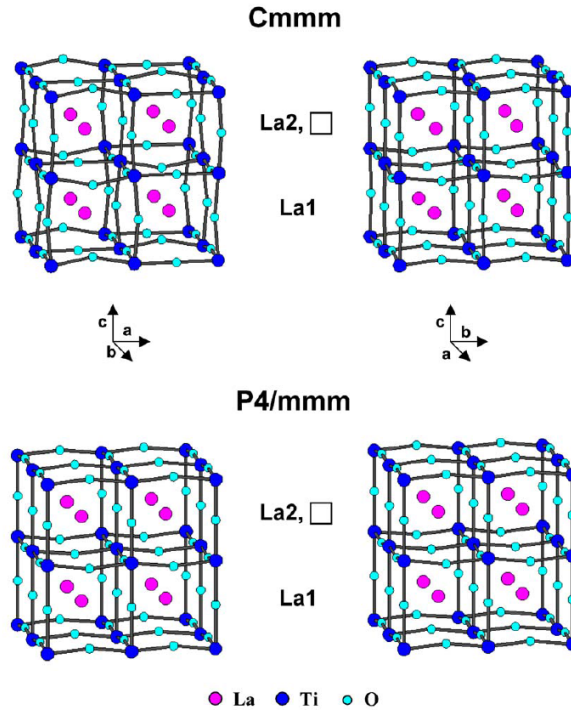
Fig. 14 Crystal structure of $Li_{0.18}La_{0.61}TiO_3$ perovskite along the [010] (left) and [100] directions (right) at 5 K (top) and 773K (bottom) as deduced from Cmmm and P4/mmm model. [53]

At higher temperatures, orthorhombic-tetragonal transformation begins, tetragonal phase (a, a_p, $2a_p$; where a_p stands for the cell parameter of the ideal cubic perovskite) begins to be seen, and its spatial group is P4/mmm [53].

1.1.2.6. $Li_{0.2}La_{0.6}TiO_3$ crystal structure

$Li_{0.2}La_{0.6}TiO_3$ has the tetragonal tungsten bronze type of structure. At 1000°C, the diagonal cell parameters are a ≈ $\sqrt{2}a_p$, b ≈ $\sqrt{2}a_p$, c ≈ $2a_p$. The schematic representation of $La_{0.6}Li_{0.2}TiO_3$ structure is shown in Fig. 15 [54].
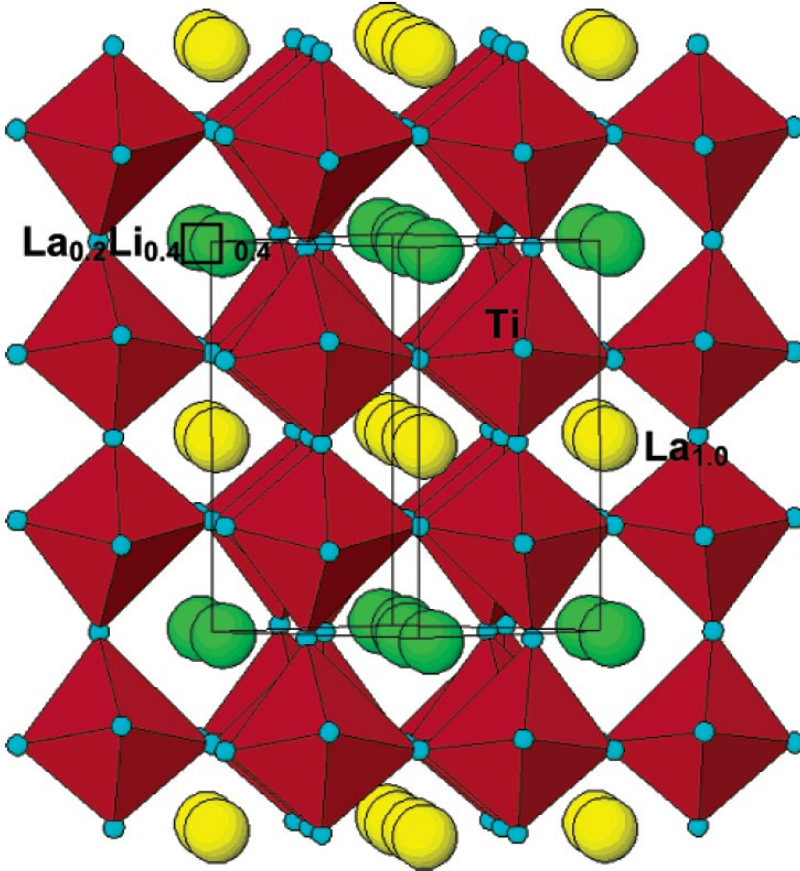
Fig. 15 Schematic representation of the structure of $Li_{0.20}La_{0.60}TiO_3$ quenched from 1000 °C [54]

The symmetry conforms to the Pmmm space group. All the crystals consist of domains of this cell, and in each domain, the long c-axis is oriented along

one of the three main crystallographic directions. Only at approximately 1200 °C transaction into a cubic perovskite cell is observed [54].

1.1.3. Crystalline varieties of $Bi_2O_3 – V_2O_5$ system

$Bi_2O_3 – V_2O_5$ mixed oxide has attracted a lot of attention over the years due to its qualities, such as high density, great electrical conductivity, ferroelastic properties, and thermal stability. These properties highly depend on the crystal form. This system has been identified by many phases, such as $BiVO_4$ [55], $Bi_{1.7}V_8O_{16}$ [56], $Bi_2O_3–V_2O_5$ [57], $Bi_6V_3O_{16}$ [58], $Bi_4V_2O_{11}$ [59], $Bi_{3.5}V_{1.2}O_{8.25}$ [60], $Bi_{23}V_2O_{44.5}$, $Bi_8V_2O_{17}$, and $Bi_{46}V_8O_{89}$ [56, 61].

1.1.3.1. $BiVO_4$ crystal structure

$BiVO_4$ has three main crystal forms: zircon structure with a tetragonal system, monoclinic scheelite structure, and tetragonal (s-t) system. The transaction between tetragonal zircon structure and monoclinic scheelite structures is irreversible, while tetragonal scheelite structure transformation from monoclinic scheelite structure can be reversed and occurs at 528 K [55].

Figure 16 shows the bismuth vanadate unit cell of a tetragonal crystal lattice with a 1:1 ratio of bismuth to vanadium.
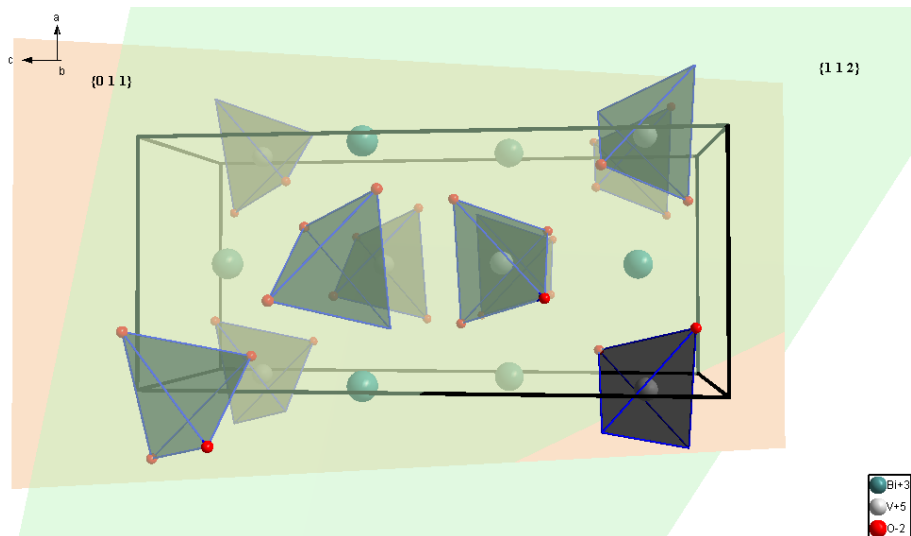
Fig. 16 Monoclinic crystal structure for bismuth vanadate composition [62]

When BiVO$_4$ tetragonal zircon structure is heat treated above 670-770 K or crushed into powder at room temperature [55], BiVO$_4$ has a monoclinic, distorted scheelite crystal structure with the spatial group designation of C2/2. The parameters of the lattice are determined by the general notation: a ≠ b ≠ c; α ≠ β ≠ γ ≠ 90°, where a, b, and c are the lattice parameters, and α, γ, and β are the angles between them. For BiVO$_4$, a = 5.1956 Å, b = 5.0935 Å, c = 11.7045 Å, and α = γ = 90°, and β = 90° [62, 63].

BiVO$_4$ tetragonal structure is similar to the BiVO$_4$ monoclinic, distorted scheelite crystal structure, and is defined by these parameters: a = 5.147 Å, b = 5.147 Å, c = 11.722 Å, o α = γ = 90°, and β = 90° [55].

1.1.3.2. Bi$_2$O$_3$–V$_2$O$_5$ crystal structure

Ternary oxide Bi$_2$O$_3$–V$_2$O$_5$ has a fluorite-type superstructure with a pseudo monoclinic cell (Fig. 17). The parameters are determined by the general notation: a ≠ b ≠ c; β ≠ γ; γ = α = 90 °, where a, b, and c are the lattice parameters, and α, γ, and β are the angles between them.
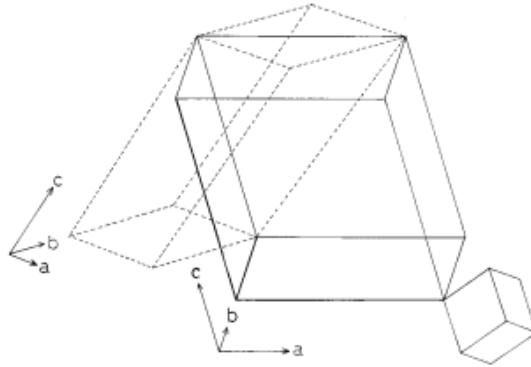
Fig. 17 The unit cell vectors of 6Bi$_2$O$_3$–V$_2$O$_5$ [57]

For Bi$_2$O$_3$–V$_2$O$_5$, a = 20.023 Å, b = 11.668 Å, c = 20.472 Å, and β = 107.13°. α = γ = 90 °. The unit cell vectors are presented in Fig. 17, where the solid lines show the monoclinic unit cells, while the dotted lines show the triclinic unit cells [57].

1.1.3.3. $Bi_4V_2O_{11}$ crystal structure

$Bi_4V_2O_{11}$ displays three polymorphs, depending on the temperature. The α-polymorph is stable from room temperature up to 430 °C, β between 430 and 570 °C, and γ, which is the most conductive polymorph, above 570 °C up to the melting point around 870 °C [59, 64-66]. The unit cell of a tetragonal bismuth vanadate with a 2:1 ratio of bismuth to vanadium and the spatial designation of I4/mmm is shown in Fig. 18.
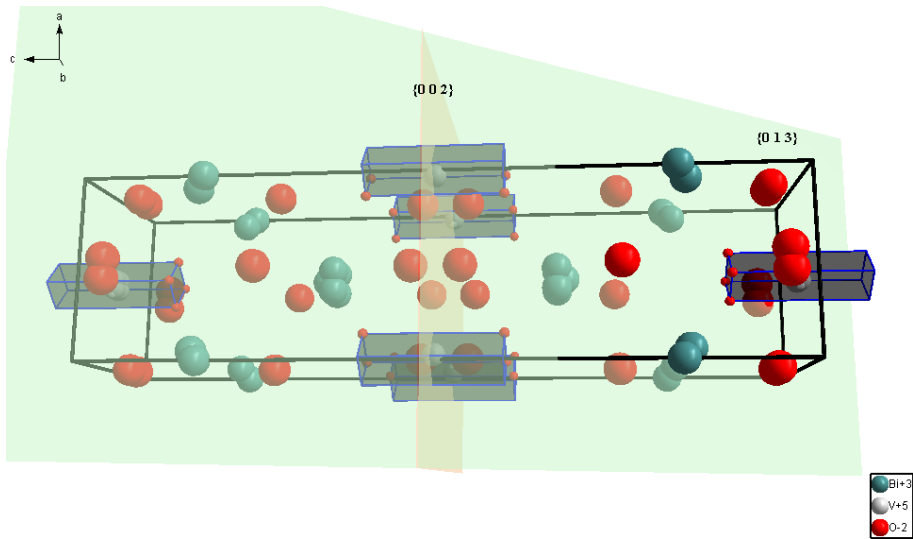
Fig. 18 Tetragonal crystal structure for $Bi_4V_2O_{11}$ [64]

The parameters of the γ tetragonal polymorph are determined by the general notation: $a = b \neq c$; $\alpha = \beta \neq \gamma \neq 90$, where a, b, and c are the lattice parameters, and α, γ, and β are the angles between them. For $Bi_4V_2O_{11}$, a = 3.9917 Å, b = 3.9917 Å, c = 15.4309 Å, and α = 90°, γ = 90°, and β = 90° [64].

1.1.3.4. $Bi_{3.5}V_{1.2}O_{8.25}$ crystal structure

The previously mentioned α- $Bi_4V_2O_{11}$ decomposes to a mixture of $BiVO_4$ and $Bi_{3.5}V_{1.2}O_{8.25}$. The parameters of the $Bi_{3.5}V_{1.2}O_{8.25}$ superstructure with triclinic symmetry are determined by the general notation: $a \neq b \neq c$; $\alpha = \beta \neq \gamma \neq 90$, where a, b, and c are the lattice parameters, and α, γ, and β are the angles between them. For $Bi_{3.5}V_{1.2}O_{8.25}$, a = 16.4521 Å, b = 16.8861 Å, c = 7.0914 Å, and α = 91.3°, γ = 96.0°, and β = 95.2° [60].

1.1.3.5. $Bi_6V_3O_{16}$ crystal structure

$Bi_6V_3O_{16}$ has the orthorhombic crystal structure and Pnma space group. The parameters of the lattice are determined by the general notation: $a \neq b \neq c$; $\alpha \neq \beta \neq \gamma \neq 90$, where a, b, and c are the lattice parameters. For $Bi_6V_3O_{16}$, a = 5.4721 Å, b = 17.2542 Å, c = 14.9174 Å [58, 67]. The crystal structure of $Bi_6V_3O_{16}$ is presented in Fig. 19.
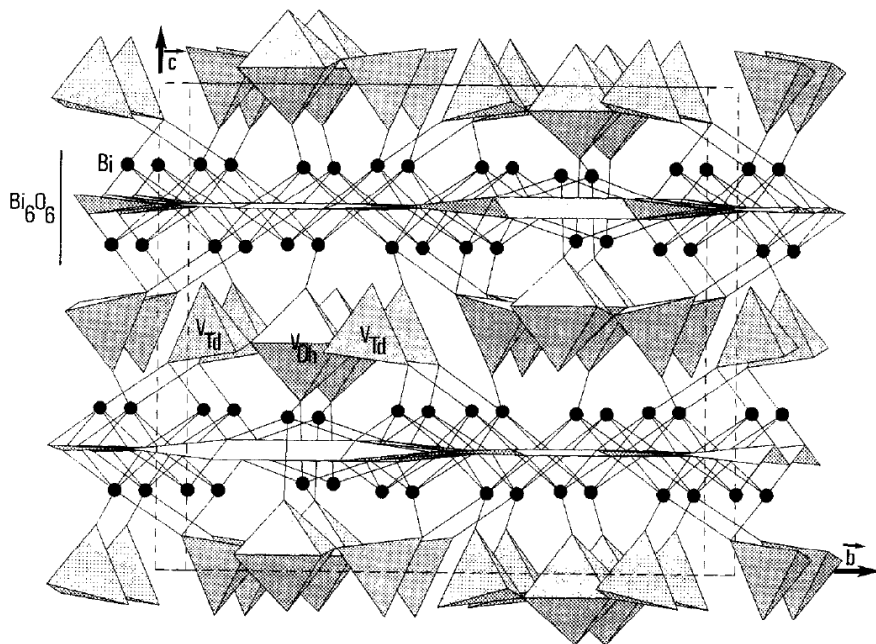
Fig. 19 $Bi_6V_3O_{16}$ orthorhombic crystal structure

These parameters can be compared to the previously mentioned α-$Bi_4V_2O_{11}$ in a low-temperature form. While α- $Bi_4V_2O_{11}$ cell results in a three-fold commensurate modulation along the α-axis of the orthorhombic cell, $Bi_6V_3O_{16}$ three-fold modulation appears along the β axis.

1.1.3.6. $Bi_{46}V_8O_{89}$ crystal structure

$Bi_{46}V_8O_{89}$, with a bismuth to vanadium ratio of 5.75:1, has a monoclinic crystalline lattice whose space group is – P21/c. In $Bi_{46}V_8O_{89}$, four positions (O29–O32) are partially filled by oxygen that can participate to the pathway of the oxygen ionic conductivity.

The parameters are determined by the general notation: $a \neq b \neq c$; $\alpha = \gamma \neq \beta$, where a, b, and c are the lattice parameters, and α, γ, and β are the angles between them. For $Bi_{46}V_8O_{89}$, $a = 20.0100$ Å, $b = 11.6445$ Å, $c = 20.4136$ Å, and $\alpha = 90°$, $\gamma = 90°$, and $\beta = 107.2700°$ [61].

The unit cell of the monoclinic crystalline lattice is shown in Fig. 20 [61].
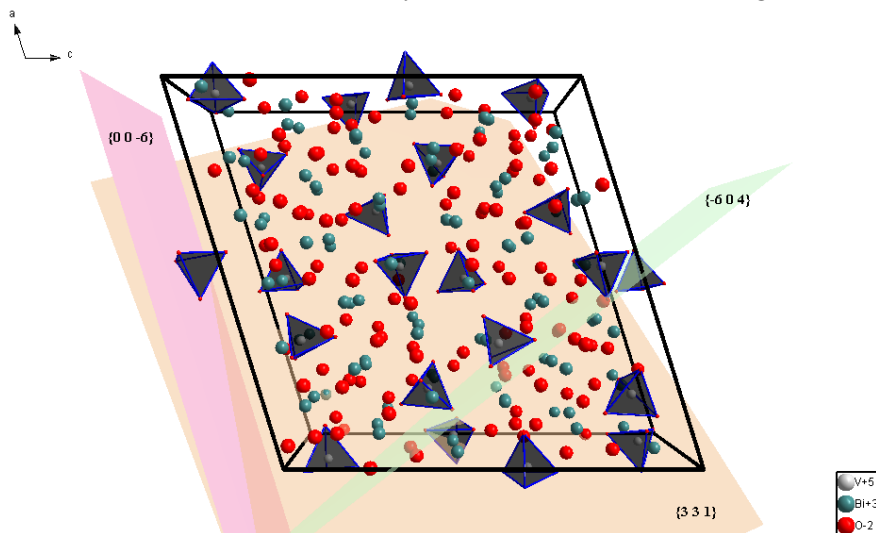
Fig. 20 Monoclinic crystal structure for $Bi_{46}V_8O_{89}$ [61]

It is also interesting to note that the proposed structures in this range of compositions correspond to superstructures based on a fluorite pseudo-fcc subcell.

1.2. Sol-gel and other types of syntheses of multicomponent oxides

Nowadays, sol-gel chemistry is associated with many different industries that are not only used in our everyday life but also have the potential to significantly improve it. Starting with more durable cell phone batteries [68], and ending with bone regeneration [69], this method has been widely studied due to its versatility, ability to control the structure and the composition of materials, low cost, and great scalability.

The first documented sol-gel synthesis goes back to 1845 when French chemist Jacques-Joseph Ébelmen prepared silica gels from $SiCl_4$ and alcohol [70]. He achieved hydrated silica synthesis by performing a slow hydrolysis of an ester of the silicic acid [71] and therefore, setting the grounds for what is now known as the sol-gel method. However, it wouldn't be until 1953 that this method would be incorporated into the industry and, a couple of years

later, into large-scale production. This discovery was claimed to be rather accidental than planned [72], so it was only 19 years later that the term "sol-gel" gel was actually introduced when British scientist Thomas Graham coined this term to describe his work with "silica soils" [73]. Graham improved Ebelmen's theory by showing that the water in the silica gel could be replaced with organic solvents [70]. Rear-view mirrors, anti-reflection coatings, and sun-shielding windows were the first products to be manufactured via sol-gel synthesis. Despite its initial success, it took another decade to establish that this method could be used to synthesize any type of multicomponent oxide by using the alkoxides of different elements via a sol-gel process [74]. Since then, various products have been produced this way and used daily, making our lives more convenient and comfortable, and in some cases, even saving our lives. Over the years, the sol-gel technique had been studied by many great minds, including Geffecken and Berger (dip-coating method) [75], Pajong (aerogels and xerogels) [76], Roy (homogeneous powders) [77], Teichner (hypercritical dried alcogels) [78], and many others. This work focuses mainly on the aqueous sol-gel synthesis technique of three types of remarkable materials for $MAlMo_2O_8$, $Li_{3x}La_{2/3−x}TiO_3$, and $Bi_2O_3–V_2O_5$ compositions. Other types of preparation techniques, published in literature, are also reviewed in this section.

1.2.1. Alkali metal aluminium molybdates

Preparing a homogeneous aquatic solution is the most challenging stage of this synthesis. This is due to the fact that while molybdenum oxide is soluble in basic solutions, aluminum ions hydrolyze in these conditions, forming a solid hydroxide. To overcome this, tartaric acid is used when such individual components need to be dissolved. Tartaric acid acts like a complex-creating agent that traps all ions in the solution, disallowing the formation of solid compounds, regardless of the pH change.

Due to its simplicity and low-costs, aqueous sol-gel method is an excellent choice to synthesize multicomponent materials, which is especially important nowadays considering not only the increased costs of the materials, but also the growing requirements to use environmentally friendly starting compounds. By performing the sol-gel synthesis, it is possible to obtain porous compounds whose network structure corresponds to the shape of the initial dried gels. Under critical drying conditions (e.g., pressure) the gels are released from the solutions without any fissures or cracks, which would often occur when using other methods. Such aerogels are characterized by a

particularly dense structure, which is also preserved in the final ceramic materials, increasing their strength and durability. With planned application of sol–gel technology, it is possible to successfully increase the range of manufactured products, simultaneously increasing the competitive and operational capabilities of this method in terms of scientific and practical application [86-91].

In this section, other types of different synthesis methods for various alkali metal molybdates are also reviewed. Table 1 shows the preparation techniques and their conditions suggested in the literature.

Table 1 Synhesis method for the preparation of $MAlMo_2O_8$ ceramic

Final compound	Synthesis method	Used materials	Heating conditions	Ref.
Cr^{3+}:$KAlMo_2O_8$	Top-seeded solution growth	K_2CO_3, Al_2O_3, MoO_3, Cr_2O_3	Incongruent melting (over 715 ºC)	[23]
$NaAlMo_2O_8$	Top-seeded solution growth	Na_2CO_3, Al_2O_3, MoO_3	Incongruent melting (over 715 ºC)	[25]
$KAlMo_2O_8$	Top-seeded solution growth	K_2CO_3, Al_2O_3, MoO_3	Incongruent melting (over 715 ºC)	[25]
$RbAlMo_2O_8$	Top-seeded solution growth	Rb_2CO_3, Al_2O_3, MoO_3	Incongruent melting (over 715 ºC)	[43]
$CsAlMo_2O_8$	Top-seeded solution growth	Cs_2CO_3), Al_2O_3, MoO_3	Incongruent melting (over 715 ºC)	[43]
$KAlMo_2O_8$	Top-seeded solution growth	K_2CO_3, Al_2O_3, MoO_3	Incongruent melting (over 715 ºC)	[79]
$CsAlMo_2O_8$	Top-seeded solution growth	$Cs_2Mo_3O_{10}$ and Al_2O_3 melt	Incongruent melting (over 715 ºC)	[30]
$NaAlMo_2O_8$	Top-seeded solution growth	Na_2CO_3, Al_2O_3, MoO_3	Incongruent melting (over 715 ºC)	[80]
$CsAlMo_2O_8$	Top-seeded solution growth	$Cs_2Mo_2O_7$ and Al_2O_3	Incongruent melting (over 715 ºC)	[29]
$KAlMo_2O_8$	Top-seeded solution growth	$K_2Mo_3O_{10}$ and Al_2O_3 ($Cr(NO_3)_3$)	Incongruent melting (over 715 ºC)	[81]
$NaAlMo_2O_8$	Pechini	Na_2MoO_4, $Al(NO_3)_3 \cdot 9H_2O$, $((NH_4)_6Mo_7O_{24} \cdot$	480–650 ºC	[82]

Final compound	Synthesis method	Used materials	Heating conditions	Ref.
		$4H_2O$, citric acid, ethylene glycol		
$KAlMo_2O_8$	Pechini	K_2MoO_4, $Al(NO_3)_3 \cdot 9H_2O$, $((NH_4)_6Mo_7O_{24} \cdot 4H_2O$, citric acid, ethylene glycol	480–650 °C	[82]
$RbAlMo_2O_8$	Pechini	Rb_2MoO_4, $Al(NO_3)_3 \cdot 9H_2O$, $((NH_4)_6Mo_7O_{24} \cdot 4H_2O$, citric acid, ethylene glycol	480–650 °C	[82]
$NaAlMo_2O_8$	Solid-state	Na_2CO_3, Al_2O_3, and MoO_3	500, 600, 700 °C	[83]
$NaAlMo_2O_8$	Sol-gel	Na_2CO_3, Al_2O_3, MoO_3	500, 600, 700 °C	[83]
$NaAlMo_2O_8$	Precipitation	Na_2CO_3, Al_2O_3, MoO_3	500, 600, 700 °C	[83]
$NaAlMo_2O_8Cr^{3+}$	Precipitation	$Al(NO_3)_3 \cdot 9H_2O$, $Cr(NO_3)_3 \cdot 9H_2O$, $Na_2MoO_4 \cdot 2H_2O$	600–720 °C	[84]
$NaAlMo_2O_8$	Top-seeded solution growth	Na_2CO_3, Al_2O_3, MoO_3	Incongruent melting (over 715 °C)	[21]
$KAlMo_2O_8$	Top-seeded solution growth	K_2CO_3, Al_2O_3, MoO_3	Incongruent melting (over 715 °C)	[21]

The most widely investigated synthesis method in the literature is the top-seeded solution growth (TSSG) technique in which monocrystals and polycrystals are obtained. The simplified version of this synthesis is shown in Fig. 21 [85].
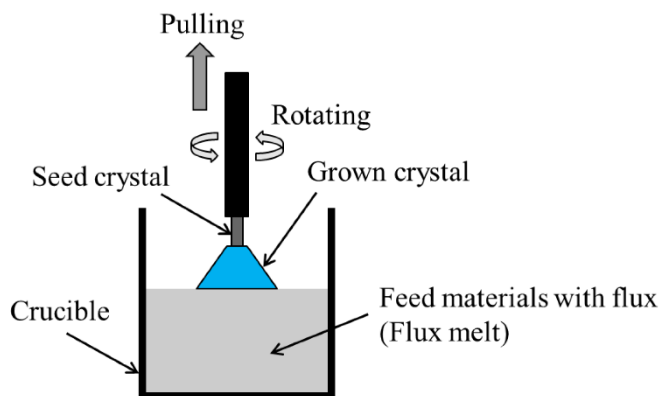
Fig. 21 TSSG schematic representation [85]

The crystallization process is performed by adding fine crystals of the final crystallizable compound to a supersaturated solution of the individual salts. This method resembles the well-known Czochralski and Nacken Kyropoulos single crystal growth techniques. Using the TSSG method, crystals can be obtained in two ways: either by using the vertical temperature gradient to transport the components of the initial compounds, or by slow cooling of the supersaturated solution. In the first option, $M^xLaMo_2O_8$ (where x is an alkali metal) compounds alloyed with impurity elements are obtained, while the slow cooling produces pure crystalline phases [21, 23, 25, 29, 30, 43, 79, 80].

However, the oldest method recorded is the solid-state synthesis, where separate precursors are mechanically mixed and – by adjusting their heating temperature – a chemical reaction between them is carried out. In other words, the diffusion of individual ions is carried out in the reaction medium due to temperature [83].

Another widely used method is precipitation synthesis. It is often favored due to its simple conditions and inexpensive equipment. With this method, it is possible to precipitate much smaller particles compared to the solid-state method. In the precipitation technique, an appropriate solvent is chosen to dissolve the individual components of the final compounds – usually fitting metallic salts – then the reaction mixture is stirred and can be heated if required. After a couple of hours, the precipitate is filtered and washed with ethanol, acetone, or water, which allows the discarding of the unreacted products [83, 84].

Pechini method is another technique that has been commonly researched, in which the metal cations are complexed by using citric acid and ethylene glycol, polymerizing the initial salts to form a dispersed system called a gel.

This way it is possible to perform the synthesis at relatively low temperatures. During the pyrolysis of the obtained gels, the formed ions do not accumulate in one place, but instead react with each other, avoiding unfavorable sublimation of molybdenum (VI) oxide [82].

1.2.2. LLTO ceramic

The preparation process of LLTO is inexpensive [92], as well as considerably environmentally friendly, which is exactly why lithium lanthanum titanates have received a lot of attention over these few years when it came to research and improvement of energy-storing devices [3, 68].

However, synthesizing LLTO ceramics while using different methods can have significant effects on the final LLTO product structure and electrochemical properties. For this reason, a deeper examination of reported LLTO synthesis methods was performed, investigating methods, such as sol-gel synthesis, solid-state reactions, ball-milling methods, hydrothermal methods, tape-casting syntheses, and molten salt methods.

Sol-gel technique to prepare lithium lanthanum titanates was examined by Carazeanu et al.. $LiNO_3$, $La(NO_3)_3 \cdot 6H_2O$, and titanium butoxide $Ti(OC_4H_9)_4$ with ethaline glycol were used as primary materials, citric acid was used as a ligan; then the samples were heated. The synthesized $La_{0.66}Li_{0.33}TiO_3$ was then examined by performing XRD, Thermogravimetry and Differential Thermal Analysis (DTA-TG), SEM, and High-resolution transmission electron microscopy (HRTEM). From the Differential thermal analysis (DTA) curve, an endothermic peak could be observed at approximately 99°C degrees, which was suggested to be due to the water adsorption in the pores. The exothermic peaks at the temperature range of approximately 300 to 600°C degrees exhibited the combustion of the acid metal-citric complex. The citric acid, in addition to ethylene glycol, accelerated the synthesis of the LLTO oxide. The XRD results showed patterns of amorphous solids at the temperatures of 750°C and lower, which suggests that full crystallization did not occur. At 800°C degrees both amorphous, and LLTO crystal phases were observed, while at 900°C degrees only single phase $La_{0.66}Li_{0.33}TiO_3$ was detected, with a complete crystallization after being heat treated at 1000°C degrees for 2 hours [97].

Another article discussed obtaining the LLTO ceramics in two different ways in one study, using both sol–gel synthesis, and solid-state reaction. In sol–gel synthesis, tetra-propyl orthotitanate $(Ti(OC_3H_7)_4)$, lithium nitrate $(LiNO_3)$, and lanthanum nitrate $(La(NO_3)_{3.6}H_2O)$ were used as starting

materials. Some impurities could still be observed, mostly $La_2Ti_2O_7$, which could modify the surface of the grain boundary, and was most likely the reason of poor pH sensing property that was not observed in solid state synthesis [95].

The authors managed to modify the synthesis conditions and replicate the experiment in their new study. The new improved synthesis focused on avoiding the use of alkoxides – which are highly unstable in air atmosphere – and choosing a Pechini-type polymerizable precursors instead. X-ray diffraction study showed a pure crystalline phase of LLTO. The sol–gel method was strongly favored in this study to due significantly reduced time and temperature needed to synthesize the LLTO ceramics [96].

Other types of syntheses techniques have been investigated as well to prepare Li-La-Ti-O gel precursors.

In 2021, Huang et al. chose a rather unusual method and synthesized $Li_{0.33}La_{0.55}TiO_3$ (LLTO) by performing the molten salt method and investigating the synthesis effect on its properties and structure. The optimized conditions of the experiment were calcinating at 1100 ∘C and sintering at 1300 ∘C under LiCl–KCl. In the experiment, it was also proven that higher reaction temperatures have a significant effect on the morphology of LLTO powder, changing the structure from a multi-rod-like and sheet-like structure into a multi-sheet-like structure [93].

The same approach as discussed above was modified and used to prepare LaOCl microplates in the tape-casting study. Such a method is widely used for producing ceramic electrolyte films on a wider production scale due to its one-step tape casting method, performed at significantly low temperatures. In 2020, Huang et al. examined LLTO preparation via the tape-casting method [94].

La_2O_3, KCl, and LiCl were chosen as starting materials to prepare the microplate. The microplate, along with Li_2CO_3 and TiO_2 were then mixed and grounded. After adding the solvent and dispersant, the mixture was ground, and finally, the defoaming agent was added. Sheet forming was performed using a scalpel, and the formed films were stacked and heat-pressed, until being sintered at 900 to 1350 °C for 6 hours. The experiment showed that $Li_{0.33}La_{0.55}TiO_3$ could be successfully synthesized at low temperatures, such as 900 °C, with a total ionic conductivity of 4.3×10^{-6} S cm^{-1} increasing with the increase in temperature. Ionic conductivity of 6.13×10^{-5} S cm^{-1} was obtained at 1350 °C with a low activation energy of 0.28 eV [94], proving LLTO materials highly favorable in secondary energy storage applications.

In other works, spin-coating techniques were used to prepare chemically stable, thin, and smooth LLTO films, which is a crucial property when it comes to lithium battery application. Abhilash et al. prepared the LLTO thin film nano-electrolytes by spin coating and using sol–gel precursor solution. The $Li_{0.5}La_{0.5}TiO_3$ sol–gel solution has been synthesized by using lithium nitrate ($LiNO_3$), lanthanum nitrate hexahydrate ($La(NO_3)_{3.6}H_2O$), tetra butyl titanate ($C_{16}H_{36}O_4Ti$) and acetyl acetone ($C_5H_8O_2$). The synthesized ceramics were investigated by performing structural analysis, Fourier transform infrared (FTIR) spectroscopy, morphological analysis, and doing conductivity studies.

The interesting aspect of this study was that the LLTO films could not be calcinated at a higher temperature than 550 °C because of the thermal instability of the glass substrates above 600 °C. Therefore, in order to achieve the crystalline phase, the LLTO films were heated in oxidative environment for a longer time (5h, 20h, 40h). The films showed a complete crystalline phase after heating at 550 °C for 40 h. FT-IR spectrum of the LLTO films also showed great results after heating at 550 °C for 40 h. After heating the samples at 550 °C for 5 and 20 hours, some impurities were recorded, however, at 40 hours of heating the peak that was related due to the acetone related impurities decreased its broadening, which again indicates the removal of precursor impurities during calcination. Morphological analysis also confirmed the previous results. After having calcined the sample at 550 °C degrees for 5 hours, the Scanning Electron Microscopy (SEM) analysis showed dense, cracked structures and mesoporous structures. After being heated for 20 hours, the sample showed a transformation to more structured particles, and the pores that were observed in the previous sample became narrower. LLTO films that were calcined at 550 °C for 40 hours, showed a complete crystalline structure [97].

An alternative LLTO synthesis method had been examined by Bhat et al. In their study, two types of LLTO syntheses were performed – a conventional method and the microwave method. The first samples were prepared by mixing La_2O_3, TiO_2 and Li_2CO_3 while continuously heating the materials for 4 hours at 800 °C, and then increasing the temperature to 1150 °C and heating for another 36 hours, while grinding the materials every 12 hours. The microwave synthesis samples were prepared in two ways. In the first one, the same mixture was used as in the conventional way with the addition of amorphous carbon. Then the entire mixture was pelletized and placed into an industrial microwave, turning it on at the highest settings.

In the second way, the initial mixture was pelletized, then embedded in amorphous carbon powder, and same procedure with the microwave was performed. While in both of those ways pure crystalline phase was achieved, the first way required an addition heating at 700 °C for 3 hours to remove the excess carbon in the composition. The samples were then analyzed. X-ray diffraction (XRD) patterns of both the conventionally prepared LLTO, and by the microwave synthesis corresponded to the values reported in the literature and between themselves. The conductivity of both conventionally prepared LLTO, and by the microwave synthesis was approximately similar, being 8.63 x 10^{-4} and 8.95 x 10^{-4} S cm^{-1}, respectively, which is also relatively similar to documented values in the literature [92]. In addition to being clean and simple to follow, this microwave method is also very rapid as the synthesis takes minutes to perform.

Romero et al. performed a study where LLTO ceramics were prepared lanthanum oxide (La_2O_3) and lithium carbonate (Li_2CO_3) as starting materials, which were dissolved in acetic acid and deionized water, while stirring at approximately 70 °C until homogenous solution formed [98].

Out of these methods described to synthesize LLTO products, many of them require high temperatures, various calcination steps or expensive materials, and long annealing time, therefore, sol–gel methods are highly recommended. While generally sol–gel synthesis provides final materials with smaller particle size, resulting in more dense structures, it can also produce more impurities, as well as lower ionic conductivity. In order to improve these qualities, more detailed experiments on sol–gel synthesis are needed.

1.2.3. $Bi_2O_3 – V_2O_5$ system

Different synthesis techniques of $Bi_2O_3 – V_2O_5$ systems have a great impact on the resulting materials, and therefore, their desired properties and potential application. The choice of synthesis can affect the crystal structure, particle shape and size, surface features, and the purity of the final compound. For example, sol-gel synthesis and precipitation methods allow adjusting the precursor concentration, giving control over the composition of the material. Sol-gel method also allows to control the particle size and shape, while methods, such as the Ultrasonic spray pyrolysis (USP), mostly produce fine particle size. In addition, USP method results in materials with a better photocatalytic activity in comparison to the same material obtained by solid-state reactions. The structure of the final compound, obtained by the one-step hydrothermal method highly depended on the pH conditions, while the solid-

state method depended on the high-temperature calcination. The appropriate synthesis technique should be chosen based on the pertinent characteristics of the final compound.

Pookmanee et al. used the sol-gel method to prepare $BiVO_4$ powder. The product was synthesized by using $Bi(NO_3)_3H_2O$ and ammonium vanadate (NH_4VO_3) as starting materials. Two solutions were prepared: solution A - 0.03 M $Bi(NO_3)_3 \cdot 5H_2O$ dissolved in 4 M HNO_3 and solution B – 0.03 M NH_4VO_3 dissolved in 4 M NH_4OH. Each solution was stirred for 30 minutes. Solution A was then added drop-wise into the solution B, continuously stirring on a magnetic plate until both solutions were mixed with a 1:1 molar ratio, and yellow solution was obtained. C_2H_5OH was then added to the solution and heated at 70 ºC while stirring for 1 hour, resulting in a yellow sol solution. The addition of 1 mol CH_3COOH caused the sol turn into a yellow gel, which was then dried in the oven at 100 ºC for 24 hours and calcined in a furnace. A pure monoclinic single-phase structure was obtained, with no peaks of any other impurities present. The increase of the calcining temperature exhibited the growth of the crystal size [103].

Mairesse et al. performed a solid-state $Bi_4V_2O_{11}$ synthesis. Bi_2O_3 and V_2O_5 were meticulously ground in an agate mortar and heated in Au foil boats for 12 hours at temperatures of 600 ºC, 700 ºC, and 800 ºC. Then the compound was cooled from the last firing temperature to 300 ºC at the rate of 5 ºC per hour, and then further cooled to room temperature at the rate of 10 ºC per hour. Such gradual cooling of the material was performed in the air and its slow cooling speed was especially important to the synthesis, as the oxygen stoichiometry in this material is highly influenced by the reaction conditions. This way, it was possible to ensure the compound was fully oxidized. The synthesis resulted in a monoclinic α- $Bi_4V_2O_{11}$ and a small amount of $BiVO_4$ impurity [66].

The importance of slow cooling was supported in another study as well, where Bi_2O_3 and V_2O_5 had been dried at 300 ºC and mixed into a paste with acetone in an agate mortar, dried, and then heated in Au foil boats. The material was heated at 500 ºC for three hours, then the temperature was raised to 650 ºC and left overnight, then reground. After regrinding, the temperature was then raised back to 650 ºC for one hour and then raised to 800 – 820 ºC overnight, then reground and heated overnight at the same temperature. The study determined that single-phase $Bi_4V_2O_{11}$ was only obtained by rapid cooling, and just as in the previous study, resulted in α-$Bi_4V_2O_{11}$ and some $BiVO_4$ impurities [99].

In another study, Watanabe et al. prepared $Bi_{3.5}V_{1.2}O_{8.2}$ by using 99.9% pure Bi_2O_3 and V_2O_5. Proportions of $Bi_{1-x}V_xO_{1.5/x}$ (where x equals 0.2 – 0.35) were hand-mixed in an agate mortar and transferred into a covered platinum crucible and heated for 20 hours at 800-850 ℃, then cooled down to room temperature by an air stream. Intermediate grindings were performed, and the material was heated at the same temperature after every grinding. Then it was placed into a gold crucible, heated at 550 ℃ for over 300 hours, and cooled down by an air stream again. The process was repeated several times. The chemical analysis showed the composition of two representative samples as follows: 74.56±0.03 mol% Bi_2O_3 and 25.44±0.01 mol% V_2O_5 for $Bi_{3.5}V_{1.2}O_{8.25}$ and 66.69±0.01 mol% Bi_2O_3 and 33.31±0.02 mol% V_2O_5 for $Bi_4V_2O_{11}$. Pure α-form was observed at the more bismuth-rich composition, 31.50 mol% V_2O_5 [60].

Beg et al. study prepared the Bi_2O_3–V_2O_5 by using Bi_2O_3 and V_2O_5 as starting materials with various molar compositions (0.9:0.1, 0.8:02, 0.7:0.3, 0.6: 0.4, 0.5:0.5, 0.4:0.6) and mixed in an agate mortar, then sintered in the air in a Muffle Furnace for 25 hours at the temperature of 700 ℃. Using hydraulic press and applying the pressure of 5 tons, pellets have been prepared. Then the electrical conductivity of Bi_2O_3–V_2O_5 and Bi_2O_3 were examined at different temperatures. The results suggest that an increase in temperature and V_2O_5 concentration increases the electrical conductivity. At 230-260 ℃ a sudden rise in conductivity was observed at all compositions, which is explained to occur due to the phase transition of $BiVO_4$ from a monoclinic scheelite type to that of tetragonal scheelite type structure. This hypothesis is supported by the Differential Scanning Calorimetry (DSC) and XRD results [36].

Similar Bi_2O_3–V_2O_5 has been described in the study performed by Exner et al., where the starting materials were Bi_2O_3 and V_2O_5 and a two-stage grinding process was done. Both starting materials have been ground separately for 4 hours in a planetary ball mill using cyclohexane as a milling fluid, dried and then stoichiometric amounts of the metal oxides were added to the planetary ball mill for an additional hour. Authors pointed out that the duration of milling was chosen in order to achieve a homogeneous mixture while avoiding a mechanochemical synthesis. Then aerosol deposition method was used to apply the ceramic film [100].

One-step hydrothermal method was used in the study performed by Li et al.. 2 mmol bismuth nitrate pentahydrate ($Bi(NO_3)_3 \cdot 5H_2O$) was dissolved in a 100 mL beaker using 60 mL ultrapure water and 2 mL nitric acid (HNO_3). The solution was stirred at room temperature on a magnetic shaker for 30 minutes

until the material dissolved completely. 1 mmol of ammonium metavanadate (NH_4VO_3) was gradually added to the solution. In order to adjust the pH to 10, 11, and 12, nitric acid or ammonium hydroxide was added and the mixture was stirred for another 30 minutes. Then the suspension was transferred to a 100 mL Teflon-lined stainless autoclave and incubated at 180 °C in the oven for 12 hours. The autoclave gradually cooled down to room temperature, and the compounds were dried in the oven for 3 hours at 60 °C. The study showed that the formation of the $BiVO_4/Bi_4V_2O_{11}$ was highly dependent on the pH conditions during the synthesis. When the solution was adjusted to pH 11, monoclinic $BiVO_4$ and orthorhombic $Bi_4V_2O_{11}$ were obtained [101].

Kumar et al. synthesized $Bi_4V_2O_{11}$ by mixing bismuth nitrate pentahydrate $(Bi(NO_3)_3 \cdot 5H_2O$ and vanadium oxide (V_2O_5) in an agate mortar for 6 hours, using the minimum amount of required ethanol until a homogenous mixture was obtained. Then the mixture was held in a vacuum oven at 100 °C overnight in order to remove the excess water. The obtained yellow powder was mixed with glycine (NH_2CH_2COOH) and moved into a glass bowl, which was then ignited at 300 °C. The formed paste then underwent the process of melting and dehydration, resulting in the release of significant quantities of gases, such as carbon and nitrogen oxides. The mixture then foamed and expanded, forming a shape that eventually ruptured with a flame and emitted a glowing light, resulting in a brown-yellow foam. In order to enhance the crystalline structure and eliminate organic impurities, the obtained material was then annealed at 400 °C for 2 hours in an air environment. The analysis results indicated that the $Bi_4V_2O_{11}$ sample was monoclinic and consisted of layered Aurivillius-type particles [102].

In 2001, Tokunaga et al. published $BiVO_4$ synthesis by precipitation method. $BiVO_4$ was synthesized by dissolving $Bi(NO_3)_3 \cdot 5H2O$ and $Na_3VO_4 \cdot 7H_2O$ in concentrated in nitric acid. Nitric acid solutions of 0.12 mol/L $Bi(NO_3)_3$ and 0.12 mol/L Na_3VO_4 were prepared by adding water to the solutions, and then the solutions were mixed. Different amounts Na_2CO_3 (3 g, 5 g, 6 g, 7 g, 8 g, 10 g) or $NaHCO_3$ (3 g, 5 g, 7 g, 8 g) were added, and the solution was stirred for 4.5 - 4.6 hours. $BiVO_4$ precipitation was washed with water and filtered, then dried at approximately 47 °C degrees for 12 hours. The obtained $BiVO_4$ had a monoclinic scheelite structure. To further examine the formation process, X-ray diffraction patterns of $BiVO_4$, obtained at 4.5 - 46 hours of preparation time, were measured. The analysis showed that pure pattern of $BiVO_4$ (scheelite structure with tetragonal systems) was obtained after 4.5 hours, while $BiVO_4$ scheelite structure with monoclinic systems pattern was observed along with the $BiVO_4$ scheelite structure with tetragonal

systems pattern after 9 and 24 hours. The $BiVO_4$ scheelite structure with monoclinic systems pattern was only observed after 46 hours. Interestingly, the crystal form of $BiVO_4$, obtained by using 7 g of Na_2CO_3, showed the highest and significantly higher photocatalytic activity [55].

Dunkle et al. published the $BiVO_4$ synthesis using the USP method. $BiVO_4$ was synthesized by dissolving $Bi(NO_3)_3 \cdot 5H2O$ and ammonium vanadate (NH_4VO_3) with the molar ratio of 1:1 in ~3 M solution of nitric acid. Precursors were added in order to obtain the final concentration of 0.2 M, and the solution was stirred to obtain a homogenous mixture. A piezoceramic transducer operating at 1.65 MHz was used to convert a precursor solution into a micrometer-sized mist. The mist was then carried by an air flow (~1 standard liter/min) into a furnace at a temperature of 700 °C. The products were collected in water-filled bubblers at the furnace outlet. The water-filled bubblers were centrifuged to isolate the USP products, the pellets were washed with purified water a minimum of three times, and then were rewashed with absolute ethanol. The obtained powder was then dried under a vacuum for approximately 12 hours at room temperature. The $BiVO_4$ sample analysis showed a rather unique particle morphology – hollow shells or fractions of hollow shells were observed, as well as considerably higher surface area than compared to $BiVO_4$ prepared by solid state methods. USP method also resulted in better photocatalytic activity of $BiVO_4$ in comparison to $BiVO_4$ obtained by solid-state reactions [104, 105].

1.3. Properties and application of multicomponent oxide materials

As discussed in the previous chapter, the choice of the synthesis has a significant effect on the final compound's properties. After understanding how the synthesis technique affects the structure, composition, morphology and characteristics, researchers can use this information and apply these ceramics to many distinct industries. High ionic activity and substantial chemical, temperature, and pressure stability allow these multicomponent oxide materials to be used in the production of energy storing devices and gas or pressure sensors in harsh environments. Their non-toxicity allows their use in food industry and environmentally-friendly energy production. The antiviral and antimicrobial activities make bismuth vanadates very efficient in pharmaceutical waste degradation and biomedical devices production. Because of the narrow bandgap, bismuth vanadium oxides and alkali metal aluminium molydates exhibit great ferroelastic properties, and could be applied in tunable lasers and optical devices.

1.3.1. Application of alkali metal aluminium molybdate

Alkali metal aluminium molybdates $M^IAlMo_2O_8$ double molybdates (M = Li, Na, K, Rb and Ce) have received most of the attention due to their ferroelastic phase transitions and optical properties [106]. Alkali metal aluminium molydates exhibit high and continuous transparency in the wide range of the near-IR region [80], and therefore, are considered great laser host materials. Doped with transition metals or rare-earth ions, they can be used as a potential tunable laser material.

$NaAlMo_2O_8$, doped with Cr^{3+} ions, exhibits emission specific to the Cr^{3+} ions in octahedral oxygen coordination. One study suggests that by doping monoclinic $NaAlMo_2O_8$ with Cr^{3+} ions, three one-electron bands are incorporated into the band gap of the $NaAlMo_2O_8$ [107]. Interestingly, the concentration of Cr^{3+}, temperature, and excitation energy does not affect the positions of the R-lines, however, the temperature does have a significant affect on the $NaAlMo_2O_8$:Cr spectra under excitation by laser radiation. Similarly, $KAlMo_2O_8$, $RbAlMo_2O_8$, and $CsAlMo_2O_8$ have also been explored as hosts to Cr^{3+} ions [23, 30, 108].

At room temperature, $NaAlMo_2O_8$ and $KAlMo_2O_8$ crystals exhibit a spin-allowed broad band emission $^4T_2$-$^4A_2$, but when the temperature is lowered, a strong spin forbidden emission is observed. $RbAlMo_2O_8$, and $CsAlMo_2O_8$ absorption spectra exhibit $^4A_2$-$^4T_2$ and $^4A_2$-$^4T_1$ electron transition. The excitation spectra show $^4A_2$-$^4T_1$ emission. Based on the energy levels scheme, aluminium double molybdates lowest energy state was ^2E, so emission from this level was observed and showed a highly efficient relaxation between ^2E and $^4T_2$ levels in all alkali metal aluminium molybdate systems, doped with Cr^{3+} ions [30]. Based on this data, $RbAlMo_2O_8$, and $CsAlMo_2O_8$ are also considered to be good candidates for tunable laser material.

1.3.2. Application of LLTO ceramic

Lithium lanthanum titanate ($Li_{3x}La_{2/3-x}TiO_3$; LLTO) of a perovskite structure with cation deficiency at the A-sites is considered to be a very powerful conductor with a high bulk ionic conductivity ($\sim 10^{-3}$ S cm^{-1}) at room temperature [109], low activation energy, great stability in air [110], substantial hydrophobic and electrochemical properties [14].

Due to their high ionic conductivity [32], lithium lanthanum titanates are debated to be a good substitution for solid-state batteries, which are considered to be safer than currently used standard lithium-ion batteries. This is especially

important, granted the current technology has been associated with many fire incidents or even explosions, and it is still widely used in everyday life, in mobile phones, portable computers, or even electric and hybrid cars [111, 112]. LLTO materials could be a significantly safer alternative. Solid-state LLTO electrolytes would also be a more ecologically friendly and safer choice in comparison to solid polymer electrolytes because, unlike the latter ones, LLTO electrolytes do not include inflammable solvents [113]. In addition, LLTO compounds have been proven to have higher ionic conductivity compared to solid polymer electrolytes [114].

The most recent studies target $Li_{0.3}La_{0.57}TiO_3$ application for lithium-air batteries [115]. Lithium-air batteries have a much higher energy density and power density than lithium-ion batteries. That is because in lithium-air batteries, the oxygen is supplied continuously from the air and is used as the active material of the cathode, giving an energy density of 10 equal to that of a lithium-ion battery. For the same reason, they are also considerably lighter in weight, which is usually a more desirable quality in everyday electronics, such as mobile phones or laptops [116]. Interestingly, even better results were obtained after reducing the $Li_{0.3}La_{0.57}TiO_3$ pellet thickness by approximately 75% of its original size – the ionic conductivity increased by around 21%, from $1.31 \cdot 10^{-5}$ to $1.58 \cdot 10^{-5}$. The reason that a thinner pellet receives a higher conductivity is owing to a reduced number of grain boundaries through the lithium ions transport [115], and that is the key point that the authors plan to take into account when developing a further study.

A similar study has even been sponsored by the U.S. military, where $Li_{0.3}La_{0.57}TiO_3$ had been prepared using two different methods – solid state (LLTO-SS) and sol-gel (LLTO-SG), to better understand the mechanical properties of $Li_{0.33}La_{0.57}TiO_3$ and to predict its behavior, in hopes that it would be used in aqueous Li-air batteries or other battery applications requiring a long operating life. Significant differences had been observed in the morphology between the LLTO-SG and LLTO-SS materials. $Li_{0.3}La_{0.57}TiO_3$, prepared by the solid-state method, had significantly smaller and shorter pores than the same material that had been prepared by the sol-gel method. The grain size of the LLTO-SS was also smaller than that of the LLTO-SG. Interestingly, while one could expect the LLTO-SS to show higher fracture toughness due to its lower porosity, the complete opposite had been observed. The authors conclude that this is because the higher porosity in the LLTO-SG, especially the long pores along the grain boundaries, alters the fracture path enough to cause a part of the crack to propagate along the grain boundaries and lead to crack deflection and higher fracture toughness [117]. And that is

something else that needs to be addressed in order to successfully use LLTO ceramics in lithium-air batteries.

LLTO materials have also been discussed to be used at high temperature and high-pressure environments, such as ocean depths or even in nuclear equipment as an all-solid-state reference electrode due to their chemical stability and great electrical properties [10]. A reference electrode plays a vital role in the three-electrode configuration used for cyclic voltammetry; therefore, the chosen reference electrode must be chemically stable, and its electrical potential mustn't be influenced by any activity of the analyte. LLTO ceramics with a very high grain boundary conductivity of $8.8 \cdot 10^{-4}$ S cm^{-1} had been prepared and used to manufacture an all-soli-state reference electrode. It was then tested in cyclic voltammetric experiments and showed promising results, similar to commercially used liquid reference electrodes [10].

LLTO compounds have been investigated as potential pH indicators that could be used as a cheaper alternative in the food industry, for example, controlling milk fermentation and yogurt manufacturing. In their work, Bohnke et al. created two separate ion-selective sensors to demonstrate that LLTO-based indicators can detect different ranges of pH in different solutions (the first sensor with a liquid internal reference) and that it can be used to control the pH levels during the milk fermentation as well as in different food media (the second sensor with a solid internal reference). The second ion-selective sensor showed similarities to the currently used in the industry, more expensive glass membrane electrodes [118]. While more experiments are needed to better understand the technological limitations caused by material porosity and grain boundaries, it suggests that in the near future, LLTO compounds could be used as a cheaper and more stable alternative for pH indication in the food industry [6].

Another study suggests using LLTO-based pH indicators in the oil drilling industry to detect hydrogen sulfide gas. Since the gas is flammable, harmful to health, and under a few minutes of exposure at higher concentrations could even lead to death [15], it is important to find a convenient quality way of detecting the gas in time, which is what was proposed to be done by detecting and measuring sulfide ions in the drilling mud, using LLTO based pH sensors. The study proved that the sensors, based on LLTO compounds, show great ionic conductivity and good stability, and could be used in very harsh pH conditions from 1 to 14, which is perfect for oil drilling [7].

1.3.3. Application of bismuth vanadates

Bismuth oxide systems have been widely discussed as a potential electrolyte material due to their high-level oxygen ion conductivity. In their work, S. Beg et al., measured the electrical conductivity of both pure Bi_2O_3, and the $Bi_2O_3–V_2O_5$ samples at various temperatures up to 600 ^{o}C. It was observed that using a higher temperature and increasing V_2O_5 concentration, higher ion conductivity is recorded. An increase of conductivity was also observed at 230-260 ^{o}C and was theorized to be due to the phase transaction from a monoclinic scheelite type to tetragonal [36].

$Bi_2O_3 – V_2O_5$ application in pressure sensors has been discussed and investigated for over thirty years. While other types – silicon and foil strain – gauges have their own advantages [119, 120], such as low cost and short response time, thin film strain gauges, coated with $Bi_2O_3 – V_2O_5$, are preferred when a high level of accuracy is needed. $Bi_2O_3 – V_2O_5$ can directly bond with the supporting material through thermal evaporation without the organic epoxy layer, which could change in its size at different temperatures. Using $Bi_2O_3 – V_2O_5$ thin-film sensors eliminates this issue [121].

Solar water splitting is another interesting field where the potential of bismuth vanadate is explored. As increasing energy use is becoming a significant issue all over the world, finding a way to produce cheap, environmentally friendly, and renewable energy is now more important than ever. While solar energy has been widely advertised and used, it has some disadvantages that still need to be addressed: solar energy conversion, storage, distribution, the seasonal variability [122]. Quite often, not all these issues can be addressed to ensure stable, low-cost, and truly environmentally friendly energy production. Splitting water into usable hydrogen could solve these problems, as the only waste that would need to be utilized after the energy conversion would be water [123]. $BiVO_4$ materials have been studied as possible photoelectrodes for this because of their low-cost synthesis, good charge transport properties, excellent durability in aqueous electrolytes [9, 20], fairly acceptable photoelectrochemical and chemical corrosion stability [123]. And, most importantly, $BiVO_4$ has a narrow bandgap of approximately 2.4 eV with the absorption of visible light up to 520 nanometers, and a high-positive position of valance band that produce holes with strong oxidizing ability [124]. The monoclinic crystal form of $BiVO_4$ has been reported to have the highest photoactivity of 2.3 – 2.4 eV (by experiments) and 2.16 eV (by calculations) [123] and this form has the most potential to be used in water-splitting.

BiVO$_4$ coatings can be applied to biomedical devices to provide antibacterial properties, prevent the growth of bacteria, and reduce the risk of infection. A study, published in 2019, used *Hyphaene thebaica* dried fruit aqueous extracts to synthesize BiVO$_4$ nanorods, and managed to produce single phase of a space group I2/a with lattice parameters of (a) = 5.1 Å (b) = 11.7 Å, and (c) = 5.09 Å. Those nanorods were then exposed to many different types of bacteria and fungi. The different concentrations (1TCID50, 10TCID50, and 100TCID50) of poliovirus have been incubated with BiVO$_4$ nanorods, and the results confirmed the antiviral activity. Exactly 24 hours after the incubation, the cells were still viable, however, 5 days into the incubation process, the Hep2C cells were destroyed at all three concentrations. This suggests that the BiVO$_4$ nanorods managed to suppress the spread of the polio virus within the Hep2C cells. The study proposed that the antimicrobial properties also depend on the surface morphology, size, shape and the coating of the nanorods [11]. Other studies explored and proved BiVO$_4$ antimicrobial activities against *Staphylococcus aureus, Klebsiella pneumonia, Micrococcus luteus, Salmonella typhimurium, Salmonella paratyphi-B, Candida albicans, Candida krusei* and others, as well as excellent antiviral activities against human rhabdomyosarcoma cells (RD) and L20B cells [125].

In addition to medical applications, these properties of BiVO$_4$ also allow the material to be used for degradation of various pollutants in the water, such as organic dyes or pharmaceutical waste. Other materials, such as nickel ferrite, can be added to improve their photocatalytic properties, and in the case of the latter, BiVO$_4$/NiFe$_2$O$_4$ composites can photodegrade the methylene blue under visible light. After only 90 minutes of exposure under visible light, the BiVO$_4$/NiFe$_2$O$_4$ composites degraded the methylene blue with approximately 99% success rate [126]. Due to its narrow band-gap, BiVO$_4$ makes an excellent material to solve the pharmaceutical and organic dye waste issue.

2. EXPERIMENTAL

This section reveals the characteristic peculiarities of the aqueous tartaric acid-assisted sol-gel preparation technique. Moreover, the description of used materials, reagents and equipment is also included.

2.1. Materials and reagents

The materials and reagents for corresponding syntheses were purchased from the suppliers, listed with each material description. The name of the compound, its formula, purity, and supplier are given next: aluminium (III) nitrate nonahydrate, $Al(NO_3)_3 \cdot 9H_2O$, 99 %, Alfa Aesar; bismuth (III) oxide, Bi_2O_3, 99.99%, Alfa Aesar; lanthanum (III) oxide, La_2O_3, 99.9 %, Alfa Aesar; lithium nitrate, $LiNO_3$, 99 %, Alfa Aesar; molybdenum (VI) oxide, MoO_3, 99.95%, Alfa Aesar; titanium powder, Ti, 99.4 %, Alfa Aesar; vanadium (V) oxide, V_2O_5, 99.8%, Alfa Aesar.

The chelating agent for the complexation of metal ions and reagents for the control of pH in the aqueous solution are presented as follows: L–(+)–tartaric acid, $C_4H_6O_6$, 99.5%, Roth; ammonia aqueous solution $NH_3 \cdot H_2O$, 25 %, Penta; hydrochloric acid, HCl, 35 – 38 % Chempur; nitric acid, HNO_3, 66% Reachem.

2.2. Synthesis methodology

The syntheses of different metal tartrate gel precursors for $LiAlMo_2O_8$, $Li_{0.35}La_{0.55}TiO_3$ and $5Bi_2O_3 \cdot V_2O_5$ ceramics were prepared by an aqueous sol-gel synthesis method by using tartaric acid as a chelating agent that interacts as a ligand at the molecular level with the reaction mixture during the both dissolution in water and sol–gel formation.

2.2.1. Preparation of Li–Al–Mo–O tartrate gel precursor

The general synthesis scheme of Li–Al–Mo–O tartrate gel precursor for $LiAlMo_2O_8$ ceramic is illustrated and presented in Fig. 22. In the first stage of this preparation technique, the powder of molybdenum (VI) oxide was dissolved in a small amount of concentrated ammonia aqueous solution.
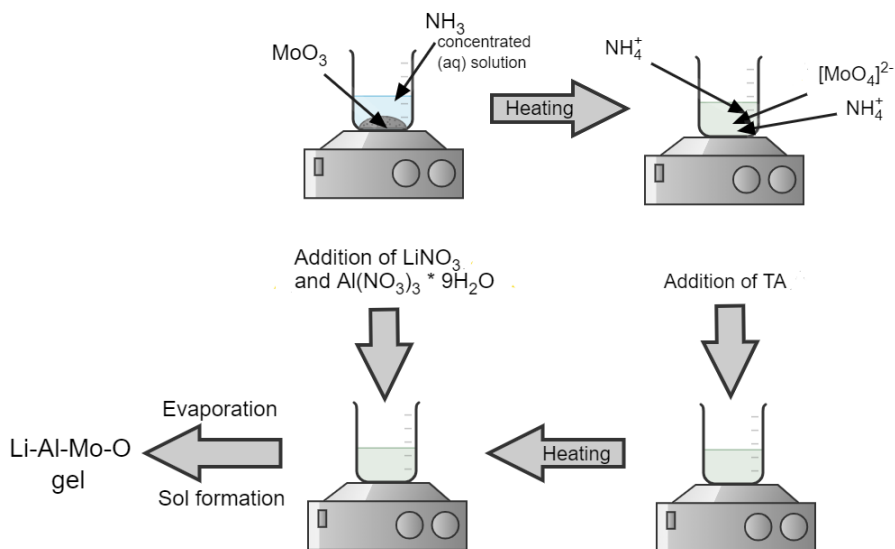
Fig. 22 Synthesis scheme of Li–Al–Mo–O tartrate precursor for LiAlMo$_2$O$_8$ ceramic

As shown in equation 1, the molybdenum (VI) oxide dissolves in hot concentrated ammonia solution forming NH$_4^+$ and MoO$_4^{2-}$ ions.

$$MoO_3 \text{ (s)} + 2 \, NH_3 \cdot H_2O \text{ (aq)} \rightarrow 2 \, NH_4^+ \text{ (aq)} + MoO_4^{2-} \text{ (aq)} + 2 \, H_2O \text{ (l)} \quad (1)$$
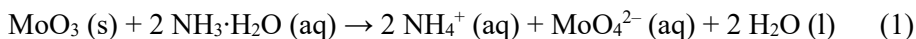
Excess ammonia is removed from the reaction mixture during further heating of the reaction mixture until 90 % of the water is evaporated. The addition of tartaric acid (TA) to the reaction mixture creates a coordination compound for $[(MoO_4)_p(C_4H_4O_6)_qH_r]^{(2p+2q-r)-}$ composition [127, 128]. The chemical reaction that occurred after this procedure can be written as shown in Eq. 2.

$$p \, (NH_4)_2MoO_4 \text{ (aq)} \; + \; q \, C_4H_6O_6 \text{ (aq)} \; \rightarrow$$
$$\rightarrow \; [(MoO_4)_p(C_4H_4O_6)_qH_r]^{(2p+2q-r)-} \text{ (aq)} \; + \; 2p \, NH_4^+ \text{ (aq)} \qquad (2)$$
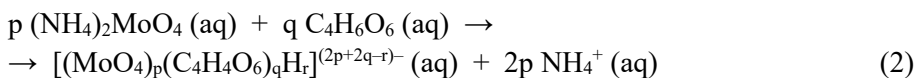
Such a protective environment against pH changes is easily created by the tartaric acid, which coordinates the corresponding molybdate complexes and prevents the occurring hydrolysis reaction that results in the formation of precipitates. Next to that followed the addition of lithium (I) nitrate and

aluminium (III) nitrate nonahydrate into the reaction mixture, the obtained clear solution was additionally stirred in an open beaker at 85 ºC – 90 ºC for several hours. Finally, a clear pale yellowish sol of corresponding metal ions was obtained and subsequently concentrated by slowly vaporizing the reaction mixture at 90 ºC. After drying in an oven at 120 ºC, fine-grained light yellow gel powders were obtained.

2.2.2. Preparation of Li–La–Ti–O tartrate gel precursor

Li-La-Ti-O tartrate gel precursors for $Li_{3x}La_{2/3-x}TiO_3$ (x=0.10, 0.12, 0.14, and 0.16) have been prepared. The general synthesis scheme of Li–La–Ti–O tartrate gel precursor for $Li_{0.35}La_{0.55}TiO_3$ ceramic is illustrated and presented in Fig. 23, respectively.

In the first stage of this preparation technique, the titanium powders were dissolved in a concentrated aqueous solution of hydrochloric acid. As shown in equation 3, the titanium is attacked by hot HCl, forming Ti(III) and H_2 [129].

$$2\ Ti\ (s)\ +\ 6\ HCl\ (aq)\ \rightarrow 2\ Ti^{3+}\ (aq)\ +\ 6\ Cl^-\ (aq)\ +\ 3\ H_2\ (g) \qquad (3)$$
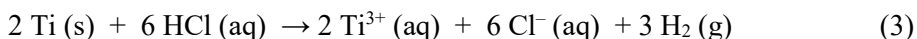
This chemical process is confirmed by the formation of the purple aqua ion $[Ti(OH_2)_6]^{3+}$ in the reaction mixture. Knowing that this coordination particle is a strong reductant (Equation 4), the aqueous solutions of Ti(III) must be protected from aerial oxidation.

$$[TiO]^{2+}\ (aq)\ +\ 2\ H^+\ (aq)\ +\ e^-\ \leftrightarrow\ Ti^{3+}\ (aq)\ +\ H_2O\ (l) \quad (E^o = +0.1\ V) \quad (4)$$
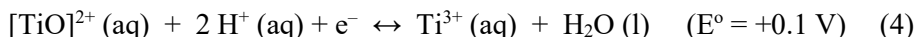
Such a protective environment against oxidation is easily created by the tartaric acid, which coordinates the corresponding titanium complexes and prevents from the hydrolysis and the formation of precipitates in the form of $TiO_2 \cdot 2\ H_2O$. Nevertheless, the oxidation of Ti^{3+} ions has occurred straight after adding lithium nitrate into the reaction mixture. As a result, a large number of nitrogen dioxide gases were released and the purple color of the solution disappeared. The following formation of a clear colorless aqueous solution is characterized by equation 5.

$$Ti^{3+}\ (aq)\ +\ 2\ H^+\ (aq)\ +\ NO_3^-\ (aq)\ \rightarrow\ Ti^{4+}\ (aq)\ +\ NO_2\ (g)\ +\ H_2O\ (l) \quad (5)$$
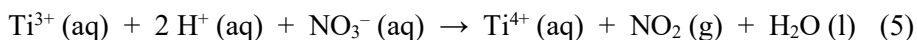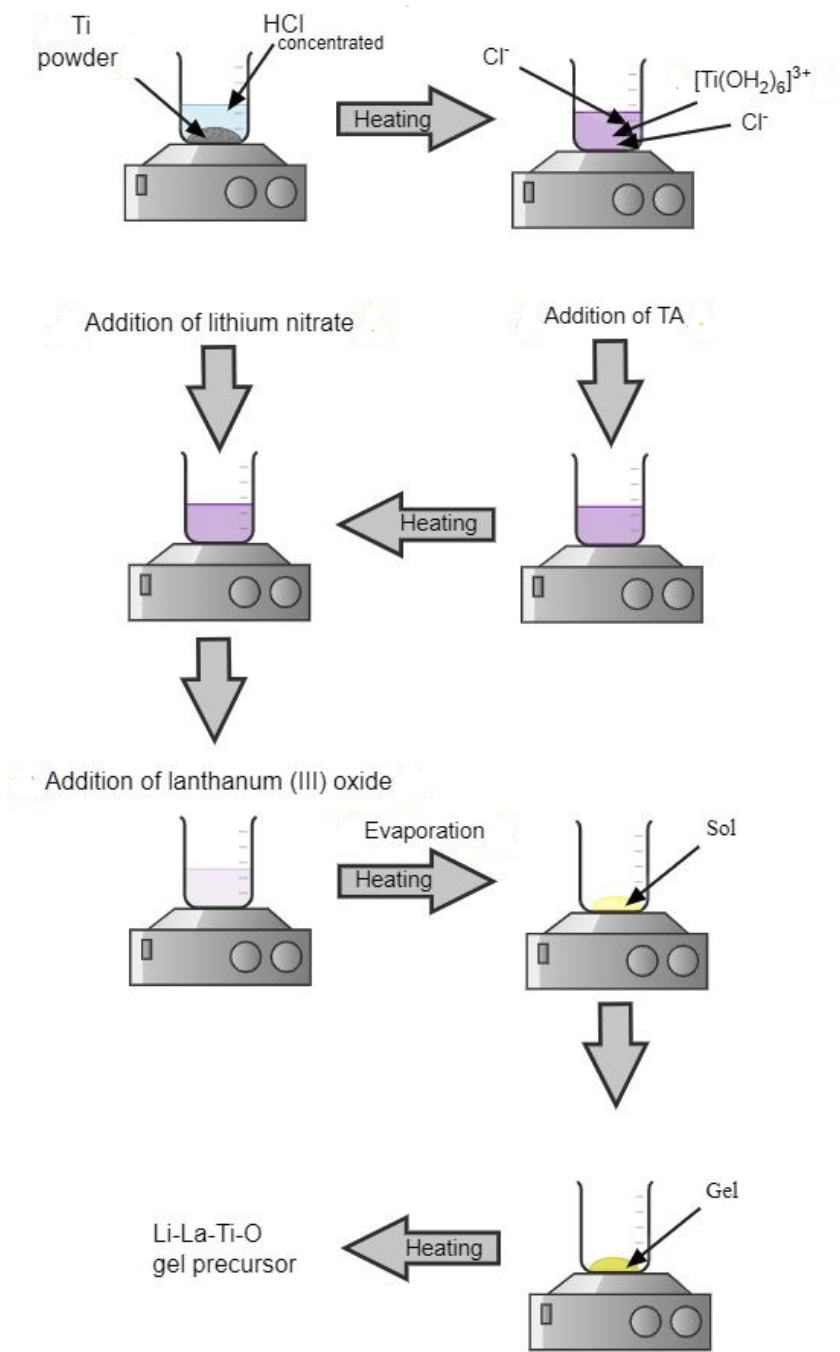
Fig. 23 Synthesis scheme of Li–La–Ti–O tartrate precursor for $Li_{0.35}La_{0.55}TiO_3$ ceramic

The absence of precipitates in the reaction mixture confirmed the importance of tartaric acid as a ligand during the stabilization of Ti(IV) ion in the aqueous solution and preventing its hydrolysis according to equation 6.

$$[Ti(OH_2)_6]^{4+} \text{ (aq)} + 4 H_2O \text{ (l)} \rightarrow TiO_2 \cdot 4 H_2O \text{ (s)} + 4 H_3O^+ \text{ (aq)} \quad (6)$$

The exact amount of tartaric acid, which replaces aqua ligands and coordinates the Ti^{4+} ion, could be successfully identified from the thermal decomposition of a Li–La–Ti–O tartrate gel precursor. The addition of lanthanum (III) oxide creates the final composition of Li–La–Ti–O tartrate gel precursor for $Li_{0.35}La_{0.55}TiO_3$ ceramic. A clear colorless aqueous solution of the corresponding metal ions was obtained and subsequently concentrated by slowly vaporizing the reaction mixture at 90 °C. After drying in an oven at 120 °C, fine-grained light yellow gel powders were obtained.

2.2.3. Preparation of Bi–V–O tartrate gel precursor

In the first stage of the synthesis of Bi–V–O tartrate gel precursors for $5Bi_2O_3 \cdot V_2O_5$ ceramic, bismuth (III) oxide and vanadium (V) oxide were dissolved in concentrated nitric acid (HNO_3, 66% Reachem). It is well known that in very acidic solutions, bismuth (III) exists in the form of the nonaaqua ion $[Bi(H_2O)_9]^{3+}$, which is similar to the aqua complexes of the lanthanide ions [130]. Partial hydrolysis of bismuth (III) salts leads to the formation of bismuth oxo clusters [131], which solubility in water significantly decreases, respectively. Thus, under the continuous stirring and heating at about 80 °C – 85 °C of temperature, it is possible to dissolve Bi_2O_3 in concentrated nitric acid as is shown in Fig. 24, according to equation equation 7, respectively.

$$Bi_2O_3 \text{ (s)} + 6 HNO_3 \text{ (aq)} + 15 H_2O \text{ (l)} \rightarrow$$
$$\rightarrow 2 [Bi(H_2O)_9]^{3+} \text{ (aq)} + 6 NO_3^- \text{ (aq)} \quad (7)$$
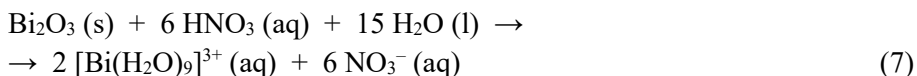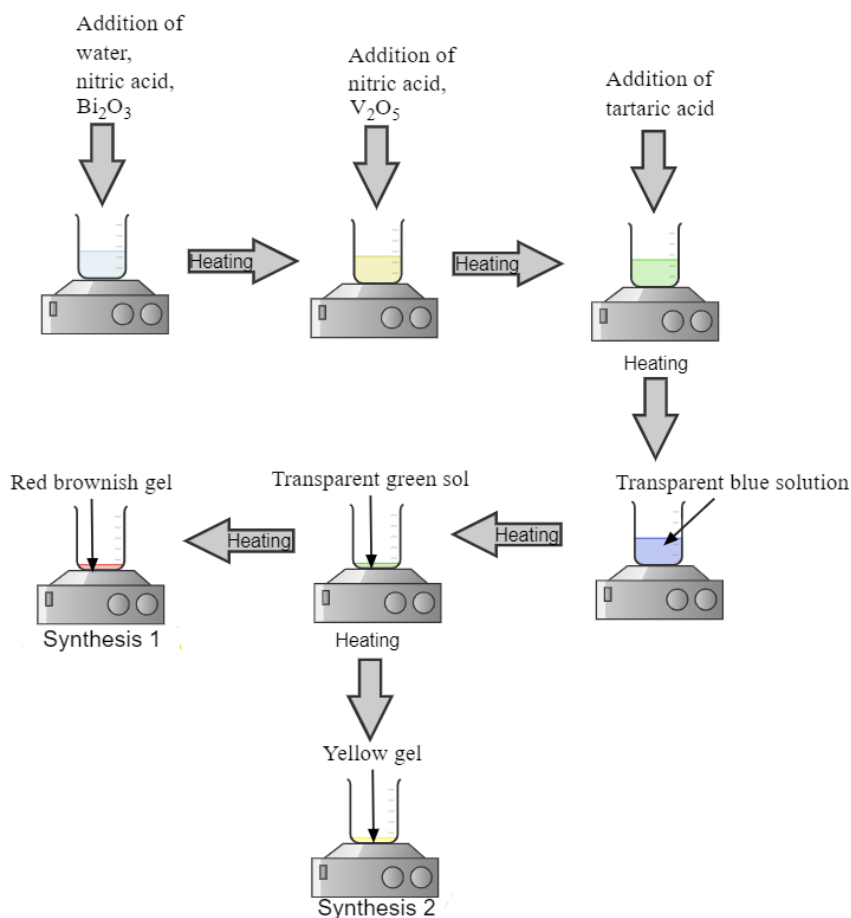
Fig. 24 Synthesis scheme for the Bi–V–O tartrate gel precursors

Meanwhile, vanadium (V) oxide is a red powder that sparingly dissolves in water but in a strongly acidic solution forms complexes of $[VO_2]^+$ [129]. In a contact with concentrated nitric acid, the dissolution of vanadium oxide corresponds the equation 8 as follows.

$$V_2O_5 \text{ (s)} + 2\ HNO_3 \text{ (aq)} \rightarrow 2\ [VO_2]^+ \text{ (aq)} + 2\ NO_3^- \text{ (aq)} + H_2O \text{ (l)} \quad (8)$$
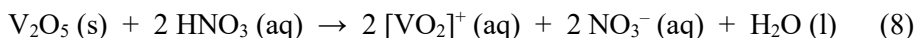
This process of the conversion into the $[VO_2]^+$ ion is quite fast and the dissolution of V_2O_5 in the acidic aqueous solution at the temperature of 80 °C – 85 °C requires only several minutes. The formation of the light yellow solution indicates that pervanadyl cation is surrounded by the nitrate ions.

The coordination capacity of nitrate ions in aqueous solution is lower than corresponding aqua ligands, thus, after the dissolution of metal oxides the composition of either $(Bi(H_2O)_9)^{3+}$, or $[VO_2]^+$ complexes is expected. Under the evaporation procedure and by the increasing the heating temperature of the reaction mixture, these ions tend to react with each other by forming the less soluble polynuclear complexes. This is the reason why the tartaric acid with molar ratios of Bi/TA = 0.25 (synthesis 1) and Bi/TA = 0.125 (synthesis 2) was added during the continuous stirring to the reaction mixture at the same temperature. Such addition of the ligand is required for the escalation of solubility via coordination of starting compounds in the reaction mixture; especially, during the pH changes and evaporation before the sol-gel formation.

After the addition of tartaric acid, the colour of the reaction mixture changed from light yellow into pale green. The continuous stirring and heating at 80 °C – 85 °C of temperature have gradually changed the appearance of the aqueous solution from green to bright blue colour. Such transformation of the reaction mixture corresponds to the coordination of metal cations by tartrates. The decrease of a wavelength of absorbed light, indicated by the colour change of the solution, confirms the increased coordination degree of metal ions with the residue of tartaric acid.

Thereafter, a clear solution was concentrated by vaporizing the reaction mixture at 90 °C. In the following stage, the blue solution gradually changed into a dark green transparent sol after nearly 95% of the water had been evaporated under continuous stirring. Finally, after drying in an oven at 120 °C, fine-grained red brownish (synthesis 1) and bright yellow (synthesis 2) gel powders were obtained.

2.2.4. Heat treatment of the different metal tartrate gel precursors

In order to synthesize the crystalline final compounds, the obtained different metal gel precursors were additionally heat-treated at high temperatures. For example, to show the crystal growth tendency, the well-milled Li–Al–Mo–O tartrate gel precursor was heat-treated at the temperatures of 400 °C, 450 °C, 500 °C, 550 °C, 600 °C, 650 °C, and 700 °C.

The heat treatment of the well-milled Li–La–Ti–O tartrate gel precursor was performed both to show the crystal growth tendency of obtained powder, and to enhance the compactness of the final ceramic. In this case, the corresponding sample was heat-treated at the temperatures of 800 °C, 900 °C, 1000 °C and 1100 °C in the air atmosphere. Finally, the obtained ceramic

powders were pelletized and additionally heat-treated at 1250 ℃ of temperature. The corresponding process of the heat treatment procedure and densification progress is shown in the scheme (Fig. 25) below.

Li-La-Ti-O tartrate gel precursor

Drying at 120 ℃ for 2 hours

Heat-treatment at 800 ℃, 900 ℃, 1000 ℃, and 1100 ℃ for 5 hours in the air atmosphere

Pressing into a pellet and additional densification under the thermal treatment at 1250 ℃ for 5 hours in the air atmosphere
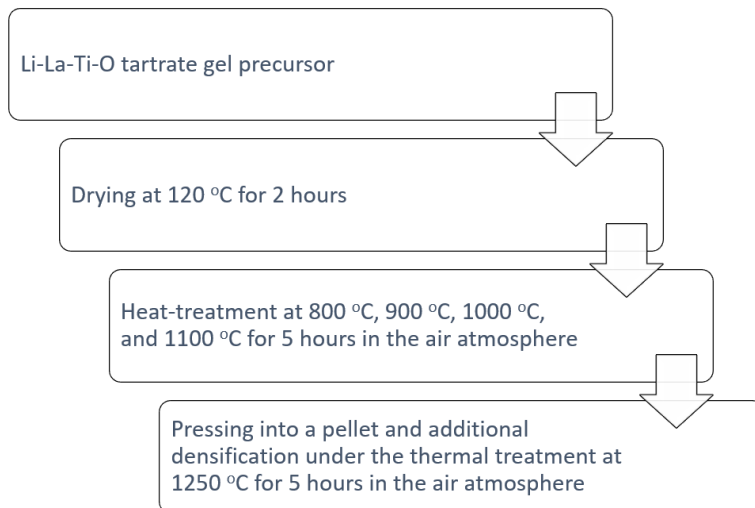
Fig. 25 Heat treatment scheme of Li–La–Ti–O tartrate precursor for $Li_{0.35}La_{0.55}TiO_3$ ceramic

Finally, the Bi–V–O tartrate gel precursors for $5Bi_2O_3 \cdot V_2O_5$ ceramics were heat-treated for 5 h at 800 ℃. The obtained yellowish ceramic powders were pelletized and additionally heat-treated at 870 ℃ for 5 h in the air.

2.3. Devices and equipments for sample characterization

TG/DSC measurement of the Li–Al–Mo–O tartrate gel precursor was performed with TG–DSC, STA 6000 Perkin-Elmer instrument using a sample weight of about 5 mg and a heating rate of $20\,°\,min^{-1}$ under the continuous air flow ($20\ cm^3\,min^{-1}$) at ambient pressure from room temperature to 950 ℃.

XRD patterns were recorded in air at room temperature by employing a powder X-ray diffractometer Rigaku MiniFlex II using Cu Kα radiation. XRD patterns were recorded at the standard rate of $1.5\ 2\theta\ min^{-1}$. The sample was spread on the glass holder to obtain the maximum intensity of the characteristic peaks in the XRD diffractograms. In order to evaluate the crystalline phase composition, the Rietveld refinement of the obtained XRD patterns was performed using X'Pert HighScore Plus software.

The scanning electron microscopes (SEM) Hitachi SU-70 and Hitachi TM3000 were used to study the surface morphology and the microstructure of the obtained ceramic samples. In addition, energy-dispersive X-ray spectroscopy (EDS) was applied for determining the elemental composition of $Bi_2O_3 \cdot V_2O_5$ ceramics.

The characteristic vibrations of the functional groups in all heat-treated samples were estimated using a Perkin-Elmer Frontier FTIR spectrometer. Fourier transform infrared (FTIR) spectra were obtained in the range of 4000–500 cm^{-1} with a 8 cm^{-1} resolution. The background was synthetic air.

The measurements of electrical properties were performed using two different impedance spectroscopy techniques by a newly developed impedance spectrometer [132-134]. Heat-treated ceramics were processed obtaining cylindrical samples of around 1.5 mm height and up to 3 mm diameter with Pt paste electrodes.

3. RESULTS AND DISCUSSION

This section contains the analysis results of the synthesized ceramics, which clearly shows the possibilities of the aqueous tartaric acid-assisted sol-gel preparation technique.

3.1. Thermal analysis of metal tartrates precursors

In this work, thermal analysis as a powerful tool was properly used for the combustion and pyrolysis processes of the as-prepared gel precursor, which play an important role during the formation of the final ceramic.

3.1.1. Thermal decomposition of the Li–Al–Mo–O precursor

The thermal treatment process of the Li–Al–Mo–O gel for $LiAlMo_2O_8$ ceramic was performed in the synthetic air atmosphere and the corresponding TG–DTG–DSC curves are shown in Fig. 26, respectively.

Fig. 26 Combined TG–DTG–DSC curves of the Li–Al–Mo–O tartrate gel precursor for $LiAlMo_2O_8$ ceramic by the heat-treating in the synthetic air atmosphere

In this case, the decomposition of the Li–Al–Mo–O tartrate gel precursor can be roughly divided into five main stages. The first mass change is directly related to an excess of tartaric acid, which has been added to the reaction mixture to avoid precipitation during the gelation process. This decomposition stage is well-seen from the TGA curve in the range of temperatures from 30 °C to 320 °C. Although the synthesized gel was dried at the temperature of 120 °C, the water molecules, which formed during the dimerization of tartaric acid (Equation 9), evaporated up to 125 °C. Such removal of moisture from the gel powder could be confirmed by the broad endothermic band in the DSC curve.

$$\text{(structure)} + \text{(structure)} \longrightarrow \text{(dimer structure)} + 2H_2O \quad (9)$$
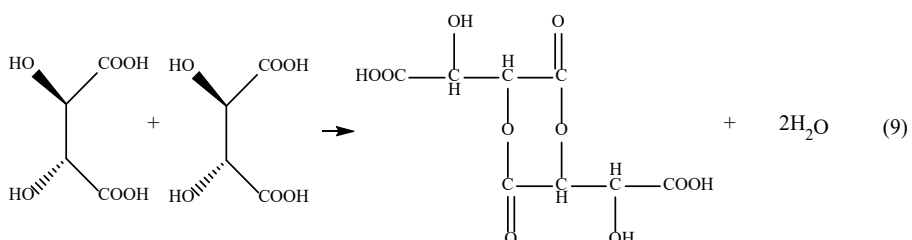
Further increase in temperature leads to the evaporation of acetic acid that forms after the decomposition of the tartaric acid dimer. This process starts at about 130 °C and ends at 175 °C. It is also confirmed by the well-expressed endothermic peak in the DSC curve and by the sharp band in the TGA curve. The exchange of hydrogen by hydroxyl group, known as Beckmann transformation, and the decomposition of an as-formed tartaric acid dimer are presented in equation 10, respectively.

$$\text{(structure)} \longrightarrow \text{(structure)} \longrightarrow \begin{array}{l} H_3C\!-\!COOH \\ CO + CO_2 \\ H_3C\!-\!COOH \end{array} \quad (10)$$

By further increasing the heating temperature, the formed tartaric acid dimer decomposes in a different manner. This process starts at 200 °C and ends above 300 °C. The release of carbon dioxide is confirmed by the broad exothermic band in the DSC curve. Meanwhile, the formation mechanism of pyruvic acid is shown in equation 11.

$$CO_2 \quad + \qquad\qquad\qquad\qquad \tag{11}$$
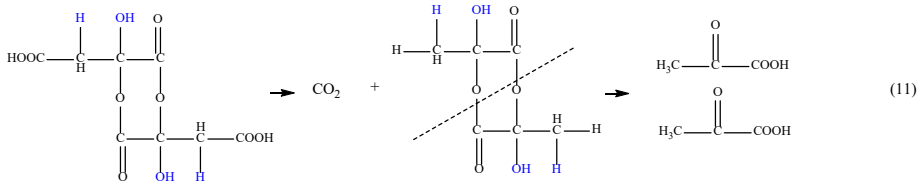
The total mass change in the temperature range of 30 ºC – 320 ºC consists of about 50 %, which is in good agreement with the amount of tartaric acid that was added to the reaction mixture at the beginning of the reaction. The further increase of the temperature from about 320 ºC to 500 ºC is directly related to the thermal decomposition of the metal tartrates. This is partially confirmed by the small and broad exothermic bands in the DSC curve. It is also important to note that from the temperature of 450 ºC, an endothermic process is distinguished in the DSC curve, which is associated with the beginning of the crystallization of multicomponent oxides. In the range of temperature from 540 ºC to 679 ºC, the occurring mass change (9.2 %) is directly related to the combustion processes of inorganic carbon, which formed during the partial decomposition of metal tartrates at lower temperatures. The mass increase of the residue of the gel precursor in the range of temperature from 679 ºC to 700 ºC is attributed to the formation of lithium peroxide, which absorbs the oxygen gas from lithium oxide as an impurity phase [135]. By further increasing the heating temperature above 730 ºC, the mass of the sample becomes stable. However, from 850 ºC, the mass change of the gel residue is observed, which is attributed to the decomposition of aluminium molybdate and the evaporation of molybdenum oxide.

Summarizing the results of the thermal analysis, it is obvious that the formation of the obtained $LiAlMo_2O_8$ ceramic is highly dependent on the molar ratio of the initial reactants in the reaction mixture. The relatively low crystallization temperature of $Al_2Mo_3O_{12}$ creates conditions for the formation of impurity compounds, the existence of which is evidenced by the increase in the mass of the residue of Li–Al–Mo–O tartrate gel precursor at the temperature of about 679 ºC. Moreover, the decrease in the mass of the sample powder above 850 ºC confirms the formation of aluminium molybdate in the crystalline mixture as an impurity phase.

3.1.2. Pyrolysis and combustion of the Li–La–Ti–O tartrate gel

In this work the proposed synthesis technique is mainly based on the interaction of metal ions in aqueous media with tartaric acid, which acts as a ligand during the gelation process by avoidance of the formation of precipitates, the detailed investigation of the synthesized Li–La–Ti–O tartrate gel precursor plays an important role in the frame of both its thermal decomposition mechanism, and the chemical and physical properties of the final multicomponent oxide. The thermogravimetric and differential scanning calorimetric analysis that allows both the evaluation of the decomposition process of lithium lanthanum titanium tartrate gel and the crystallization path of the final multicomponent oxide is particularly convenient for the implementation of such a task. Therefore, in this case, the TG–DTG–DSC curves of the as-prepared Li–La–Ti–O tartrate gel precursor measured at different conditions are presented in Fig. 27, respectively.

The nature of the data shows two important things, the decomposition mechanism of organometallic compounds and the formation behavior of the final ceramic phases during the heat treatment. Moreover, the heat-treating of the samples in different atmospheres revealed interesting trends of the gel behaviour, especially at the temperatures above 300 ºC. From this point of view, the thermal decomposition of the resulting gels can roughly be divided into three main stages. On the other hand, depending on the heating atmosphere, the number of thermal exposure stages may vary slightly because of the combustion of organic compounds, which is promoted rather in an air-enriched environment, whereas the inert conditions initiate internal rearrangements in the gel precursor, and the evaporation of the volatile components occurs at slightly elevated temperature. Nevertheless, in the first range of temperature from 30 ºC to 300 ºC, the salts of the corresponding metal tartrates are relatively stable, however, the decomposition of the unreacted tartaric acid [128, 136, 137] occurred identical independently either the oxidative or inert environment. This is evidenced by the numerical values of these physicochemical transformations, which are given in Tables 2 and 3, respectively.
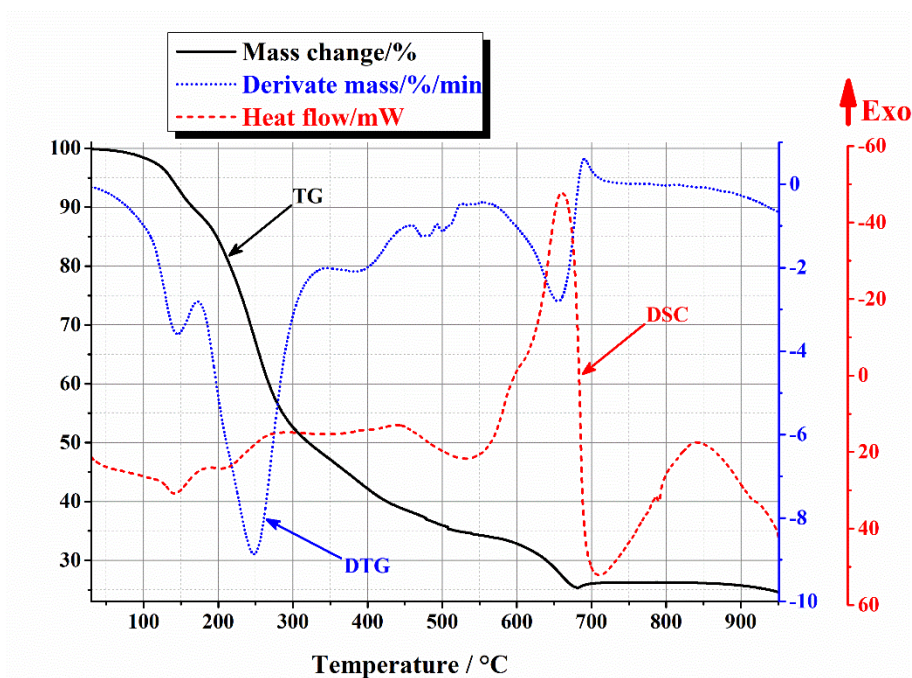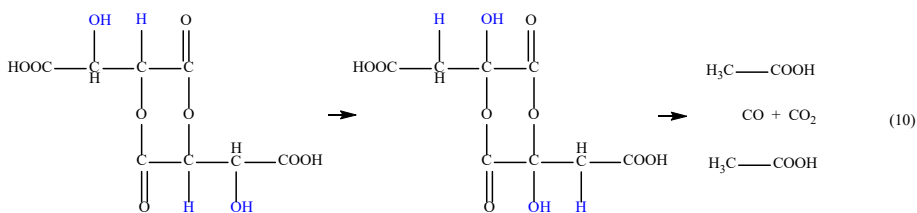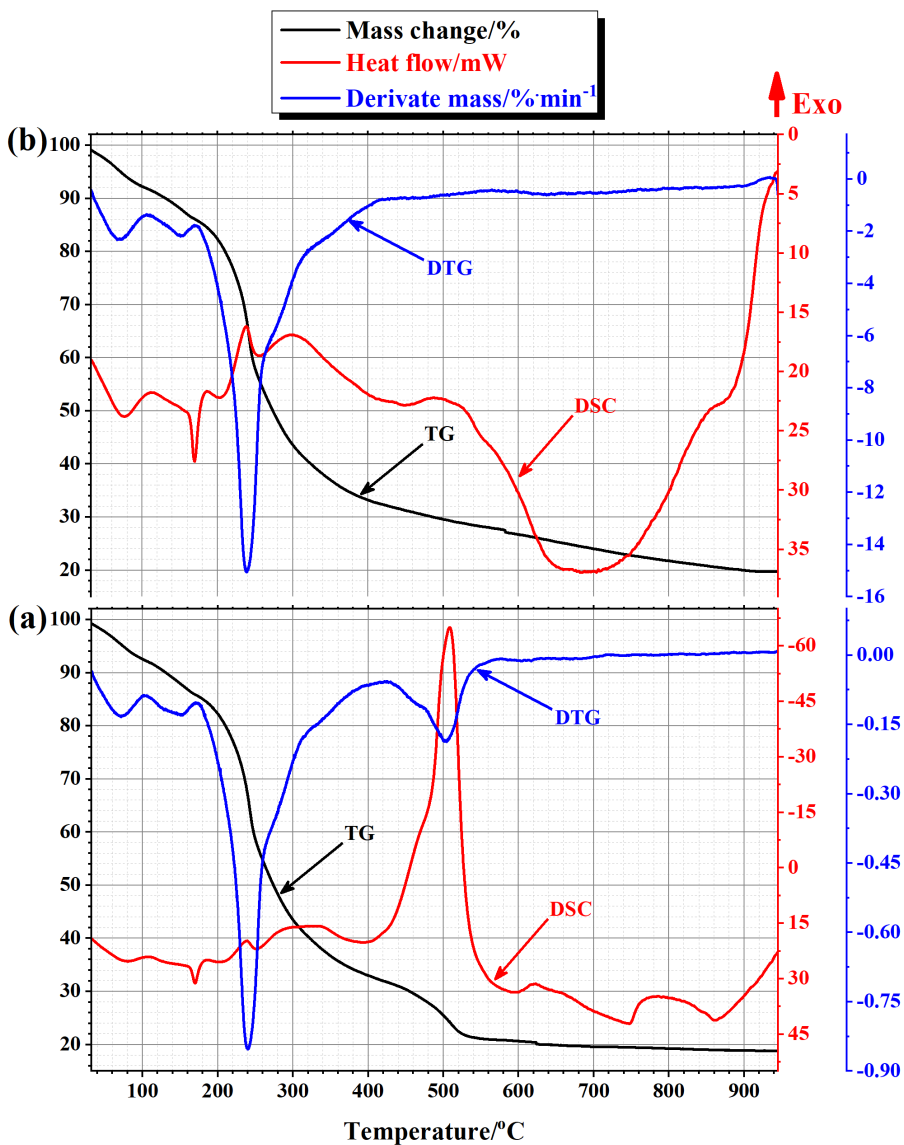
Fig. 27 Combined TG–DTG–DSC curves of the Li–La–Ti–O tartrate gel precursor for $La_{0.55}Li_{0.35}TiO_3$ ceramic by the heat-treating in the synthetic air (a) and nitrogen (b) atmospheres

Table 2 Thermoanalytical data of the Li–La–Ti–O tartrate gel precursor by heat-treatment in the air atmosphere

Stage No.	Range of temperature/ºC	Mass			Heat					
		Change/%	Onset/ºC	Residual/%	Flow/mJ	Onset/ºC	Peak/ºC	End/ºC		Enthalpy/J·g^{-1}
	30.74 – 253.71	42.391	–	57.020	1712.697	–	–	–	–	296.543
	30.74 – 106.93	7.359	51.14	92.052	403.358	39.71	72.94	103.25	endo	69.839
	72.94 – 132.91	5.331	77.05	89.792	−144.059	84.83	106.93	127.19	exo	−24.943
	106.93 – 162.23	5.462	141.97	86.590	34.454	114.48	132.91	148.58	endo	5.966
I	132.91 – 170.24	3.959	148.59	85.833	−208.450	127.89	162.23	168.85	exo	−36.092
	162.23 – 181.93	1.765	171.59	84.825	123.797	164.27	170.24	176.97	endo	21.435
	170.24 – 211.28	6.077	191.88	79.756	−272.707	171.13	181.93	211.50	exo	−47.218
	181.93 – 237.66	15.997	210.57	68.828	230.659	187.21	211.28	232.43	endo	39.937
	211.28 – 253.71	22.736	213.97	57.020	−175.975	217.19	237.66	248.32	exo	−30.570
I – II	237.66 – 320.79	28.603	–	40.225	988.838	–	–	–	–	171.261
	237.66 – 320.79	28.603	286.66	40.225	238.476	240.43	253.83	277.55	endo	41.291
II	253.71 – 415.92	24.863	–	32.157	3879.072	–	–	–	–	671.638
	253.71 – 415.92	24.863	280.72	32.157	−1324.748	258.46	320.79	373.14	exo	−229.372
	320.79 – 467.88	11.280	334.27	28.945	4870.171	341.25	415.92	467.42	endo	843.241
III	415.92 – 577.41	11.355	–	20.802	16021.790	–	–	–	–	2774.077
	415.92 – 577.41	11.355	496.29	20.802	−13143.089	475.131	509.30	531.48	exo	−2275.648
	535.31 – 623.13	1.072	535.43	20.379	887.230	545.81	577.41	616.56	endo	153.619
IV	577.41 – 747.90	1.353	–	19.449	2308.334	–	–	–	–	399.674
	577.41 – 747.90	1.353	623.23	19.449	−973.121	605.08	623.13	672.41	exo	−168.490
V	747.90 – 786.39	0.146	–	19.303	1710.118	–	–	–	–	296.097
	623.13 – 786.39	0.977	623.62	19.303	1783.195	659.69	747.90	759.98	endo	308.750
	747.90 – 864.33	0.668	781.28	18.965	−1637.041	750.74	786.39	819.15	exo	−283.444
VI	786.39 – 946.49	0.540	–	18.763	3834.418	–	–	–	–	663.907
	786.39 – 946.49	0.540	927.80	18.763	3015.897	803.95	864.33	935.15	endo	522.185

Table 3 Thermoanalytical data of the Li–La–Ti–O tartrate gel precursor by heat-treatment in the nitrogen atmosphere

Stage No.	Range of temperature/ºC	Mass			Heat					
		Change/%	Onset/ºC	Residual/%	Flow/mJ	Onset/ºC	Peak/ºC	End/ºC		Enthalpy/J·g⁻¹
I	30.74 – 237.40	30.231	–	69.136	1359.528	–	–	–	–	257.170
	32.10 – 106.30	7.011	68.30	92.356	409.631	41.09	72.84	104.45	endo	77.479
	72.84 – 136.40	5.242	89.74	90.067	−139.868	82.51	106.30	129.33	exo	−26.455
	106.30 – 162.23	5.033	132.49	87.322	10.492	117.69	136.40	148.64	endo	1.985
	136.40 – 169.99	3.399	139.42	86.667	−140.450	137.88	162.23	168.41	exo	−26.565
	162.23 – 181.10	1.622	175.48	85.701	113.902	164.16	169.99	177.01	endo	21.544
	169.99 – 211.42	6.327	200.37	80.340	−208.112	171.30	181.10	194.68	exo	−39.363
	181.10 – 237.40	16.565	211.73	69.136	223.847	187.21	211.42	232.85	endo	42.339
	211.42 – 254.84	23.572	225.35	56.768	−226.715	216.74	237.40	249.51	exo	−42.882
I – II	237.40 – 305.80	25.849	–	43.287	639.564	–	–	–	–	120.969
	237.40 – 305.80	25.849	237.10	43.287	206.059	240.43	254.84	285.85	endo	38.975
II	305.80 – 502.86	13.207	–	30.080	2267.512	–	–	–	–	428.885
	254.84 – 410.68	23.421	258.10	33.348	−640.294	261.06	305.80	392.05	exo	−121.107
	305.80 – 502.86	13.207	307.55	30.080	784.451	338.18	410.68	469.05	endo	148.374
III	502.86 – 893.33	9.063	–	21.017	10073.951	–	–	–	–	1905.419
	410.68 – 682.55	8.002	583.76	25.345	−2325.827	418.70	526.61	626.40	exo	−439.914
	502.86 – 843.49	8.268	749.29	21.811	8152.467	578.63	682.55	815.44	endo	1541.984
	682.55 – 893.33	4.329	766.62	21.017	−279.310	801.87	843.49	827.88	exo	−52.830
IV	893.33 – 945.48	0.246	–	20.771	775.105	–	–	–		146.606
	843.49 – 923.50	1.093	860.47	20.718	958.521	853.81	893.33	920.26	endo	181.298
	893.33 – 945.48	0.246	940.72	20.771	−295.844	907.40	923.50	890.11	exo	−55.957

With further increase of the temperature, the influence of the heating atmosphere reveals different trends on the decomposition of corresponding metal tartrates. From the obtained results, it is clear that the similarity of the thermal decomposition process of Li–La–Ti–O tartrate gel precursor ends at the temperature of about 254 °C. The nature of the exothermic process from 253.71 °C in the air and 254.84 °C in the nitrogen atmosphere indicates the start of the dominance of the environmental conditions to the further decomposition of the initial gel precursor. This broad exothermic band of the thermal decomposition process in the DSC curve competes with the subsequent endothermic effect, which starts at the temperature of 305.80 °C (in N_2) and 320.79 °C (in the air), respectively. Next to that, this endothermic process overlaps with the exothermic change starting in the range of temperature at about 410.68 °C to 415.92 °C depending on the heating atmosphere, which is attributed to the intramolecular rearrangement of metal tartrate residues and the onset of crystallization of Li–Ti–O, La–Ti–O and Li–La–Ti–O multicomponent oxides.

From Fig. 27, there is clear that the heat treatment of the Li–La–Ti–O tartrate gel precursor in the air atmosphere from 415.92 °C to 577.41 °C causes a pronounced combustion process of its residual organic part, which is 5.65 times brighter than the analogous broad exothermic effect indicated by the DSC curve in the nitrogen environment. Such a strong dominance of the atmosphere during the thermal treating clearly shows that the final oxidation of metal tartrate residues, which starts at the temperature of 450 °C, and the mechanism of its change behaviour strongly depend on the oxidizing capacity of the environment.

Meanwhile, the crystallization of the corresponding metal titanates occurs at about 500 °C (Fig. 27 (b)), however, the same endothermic effect in the DSC curve for the Li–La–Ti–O precursor, which was heat-treated in the air atmosphere, starts at a slightly later stage at the temperature of 550 °C due to the parallel intensive combustion of gel residues (Fig. 27 (a)). Besides, according to the results based on XRD analysis and the estimation of the trends in the nature of the DSC curves, the crystallization of lithium and lanthanum titanate tends to start at 550 °C. It is most likely that the pronounced onset of the last endothermic effect in the DSC curves (Fig. 27), in the range of temperature from 800 °C to 850 °C, is attributed to the crystallization process of lithium and lanthanum titanate residues as illustrated in the equation 12.

$$x \text{ Li–Ti–O (s)} + y \text{ La–Ti–O (s)} \rightarrow x\text{Li–}y\text{La–}(x + y)\text{Ti–O (s)} \qquad (12)$$
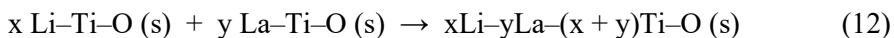
Thus, summarizing the obtained results of the thermal decomposition of Li–La– Ti–O tartrate gel precursor in different heating atmospheres, it is clear that the thermal analysis is a powerful and essential tool, which enables the substantiation and explanation of the formation peculiarities of the final crystalline oxide materials. In addition, the combination of thermal analysis and X-ray diffraction enables the possibility of explaining the causes and nature of the formation of crystalline phases during the thermal decomposition processes of the initial Li–La–Ti–O tartrate gel precursor.

3.1.3. Thermal degradation of the Bi–V–O tartrate gel precursor

The chemical stability of volatile compounds in the Bi–V–O tartrate gel precursors, prepared in the sol-gel process using a different amount of tartaric acid, is seen from the TG–DTG–DSC curves in Fig. 28, respectively.

Despite the similar tendencies of the thermal behaviour of the analysed Bi–V–O gel precursors in the DSC curve, the overall mass change completely differs. The sample prepared using synthesis route 1 corresponds to the best match of the mass residue of 64.6 % at the temperature of 800 °C comparing with the theoretical case (62.1 %). The final decomposition of another Bi–V–O gel precursor (synthesis 2) consists of 68.9 % of the remaining mass and completely mismatches the theoretical mass change, which creates at least 29.0 % of the ceramic residue. Such difference is explained by the formation of stabile metal carbonates and by the corresponding carbon-based compounds trapped in the Bi–V–O network during the evaporation and heat-treatment procedures. These ceramic systems remain stable even above the temperature of 800 °C.

As is known from the earlier investigations, the thermal decomposition of the tartaric acid occurs up to 300 °C. However, despite that fact that the amount of the tartaric acid according to the synthesis way differs twice, the mass change in both cases was observed almost the same. This result indicates that the increased amount of tartaric acid in synthesis 2 strongly affects the Bi–V–O system during the gelation process. The change in colour of corresponding gel precursors proves this conclusion, besides, the strong endothermic character ($\Delta H = 45.581$ J g^{-1}) of the DSC curve (Fig. 28 (a)) and mass change of about 5% confirms the increased hydration of the corresponding gel precursor.

Further thermal treatment in the range of temperature from 100 °C to 200 °C also determines the higher mass change of about 10% for the gel precursor

obtained in the synthesis 1. Meanwhile, in the case of the synthesis 2, the mass change decreases only by 2%. The highest mass change of the Bi–V–O tartrate gel precursor (synthesis 2) is observed in the range of temperature from 220 °C to 300 °C when the weight decreases of about 25%. Such different behaviour of both TG curves in the range of temperature from 30 °C to 300 °C indicates the uneven influence of the Bi–V–O system coordinated by tartrates to the stability of tartaric acid, which remained unreacted in the reaction mixture. The further increase of temperature from the 300 °C to 470 °C shows the typical decomposition of metal tartrates for the synthesis 1 with the mass decrease of about 5.428%. In the case of the synthesis 2, the mass change was observed only about 1.5%. Such a relatively small amount of tartrates in the Bi–V–O tartrate gel precursor is not typical for this synthesis technique, and it could be explained only by the formation of stable metal-carbon-oxygen based compounds, which do not decompose even at elevated temperatures.

Finally, the last mass change in the range of temperature from 470 °C to 540 °C corresponds to the decomposition of tartrates residue. Meanwhile, the mass changes of about 4.049% (synthesis 1) and 2.198% (synthesis 2) agree with the mass loss values of the metal tartrates in the range of temperature from 300 °C to 470 °C. In conclusion, it is clear that the amount of tartaric acid plays an important role during the formation of Bi–V–O tartrate gel precursors. The deficiency of the tartaric acid during the sol-gel process creates the precipitation that strongly affects the homogeneity of the final gel precursor. Meanwhile, the excess of the ligand produces a significant amount of the Bi–V–O ceramic integrated with the carbon-based impurities, which maintain their stability even at the temperature above than 815 °C.
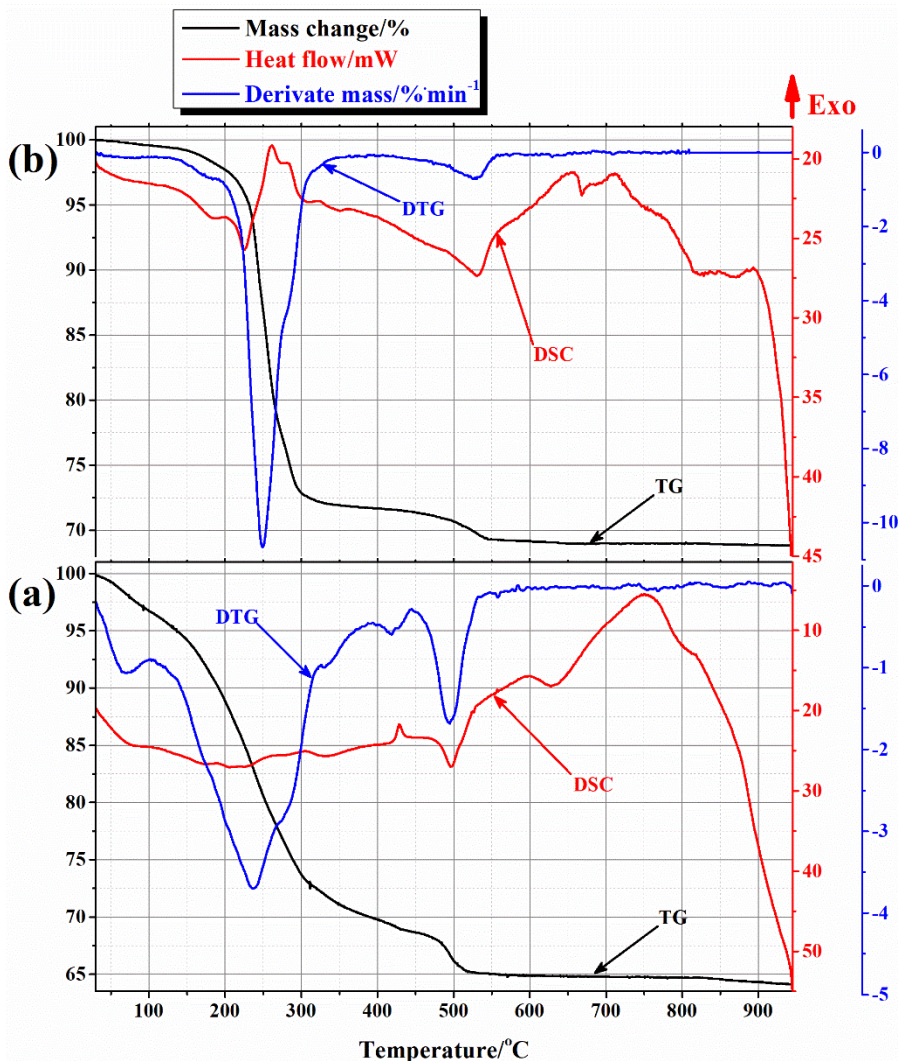
Fig. 28 The combined TG–DTG–DSC curves of the Bi–V–O tartrate gel precursors for $5Bi_2O_3 \cdot V_2O_5$ ceramic prepared by the synthesis 1 (a), and synthesis 2 (b), respectively

3.2. X-Ray diffraction patterns of the crystalline ceramics

X-ray diffraction analysis (XRD) is a non-destructive method of studying crystalline structures, which can be used to describe the crystalline structure of a material, identify chemical compounds and their varieties, and defects, and calculate crystallite sizes. Moreover, in this work, the XRD method is

successfully combined with the thermal analysis of the synthesized gels. The composition of the crystalline phases in the sample allows us to confirm the fact of crystallization processes developing during heat treatment because of the results of the thermal analysis, this transformation corresponds to both the absence of the sample mass change and the endothermic behaviour in the DSC curve.

3.2.1. Growth trends of crystallites for $LiAlMo_2O_8$ ceramic

In this work, XRD of Li–Al–Mo–O tartrate gel precursor for ceramic of initial composition of $LiAlMo_2O_8$ heat-treated at different temperatures was also performed. The corresponding X-ray diffraction patterns are presented in Fig. 29, respectively. Red colour represents $LiAlMo_2O_8$, blue – $Al_2Mo_3O_{12}$ crystalline phases.

The phase composition and estimation of the crystallite sizes for obtained ceramics were determined by the Rietveld refinement. The homogeneity of the as-synthesized gel precursor was proven by the lower diffractogram of Fig. 29, in which no characteristic peaks attributable to crystalline compounds were observed. As shown in the results of the thermal analysis, after the decomposition processes of the excess tartaric acid, the beginning of the crystallization of crystalline compounds is distinguished. Knowing that the formation of aluminium molybdate starts above the temperature of 400 ℃, the heat treatment of the sample at 450 ℃ leads to the formation of at least two different crystalline phases. Nevertheless, the composition of the remaining crystalline phases of the Li–Al–Mo–O gel precursor heat-treated at higher temperatures shows the dominance of the triclinic $LiAlMo_2O_8$ compound which amount tends to increase by increasing the heat-treatment temperature.
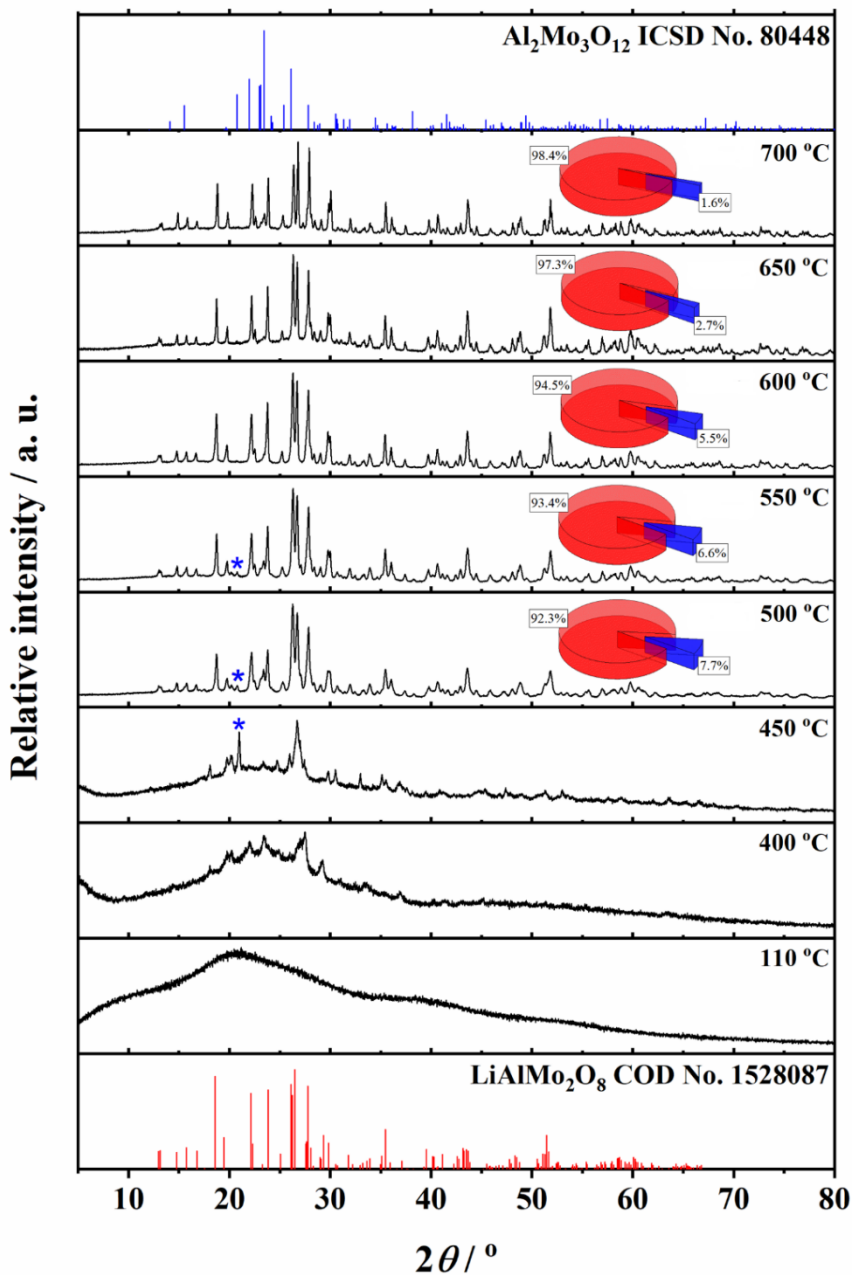
Fig. 29 Standard COD and ICSD cards for $LiAlMo_2O_8$ (red) and $Al_2Mo_3O_{12}$ (blue) crystalline phases and powder XRD patterns for Li–Al–Mo–O tartrate gel precursor sample dried at 110 °C and heat-treated at different temperatures

Meanwhile, the crystallite growth trends of the $LaAlMo_2O_8$ ceramic are shown in Fig. 30.
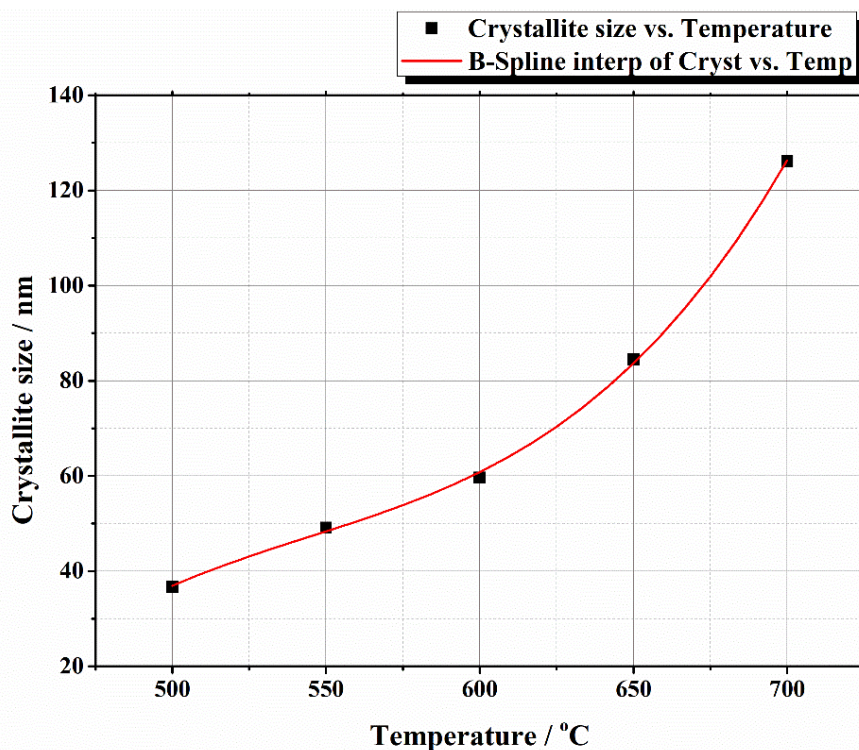
Fig. 30 Growth trends of the crystallites for $LiAlMo_2O_8$ ceramic

In this case, the size of crystallites increases exponentially from 36.75 nm for the sample heat-treated at 500 ºC to 126.11 nm at 700 ºC. It should also be noted that the existence of the impurity $Al_2Mo_3O_{12}$ crystalline phase coincides with the conclusions obtained by analyzing the results of the thermal analysis when the observed decrease in the mass of the sample above the temperature of 900 ºC was associated with the decomposition of aluminium molybdate and the removal of MoO_3 from the reaction mixture.

Summarizing the results obtained from XRD diffractograms, it can be concluded that the composition of the final crystalline phases in the reaction mixture significantly depends on the molar composition of the initial reagents. Thus, the increase in the heat-treatment temperature reduces the number of impurity phases in the reaction mixture, however, the synthesis of single-phase $LiAlMo_2O_8$ compound at lower temperature remains complicated.

3.2.2. X-Ray diffraction studies on the crystalline LLTO phases

In this work, XRD of Li–La–Ti–O tartrate gel precursor for ceramic of initial composition of $Li_{0.35}La_{0.55}TiO_3$ heat-treated at different temperatures was also performed; the corresponding X-ray diffraction patterns presented in Figs. 31, 32 and 33, respectively.

From the XRD patterns it is clearly seen that with the increase of the heat treatment temperature to 1000 ºC, the complete elimination of the characteristic peaks attributable to the impurity crystalline phases occurred. It was estimated that the size of crystallites for the tetragonal crystalline phase of $Li_{0.3}La_{0.567}TiO_3$ ceramic increased from 61.48 nm to 97.71 nm. In this heat treatment stage, the residues of lithium and lanthanum titanates react with lanthanum carbide. The corresponding characteristic peaks of the desired composition were successfully identified by the Rietveld refinement analysis. The obtained results are shown in Table 4.

The lack of titanium content in the mixture of crystalline compounds could be compensated by titanium oxide. The small amount of TiO_2 could be identified in XRD pattern of the sample, which was heat-treated at the temperature of 800 ºC. In this case, the characteristic reflections attributable to the crystalline titanium oxide overlap with the already identified peaks attributable to lithium and lanthanum titanates. It is important to note that after the thermal treatment of the sample above the temperature of 1000 ºC, the gradual transformation of the single-phase $Li_{0.3}La_{0.567}TiO_3$ tricomponent oxide into the crystalline phase of $Li_{0.35}La_{0.55}TiO_3$ was observed.

In such cases, the resulting ceramics are mainly composed of the orthorhombic phase of $Li_{0.35}La_{0.55}TiO_3$, which the mass fraction in the mixture consists of 91.3%.
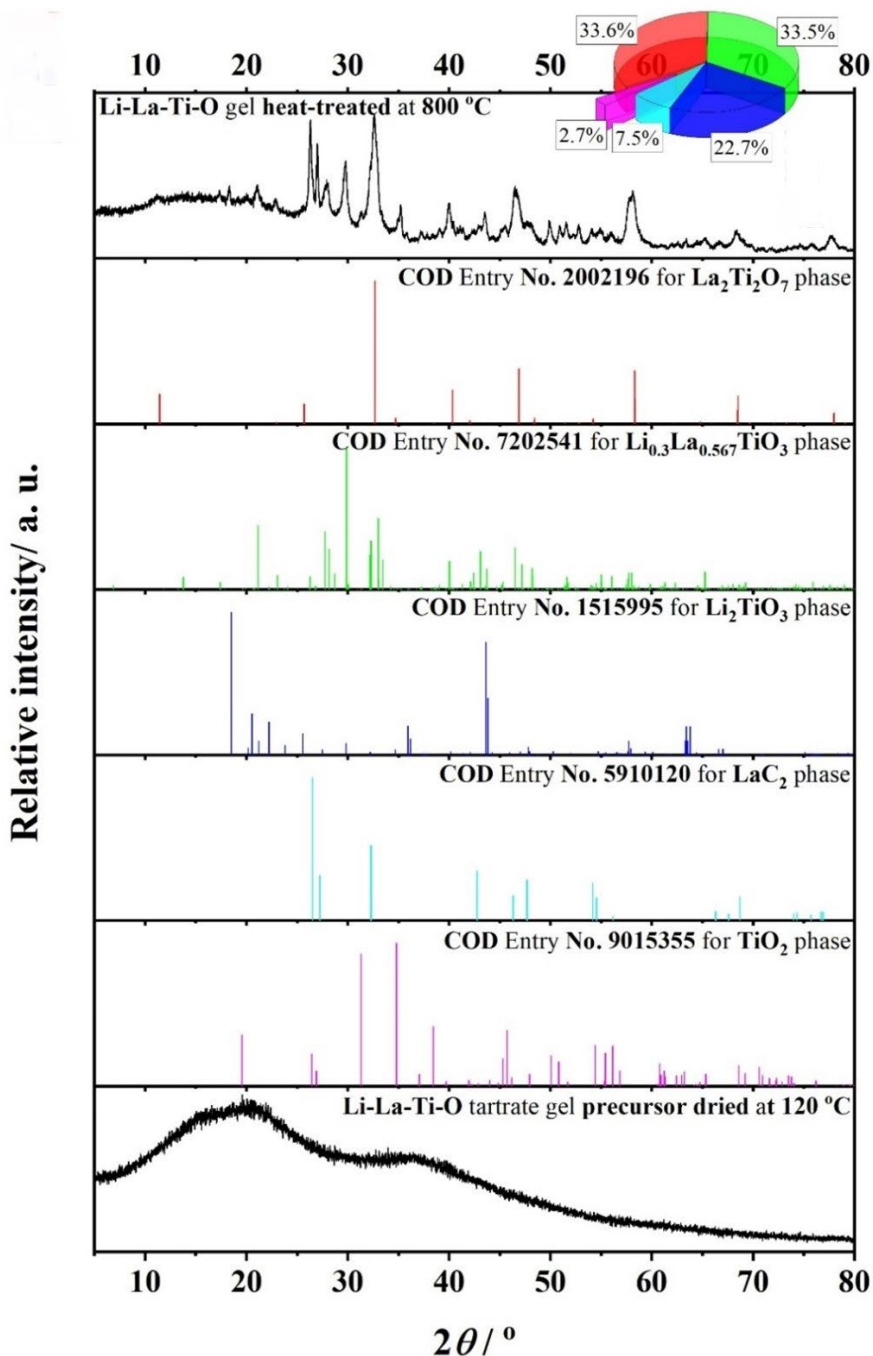
Fig. 31 Standard COD cards for $La_2Ti_2O_7$ (red), $Li_{0.3}La_{0.567}TiO_3$ (green), Li_2TiO_3 (dark blue), LaC_2 (light blue), TiO_2 (pink) crystalline phases and powder XRD patterns for Li–La–Ti–O tartrate gel precursor sample dried at 120 °C and heat-treated at 800 °C

74
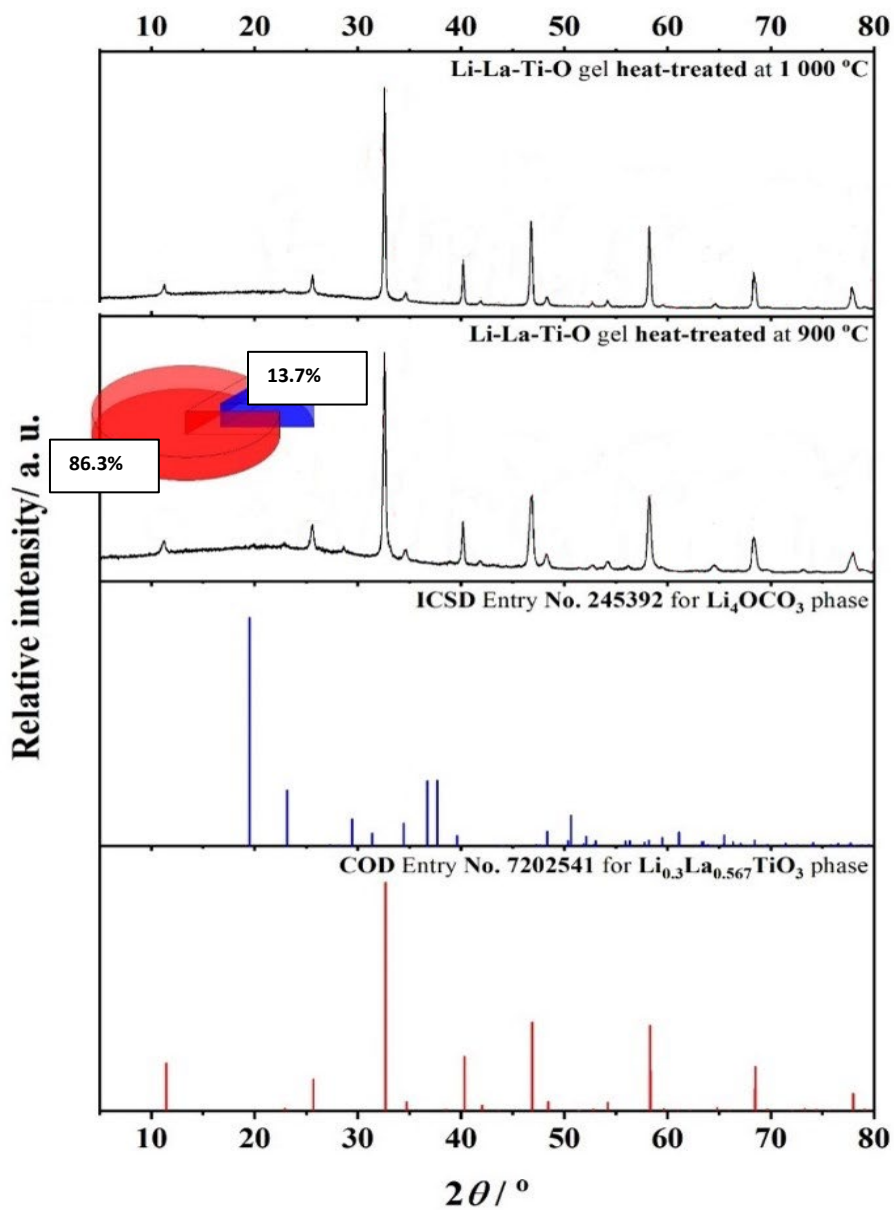
Fig. 32 Standard COD and ICSD cards for $Li_{0.3}La_{0.567}TiO_3$ (red), Li_4OCO_3 (blue) crystalline phases and powder XRD patterns for Li–La–Ti–O tartrate gel precursor sample heat-treated at 900 ºC and 1000 ºC of temperature
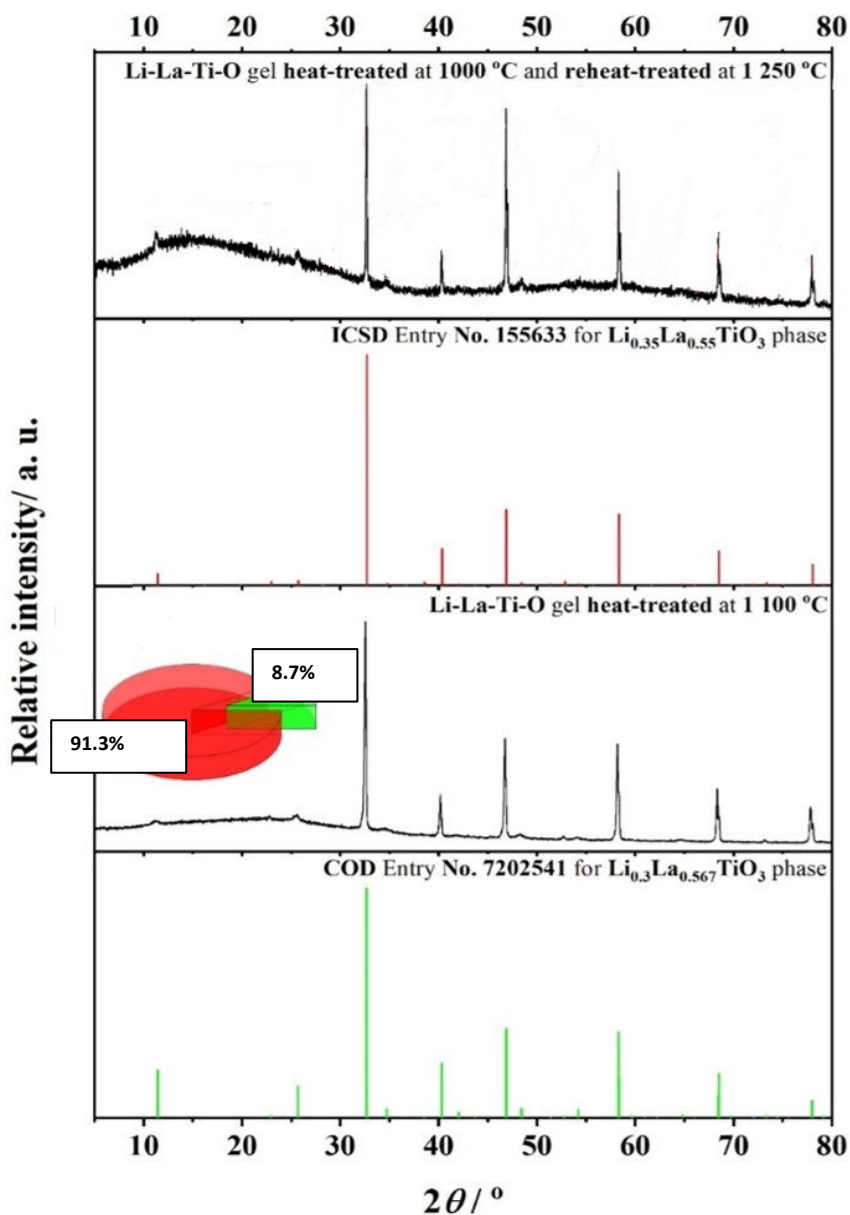
Fig. 33 Standard COD and ICSD cards for $Li_{0.3}La_{0.567}TiO_3$ (green), $Li_{0.35}La_{0.55}TiO_3$ (red) crystalline phases and powder XRD patterns for Li–La–Ti–O tartrate gel precursor sample heat-treated at 1100 °C and 1250 °C of temperature

Table 4 The phase composition, crystallite size, lattice parameters and agreement indices for $Li_{0.35}La_{0.55}TiO_3$ ceramic heated at different temperature

Heat-treating temperature / ºC	Crystal phase formula	Crystal system	Mass fraction /%	Crystal-lite size/nm	Unit cell			Weighted R profile	Goodness of fit
					a/pm alpha/º	b/pm beta/º	c/pm gamma/º		
800	$La_2Ti_2O_7$	orthorhombic	33.6	23.55	2569.584	781.796	554.057	14.467	2.590
					90.000	90.000	90.000		
	$Li_{0.3}La_{0.567}TiO_3$	tetragonal	33.5	23.17	548.869	548.869	771.678		
					90.000	90.000	90.000		
	Li_2TiO_3	monoclinic	22.7	2.79	797.277	3790.453	2627.721		
					90.000	175.812	90.000		
	LaC_2	tetragonal	7.5	26.78	392.601	392.601	658.031		
					90.000	90.000	90.000		
	TiO_2	monoclinic	2.7	2791.27	459.412	481.954	471.805		
					90.000	99.006	90.000		
900	$Li_{0.3}La_{0.567}TiO_3$	tetragonal	86.3	61.16	547.065	547.065	777.080	12.231	2.193
					90.000	90.000	90.000		
	Li_4OCO_3	monoclinic	13.7	2791.27	665.926	196.745	126.568		
					90.000	101.303	90.000		
1000	$Li_{0.3}La_{0.567}TiO_3$	tetragonal	100.0	94.34	547.239	547.239	775.860	12.074	2.042
					90.000	90.000	90.000		
1100	$Li_{0.35}La_{0.55}TiO_3$	orthorhombic	91.3	79.58	774.351	774.209	773.723	13.833	2.729
					90.000	90.000	90.000		
	$Li_{0.3}La_{0.567}TiO_3$	tetragonal	8.7	82.03	549.422	549.422	775.065		
					90.000	90.000	90.000		
1250	$Li_{0.35}La_{0.55}TiO_3$	orthorhombic	100.0	110.64	774.610	773.459	773.991	14.018	2.096

It should be also mentioned that the molar ratio of lithium and lanthanum ($n(Li)/n(La)$=0.648) in the determined mixture is really close to the molar composition of $Li_{0.35}La_{0.55}TiO_3$ ceramic. The excess of lithium ions (x=0.67) is removed from the mixture of oxides during the recrystallization of the final crystalline compound at the temperature of 1250 °C. From this result, it is clear that the ratio of chemical elements in the $Li_{0.35}La_{0.55}TiO_3$ ceramic is controlled by the amount of lanthanum in it.

Finally, after additional heat treatment of the obtained ceramic at the temperature of 1250 °C for 5 hours in the air atmosphere, a single-phase oxide of $Li_{0.35}La_{0.55}TiO_3$ composition [138] was obtained, in which, the estimated size of the crystallites corresponds to 110.64 nm. Summarizing the results obtained from the XRD analysis, it is obvious that the formation of the final lithium lanthanum titanate ceramic starts at a relatively high temperature, above 500 °C. In this case, the initial crystallization of lithium titanate intermediate allows to reduce the volatility of lithium ions, especially in the range of temperature from 500 °C to 1000 °C. Meanwhile, the additional thermal treatment of the tablet, pressed from the powders heat-treated at the temperature of 1000 °C, at 1250 °C does not cause a significant mass change, suggesting that a possible excess of lithium ions is removed from the synthesized oxide system after repeated long-term heating, when the formation of the final multicomponent oxide with the composition of $Li_{0.35}La_{0.55}TiO_3$ was identified.

The right choice of the initial stoichiometry for the final $Li_{0.35}La_{0.55}TiO_3$ ceramic was partly confirmed by XRD results of $Li_{3x}La_{2/3-x}TiO_3$ (x=0.10, 0.12, 0.14 and 0.16) samples heat-treated at 1000 °C. The corresponding XRD patterns and the percentage distribution of crystalline phases are shown in Fig. 34. The red colour in the circle represents $Li_{0.35}La_{0.55}TiO_3$, while $Li_{0.3}La_{0.567}TiO_3$ is represented by the green colour.
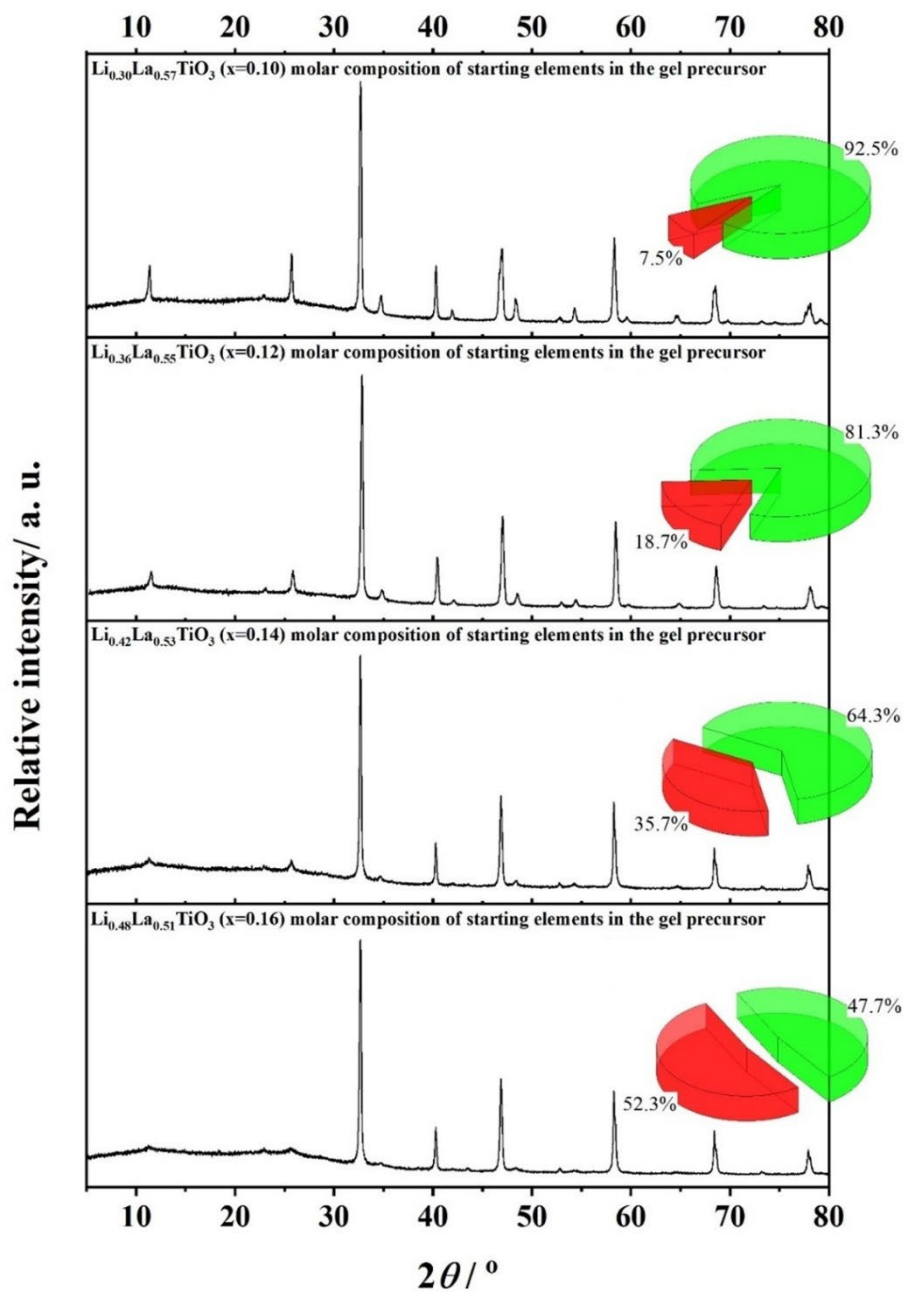
Fig. 34 XRD results of Li–La–Ti–O tartrate gel precursor samples for the ceramic of initial composition of $Li_{3x}La_{2/3-x}TiO_3$ (x=0.10, 0.12, 0.14 and 0.16) heat-treated at 1000 ºC

As seen from the Rietveld refinement results, the domination of the tetragonal crystal phase for $Li_{0.3}La_{0.567}TiO_3$ ceramic was identified, however, the tendency of the increase of the amount of orthorhombic crystal phase for $Li_{0.35}La_{0.55}TiO_3$ compound was also observed. This suggests that the initial molar ratio of lithium and lanthanum is an important factor that determines the formation of the crystalline composition of corresponding lithium lanthanum titanate at elevated temperatures. The lack of the crystalline side phases in the final ceramic mixture also creates additional advantages for the use of this synthesis technique in the preparation of lithium lanthanum titanates.

3.2.3. Structural analysis of the LLTO crystalline phases

As it was known from the XRD patterns, the initial molar ratio of Li/La atoms plays an important role in the formation of the final crystalline phase. The general information about the crystal structure of corresponding compounds could be successfully obtained from the values of the tolerance factor (t). This parameter shows the concept for the arrangement of interpenetrating dodecahedra and octahedra in a ABO_3 perovskite structure introduced by Goldschmidt [139], which is given by,

$$t = \frac{R_a + R_o}{(2)^{1/2} (R_b + R_o)} \qquad (13)$$

where R_a, R_b, and R_o are the ionic radii of cation A, B, and oxygen, respectively. For a complex perovskite system, R_a and R_b are the ionic radii of composed ions normalized by the atomic ratio [140]. The corresponding data of t values are presented in Table 5.

Table 5 The values of tolerance factor (t) for different initial compositions in the $Li_{3x}La_{2/3-x}TiO_3$ system

Initial composition	x value in the $Li_{3x}La_{2/3-x}TiO_3$ system	Tolerance factor
$Li_{0.3}La_{0.567}TiO_3$	0.0997	0.846
$Li_{0.3}La_{0.57}TiO_3$	0.100	0.848
$Li_{0.35}La_{0.55}TiO_3$	0.117	0.851
$Li_{0.36}La_{0.55}TiO_3$	0.120	0.854
$Li_{0.52}La_{0.53}TiO_3$	0.140	0.861
$Li_{0.48}La_{0.51}TiO_3$	0.160	0.867

In general, the perovskite structure is stable in the region $0.880 < t < 1.090$ and the symmetry is higher as the t value is close to 1. The t value also provides an indication about how far the atoms can move from the ideal packing positions and be still "tolerated" in the perovskite structure. It reflects the structural modification such as distortion, rotation, tilt of the octahedral [141, 142].

Similar conclusions were made from the stretching, angular, and torsional distortions of octahedra in the ABO_3 perovskite structure for $Li_{0.3}La_{0.567}TiO_3$ and $Li_{0.35}La_{0.55}TiO_3$ ceramics. ζ and Σ are general deviations of the metal ion complex from an ideal octahedral structure, whilst Θ represents a distortion from a perfect octahedral (O_h) to a trigonal prismatic (D_{3h}) geometry [143]. The mathematical expressions of ζ, Σ, and Θ parameters are given by the following equations:

$$\zeta = \sum_{i=1}^{6} |d_i - d_{mean}| \qquad (14)$$

$$\Delta = \frac{1}{6} \sum_{i=1}^{6} \left(\frac{d_i - d}{d}\right)^2 \qquad (15)$$

$$\Sigma = \sum_{i=1}^{12} |\phi_i - 90| \qquad (16)$$

$$\Theta = \sum_{i=1}^{24} |\theta_i - 60| \qquad (17)$$

The value of Δ for the stretching distortion parameter has the same meaning as ζ but does not depend on the units of measurement of the chemical bond length. The structural data for ζ, Δ, Σ and Θ parameters are shown in Tables 6 – 9, respectively.

Table 6 The distortion parameters for the octahedron in tetragonal and orthorhombic crystal structures for $Li_{0.3}La_{0.567}TiO_3$ and $Li_{0.35}La_{0.55}TiO_3$ ceramic

Initial composition	Crystal structure	Distortion parameters		
$Li_{0.35}La_{0.55}TiO_3$	Tetragonal for $Li_{0.3}La_{0.567}TiO_3$ composition	stretching distortion	ζ	85.167 pm
			Δ	$1.345\cdot10^{-4}$
		angular distortion	Σ	36.084º
		torsional distortion	Θ	29.636º
	Orthorhombic for $Li_{0.35}La_{0.55}TiO_3$ composition	stretching distortion	ζ	76.682 pm
			Δ	$4.935\cdot10^{-5}$
		angular distortion	Σ	18.237º
		torsional distortion	Θ	22.390º

Table 7 Data for the calculations of stretching distortion

Initial composition	Crystal structure	The bond lengths of Ti – O in the octahedral TiO_6 unit (d_i) / pm	$|d_i - d_{mean}|$ / pm
$Li_{0.35}La_{0.55}TiO_3$	Tetragonal for $Li_{0.3}La_{0.567}TiO_3$ composition	1945.4	1.917
		1945.4	1.917
		1945.4	1.917
		1945.4	1.917
		1978.4	34.917
		1900.9	42.583
	Orthorhombic for $Li_{0.35}La_{0.55}TiO_3$ composition	1951.29	5.605
		1934.65	11.037
		1934.65	11.037
		1957.29	11.603
		1929.42	16.267
		1966.82	21.134

Table 8 Data for the calculations of angular distortion

Initial composition	Crystal structure	The valence angle of <O – Ti – O in the octahedral TiO_6 unit (ϕ_i) / º	$|\phi_i - 90|$ / º
$Li_{0.35}La_{0.55}TiO_3$	Tetragonal for $Li_{0.3}La_{0.567}TiO_3$ composition	85.654	4.346
		85.654	4.346
		85.654	4.346
		85.654	4.346
		89.671	0.329
		89.671	0.329
		89.671	0.329
		89.671	0.329
		94.346	4.346
		94.346	4.346
		94.346	4.346
		94.346	4.346
	Orthorhombic for $Li_{0.35}La_{0.55}TiO_3$ composition	85.429	4.571
		88.280	1.720
		88.280	1.720
		89.390	0.610
		89.390	0.610
		90.609	0.609
		90.508	0.508
		90.508	0.508
		91.069	1.069
		91.708	1.708
		91.708	1.708
		92.897	2.900

Table 9 Data for the calculations of torsional distortion

Initial composition	Crystal structure	The valence angle of <O – O – O in the octahedral TiO_6 unit (θ_i) / º	$|\theta_i - 60|$ / º
		58.185	1.815
		58.185	1.815
		58.185	1.815
		58.185	1.815
		59.055	0.945
		59.055	0.945
		59.055	0.945
		59.055	0.945
		59.056	0.944

Initial composition	Crystal structure	The valence angle of <O – O – O in the octahedral TiO_6 unit (θ_i) / °	$|\theta_i - 60| / °$
$Li_{0.35}La_{0.55}TiO_3$	Tetragonal for $Li_{0.3}La_{0.567}TiO_3$ composition	59.056	0.944
		59.056	0.944
		59.056	0.944
		60.908	0.908
		60.908	0.908
		60.908	0.908
		60.908	0.908
		60.908	0.908
		60.908	0.908
		60.908	0.908
		60.908	0.908
		61.889	1.889
		61.889	1.889
		61.889	1.889
		61.889	1.889
	Orthorhombic for $Li_{0.35}La_{0.55}TiO_3$ composition	58.256	1.744
		58.256	1.744
		58.367	1.633
		58.367	1.633
		58.781	1.219
		58.781	1.219
		59.203	0.797
		59.203	0.797
		59.858	0.142
		59.858	0.142
		59.937	0.063
		59.937	0.063
		60.103	0.103
		60.103	0.103
		60.145	0.146
		60.145	0.146
		60.938	0.938
		60.938	0.938
		61.074	1.074
		61.074	1.074
		61.530	1.530
		61.530	1.530
		61.807	1.807
		61.807	1.807

The representations of crystal lattices with octahedral distortions for $La_{2/3-x}Li_{3x}TiO_3$ ceramics presented in Figs. 35 [144] and 36 [138].
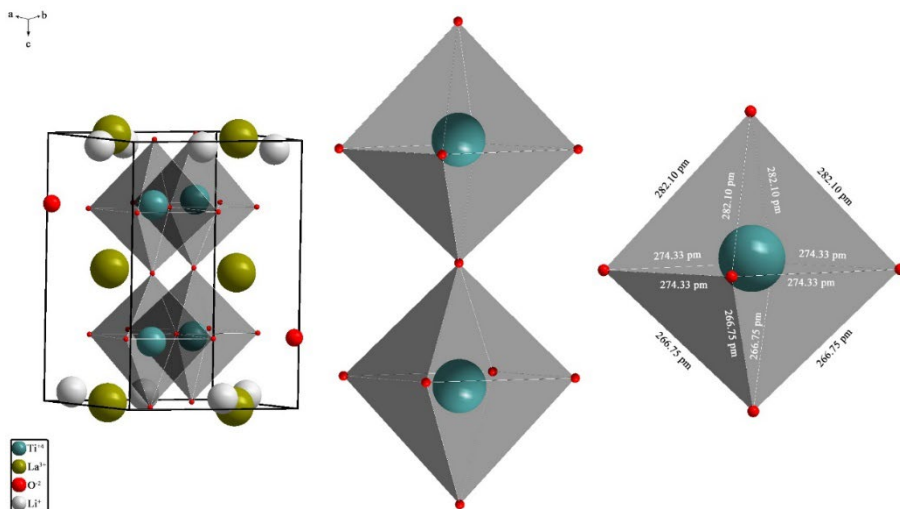

Fig. 35 The tetragonal crystal structure for $Li_{0.3}La_{0.567}TiO_3$ phase with internal octahedral TiO_6 units [144]
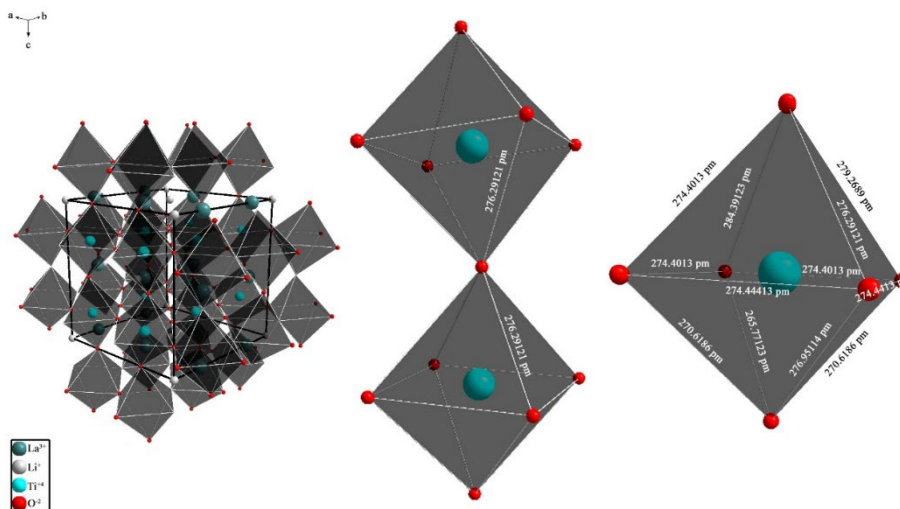
Fig. 36 The orthorhombic crystal structure for $Li_{0.35}La_{0.55}TiO_3$ phase with the octahedral surrounding of TiO_6 units [138]

The values of distortion parameters determined for $Li_{0.35}La_{0.55}TiO_3$, were higher for the tetragonal crystal phase compared with the orthorhombic structure. The values of tolerance factor (t) for different initial compositions in the $La_{2/3-x}Li_{3x}TiO_3$ system were determined to be in the range of 0.846 – 0.867, which approximately corresponds to the theoretical values of the stable perovskite structure.

3.2.4. The crystalization of the $Bi_{23}V_4O_{44}$ compound from the mixture of $5Bi_2O_3 \cdot V_2O_5$

In order to confirm the crystalline composition in the heat-treated Bi–V–O gel precursors for $5B_2O_3 \cdot V_2O_5$ ceramic the XRD was performed. The XRD data of both Bi–V–O tartrate gel precursors (Fig. 37 (a) and (b)) heat-treated at the temperature of 870 °C correspond to the characteristic reflections, which are attributed to the orthorhombic crystal structure of the $Bi_{23}V_4O_{44}$ system [145].

The Rietveld refinement analysis of the corresponding samples confirmed the domination of the orthorhombic $Bi_{23}V_4O_{44}$ (ICSD No.: 418368) crystalline compound. The trace phases of monoclinic $Bi_{46}V_8O_{89}$ (ICSD No.: 415113) and triclinic $Bi_{46}V_8O_{89}$ (ICSD No.: 87271) systems were also identified. According to this result, the initial composition of $5B_2O_3 \cdot V_2O_5$ well matches the obtained crystalline phases.

The domination of the orthorhombic phase was observed for the gel precursors prepared during Synthesis 1 and heat-treated at the temperature of 800 °C (Fig. 37 (c)). Such a result is closely related to the homogeneity of as-prepared Bi–V–O tartrate gel precursor, which was confirmed by the amorphous character of the XRD pattern as shown in Fig. 37 (d).
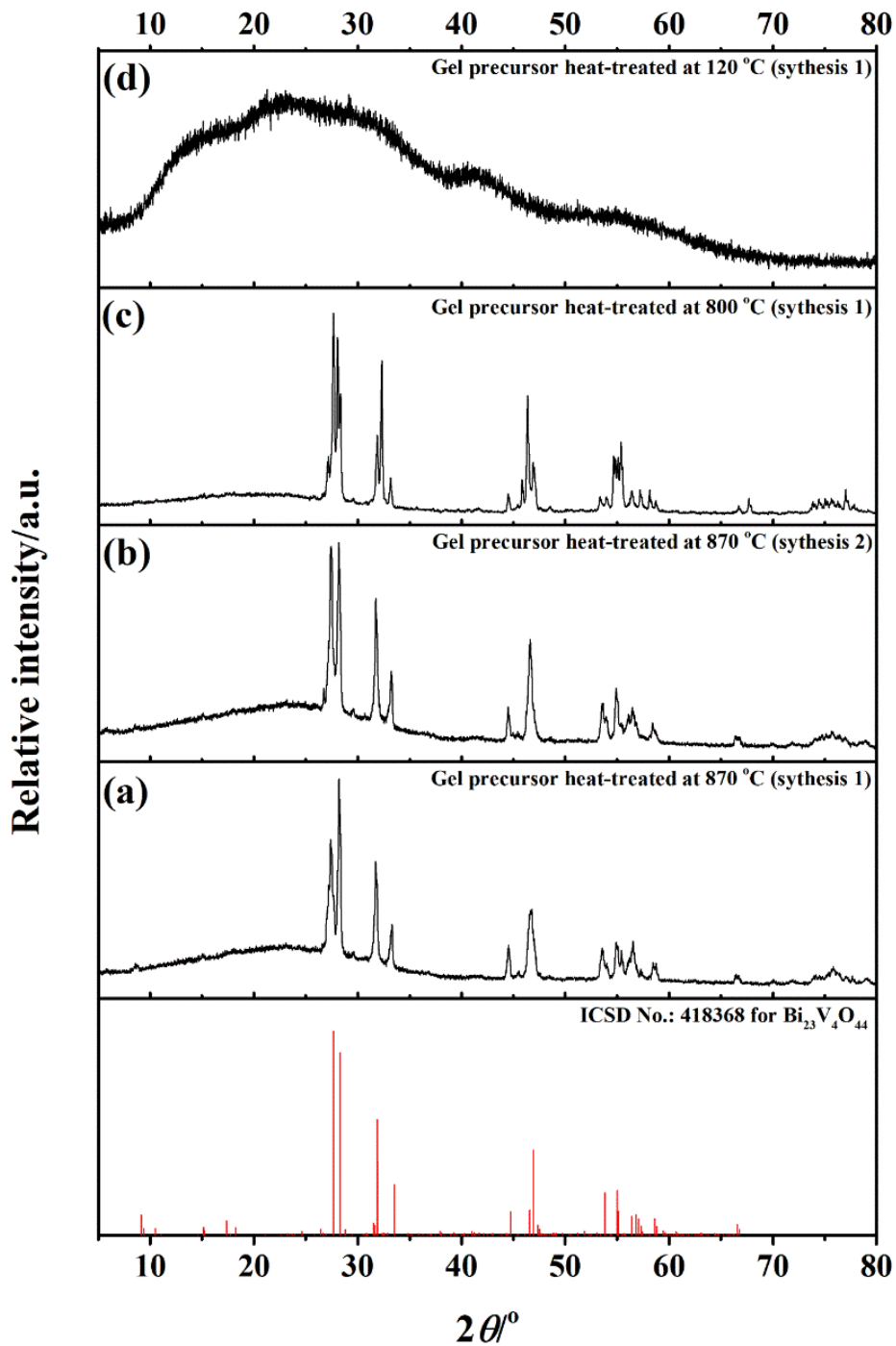
Fig. 37 Standard ICSD card for $Bi_{23}V_4O_{44}$ and XRD patterns of the Bi–V–O gel precursors heat-treated at different temperatures

3.3. Investigation of surface microstructure by scanning electron microscopy

The surface morphology of the metal tartrate gel precursors for the corresponding ceramic materials synthesized by the aqueous sol-gel method and heat-treated at different temperatures was studied using scanning electron microscopy (SEM). This analysis method is suitable for studying the morphology of the surface of the material because of its significantly higher resolution and image depth compared to an optical microscope.

3.3.1. Temperature effect on the surface morphology of Li–Al–Mo–O tartrate gel precursor

In order to show the tendency of particle growth of obtained ceramics by increasing the heat-treatment temperature, the surface morphology was investigated. Corresponding SEM micrographs of the Li–Al–Mo–O tartrate gel precursor heat-treated at 400 ºC, 500 ºC, 600 ºC, and 700 ºC are shown in Fig. 38. In the SEM picture of part (a) for Fig. 38, the surface of the sample is homogeneous, consisting of irregularly shaped formations formed during the decomposition of unreacted tartaric acid. This result is in a good agreement with the XRD data when the formation of the final ceramic at the temperature of 400 ºC is not clearly expressed. As seen from Fig. 38 micrograph (b), the increase of the heat-treatment temperature of the sample up to 500 ºC shows the changes in the surface morphology associated with the start of the growth of spherical particles with a size smaller than 200 nm. An almost identical view is observed for the gel precursor heat-treated at the temperature of 600 ºC, in which a well-seen agglomeration of smaller particles into large aggregates is distinguished. Finally, the heat-treatment of the sample at 700 ºC forms the particles of regular shape with well-defined edges, ranging in size from 4 μm to 10 μm.
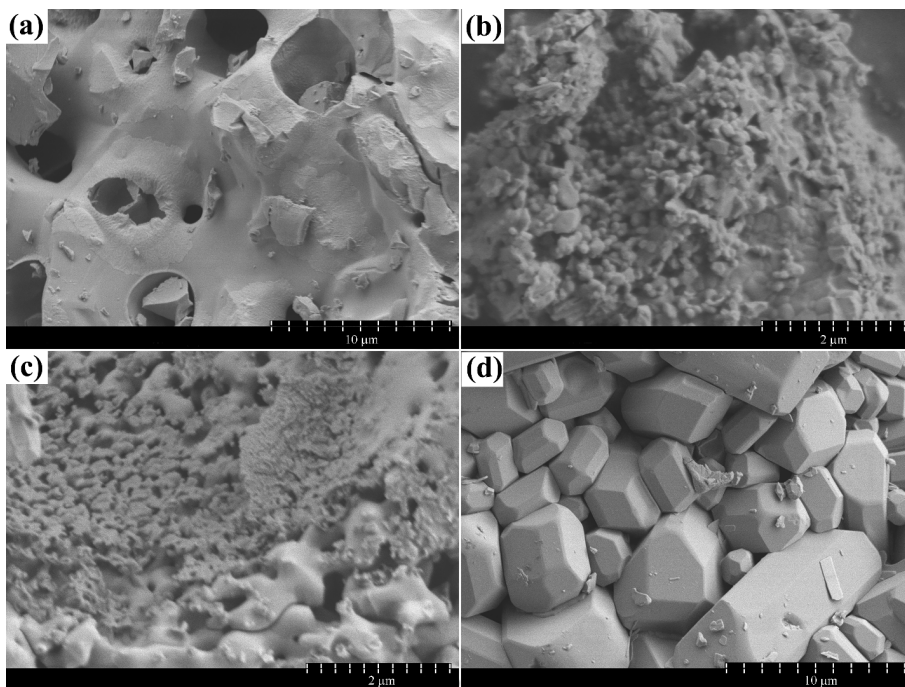
Fig. 38 SEM micrographs of Li–Al–Mo–O tartrate gel precursor for LiAlMo$_2$O$_8$ ceramic heat-treated at the temperatures of 400 ºC (a), 500 ºC (b), 600 ºC and 700 ºC (d) in the air atmosphere

Thus, SEM analysis indicate that the growth of the particles of the final ceramic takes place in two stages. In the first step, the formation of agglomerates of crystallites whose diameter does not exceed 100 nm is distinguished. Meanwhile, above the temperature of 600 ºC, the formed particles start to combine into formations of 4 µm - 10 µm in size with a regular structure, clear planes, and well-expressed edges. Based on the results of the XRD, it can be concluded that the regularly shaped particles are mainly composed of crystallites, which average size corresponds to the value of 126.11 nm.

3.3.2. Formation of dense structure in LLTO ceramic

The primary absence of correlation between SEM results and XRD data suggests that the obtained particles on the tablet surface are composed of closely packed crystallites. Despite the even shape of the particles and clearly defined edges, the wide size distribution suggests that the parameters of the

crystallites are less than the corresponding particles on the tablet surface, and it fits well with the XRD results. From Fig. 39, it can be summarized that the surface morphology of the synthesized $Li_{0.35}La_{0.55}TiO_3$ crystalline compound, which was heat-treated at the temperature of 1250 °C for 5 hours in the air atmosphere, consists of regular shape particles, which size varies from 1 μm to 10 μm.
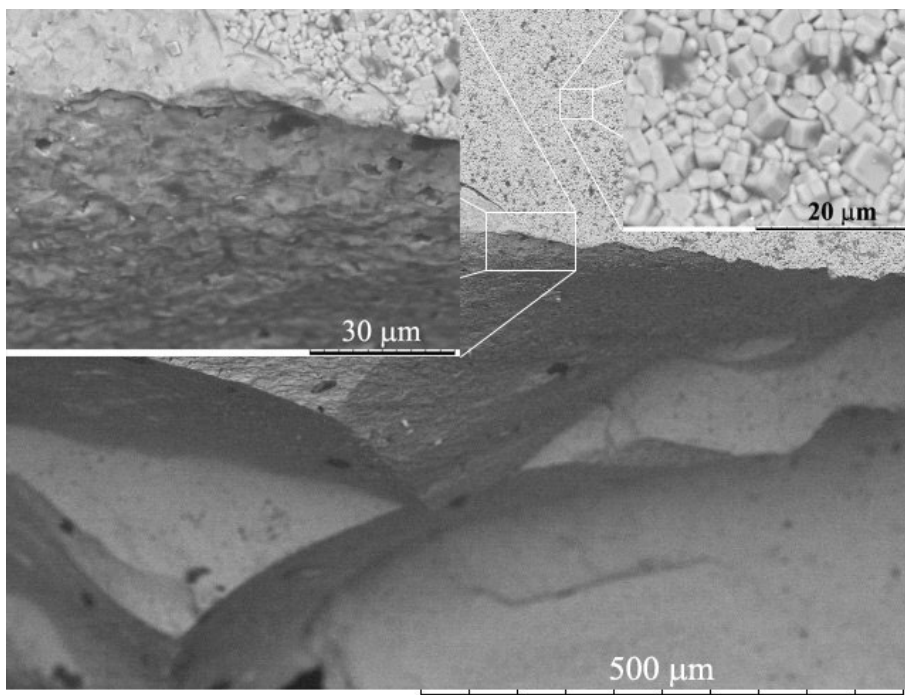
Fig. 39 SEM micrographs of Li–La–Ti–O tartrate gel precursor for $Li_{0.35}La_{0.55}TiO_3$ ceramic heat-treated at the temperature of 1250 °C in the air atmosphere

It should be mentioned that inside the tablet, at the fracture site, the dense packing of the synthesized crystallites in the monolithic surface without well-seen cracks and cavities was identified.

Knowing the fact that the close-packed crystallites and the dense structure of the single-crystalline multicomponent oxide significantly enhance the conductivity properties of the obtained sample, the size of the separate particles could influence the decreased conductivity of grain boundary values, especially at low temperatures, when the mobility of lithium ions is relatively low.

3.3.3. SEM micrographs and EDS analysis for $5Bi_2O_3 \cdot V_2O_5$ ceramic

The surface morphological features, which play an important role in the electrical properties of synthesized ceramic, were also investigated by scanning electron microscopy (SEM). The corresponding SEM micrographs of the Bi–V–O tartrate gel precursors heat-treated at 870 °C of temperature are presented in Fig. 40, respectively.
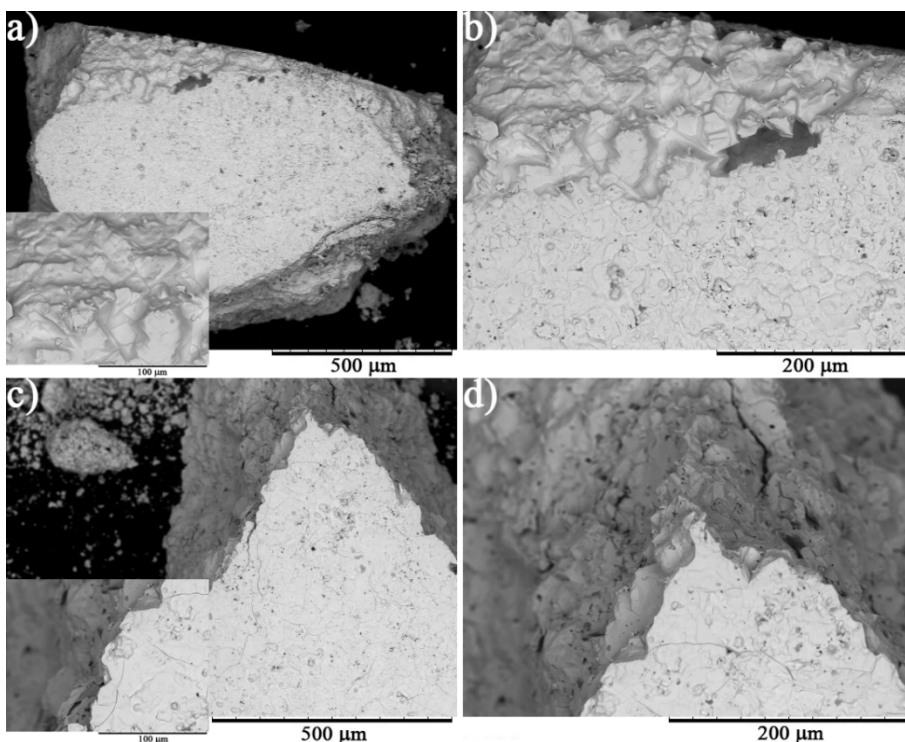
Fig. 40 SEM micrographs of Bi–V–O tartrate gel precursors for $5Bi_2O_3 \cdot V_2O_5$ ceramic, which was obtained applying synthesis 1 (a, b) and synthesis 2 (c, d), respectively

As is shown in Fig. 40 (a), the surface is dense with no cracks and cavities. At higher magnification of the SEM picture (Fig. 40 (b)), the particles are seen to be connected with the partially melted substance, which increases the hardness and mechanical strength of the ceramic. A slightly different view of SEM pictures of the $5Bi_2O_3 \cdot V_2O_5$ ceramic (synthesis 2) presented in Fig. 40 (c and d), where the surface mainly consists of the massive monoliths with

both the sharp edges and small cavities, which diameter varies from 500 nm to 3 μm.

In addition to the morphological peculiarities of both samples, it should be also noted that the mechanical treatment, which was applied to insert it into the probe for impedance analysis, was cardinally different. The mechanical treatment of $5Bi_2O_3 \cdot V_2O_5$ ceramic, prepared using synthesis 1, was easily handled, which resulted in the desired form and dimensions with a smooth surface of the sample. However, the abrasion of the other sample was much more complicated because of formation of cracks and easy crumbling.

The reason for such differences in mechanical abrasion was partly proven by analysing the elemental composition of the synthesized ceramics. Table 10 shows the amounts of the elements, which were estimated employing Energy-dispersive X-ray spectroscopy (EDS).

Table 10 The content of bismuth, vanadium and oxygen in the ceramic that was heat-treated at different temperatures

Sample	Heat-treatment temperature/ºC	Bismuth content in mol	Vanadium content in mol	Oxygen content in mol
$5Bi_2O_3 \cdot V_2O_5$ (synthesis 1)	120	27.410	2	174.170
	800	17.799	2	44.416
	870	10.996	2	30.970
$5Bi_2O_3 \cdot V_2O_5$ (synthesis 2)	120	16.992	2	97.700
	800	14.844	2	47.394
	870	17.717	2	56.577

The obtained results revealed that a smaller amount of tartaric acid during the sol-gel process (synthesis 1) determines the molar ratio of bismuth (10.996) and vanadium (2.000) close to both the initial amount of elements ($5Bi_2O_3 \cdot V_2O_5$), and the crystalline compound for $Bi_{23}V_4O_{44}$ composition, which was assigned from XRD data. The increased amount of oxygen atoms in the sample could be explained by both the organic-based impurities especially at low temperatures and the nonstoichiometry in either the crystal oxides or amorphous phases for the sample heat-treated at the temperature of 870 ºC.

The molar ratio of bismuth and vanadium for synthesis 2 remained similar regardless of heat-treatment temperature. Besides, such result is in a good agreement with the conclusion made from the thermal analysis about the

influence of the increased amount of tartaric acid on the composition of ceramic.

3.4. FT-IR analysis of LiLaMo$_2$O$_8$ ceramic

Infrared spectroscopy (IR) for the Li–Al–Mo–O tartrate gel precursor heat-treated at different temperatures was performed (Fig. 41) as an important investigation technique, which enables the fixation of the vibrational frequency of bonds for the crystalline ceramic with the initial composition of LiAlMo$_2$O$_8$.
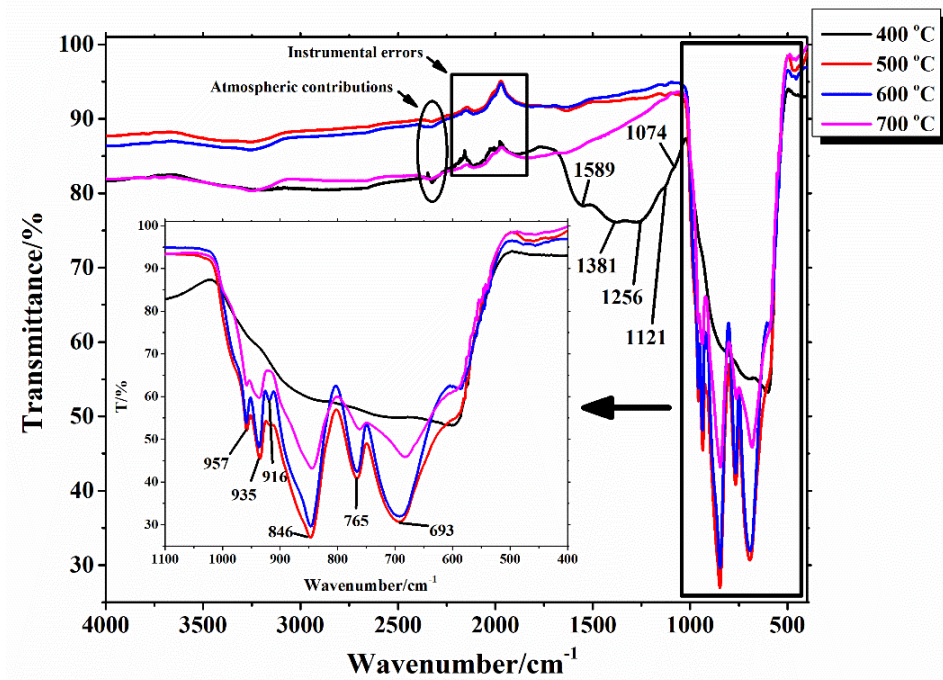
Fig. 41 FT–IR transmittance spectra of the Li–Al–Mo–O tartrate gel precursors for LiAlMo$_2$O$_8$ ceramic heat-treated at 400 °C, 500 °C, 600 °C, and 700 °C of temperature

Generally, the infrared bands for inorganic materials are broader, fewer in number, and appear at lower wavenumbers than those observed for organic materials [146]. Nevertheless, in the FT-IR spectrum of the sample heat-treated at 400 °C, a broad band with weakly expressed peaks in the range from 1600 cm^{-1} to 1050 cm^{-1} is attributable to the characteristic vibrations for

chemical bonds of corresponding tartrates. In this case, the peak at 1589 cm^{-1} corresponds to the asymmetric stretching of the –COO functional group. Meanwhile, the peak position at 1380 cm^{-1} describes either –OH in-plane bending or –COO symmetric stretching. In summary, the –COO asymmetric and symmetric stretching vibrations combined with –OH in-plane bending vibrations are observed at ~1589 cm^{-1} and ~1380 cm^{-1}, respectively [147]. The peaks that correspond to the values of 1256 cm^{-1}, 1121 cm^{-1}, and 1074 cm^{-1} are attributed to C–H in-plane stretching [148], C–OH and CH–OH stretching [149]. The relatively low intensity of the characteristic peaks attributable to the organic compounds can be explained by the complete decomposition of tartaric acid and the evaporation of the as-formed volatile components, and the existence of partially decomposed metal tartrates.

When increasing the heat-treatment temperature, the peaks of the organic compounds in the range from 1600 cm^{-1} to 1050 cm^{-1} tend to disappear. Meanwhile, the newly formed characteristic peaks, identified in the wavenumber range from 1000 cm^{-1} to 500 cm^{-1}, correspond to the vibrations of the metal-oxygen bond. In this case, the peaks attributable to ~957 cm^{-1} and ~935 cm^{-1} wavenumber correspond to characteristic vibrations of the symmetric MoO$_4$ tetrahedron. Meanwhile, a triply degenerate mode (v_3) of F$_2$ symmetry for v_{as}(MoO$_4$) and v(Mo$_2$O$_2$) bridge vibrations correspond to the peaks at ~916 cm^{-1}, ~846 cm^{-1}, ~765 cm^{-1} and ~693 cm^{-1}, respectively [150-152].

The intensity, width, and shape of the peaks in the range from 1000 cm^{-1} to 500 cm^{-1} depend on several factors such as the degree of crystallinity, surface area and crystal structure of the ceramic precursor. By increasing the heat-treating temperature, the crystallinity of the crystalline compounds also increases. Meanwhile, the opposite effect is observed when the crystallites and particles tend to grow and the surface area has a tendency to decrease [137]. This is the main reason that determines the decrease in the intensity of the characteristic peaks of the gel precursor heat-treated at 700 °C.

3.5. Electrical conductivity properties of LLTO ceramic

The ionic conductivity of the lithium ions in the Li–La–Ti–O system depends significally on the crystalline structure of the three-component oxide compound. The mechanism of bulk conductivity for the tetragonal Li$_{3x}$La$_{1.33-x}$Ti$_2$O$_6$ system (P4/mmm) was proposed by Ruiz et al. [153], which fits a parabolic function of x with a maximum value for Li$^+$, content equal to 0.25, as suggested by Inaguma et al. [154], who described the Li$_{3x}\square_{(1/3)-2x}$

La$_{(2/3)-x}$TiO$_3$ stoichiometry for these oxides. Inaguma et al. also proposed the ionic mechanism for the Li-rich Li$_{3x}$La$_{2/3-x}$TiO$_3$, furnace-cooled Li$_{0.35}$La$_{0.55}$TiO$_3$ system. It is expected that the tilt of TiO$_6$ octahedra and the La ordering attribute to faster lithium-ion conduction in La-poor layer than in La-rich layer, and control percolative diffusion pathway, from two-dimensionally to quasi-three-dimensionally [138]. With the increase of the heat treatment temperature, the volatility of lithium ions also changes. This affects both the ratio of Li/La ions and the composition of crystal phases in the oxide mixture. Under these circumstances, the dominance of the crystalline phase of lithium lanthanum titanate also tends to change. Depending on the number of elements in such multisystem, the continuous recrystallization occurs at relatively high temperatures, and as a result, the size of the crystallites does not increase significantly and sometimes even tends to decrease, and usually does not exceed of 110 nm. This is the main reason why in such a multicomponent oxide system the increased intergranular resistance is relatively high and it possesses the reduction of the total ionic conductivity, especially at low temperature.

To confirm these statements and by using the information provided in the previous sections, the obtained ionic conductivity values of Li$_{0.35}$La$_{0.55}$TiO$_3$ ceramic were also evaluated in this work. The corresponding results of the impedance spectroscopy are placed in Figs. 42, 43, 44 and 45, respectively.
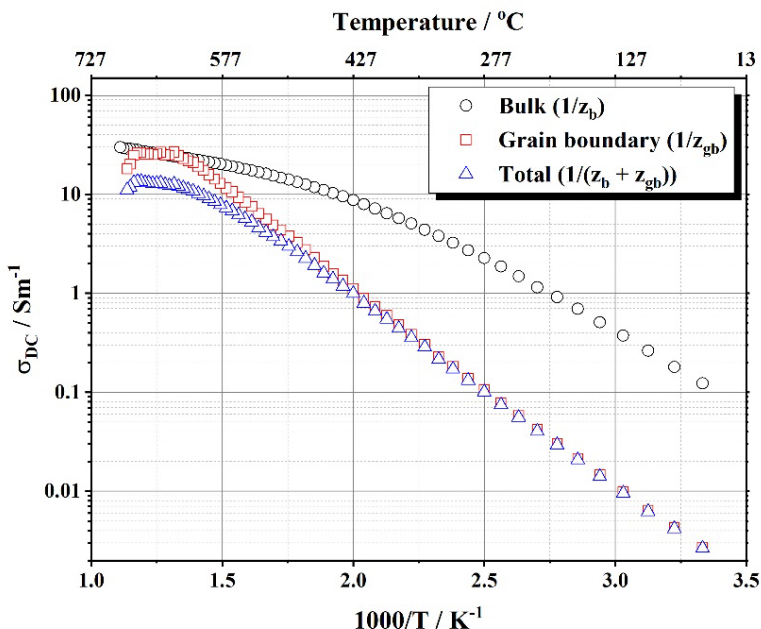
Fig. 42 Arrhenius plots of the ionic conductivity for Li$_{0.35}$La$_{0.55}$TiO$_3$ ceramic
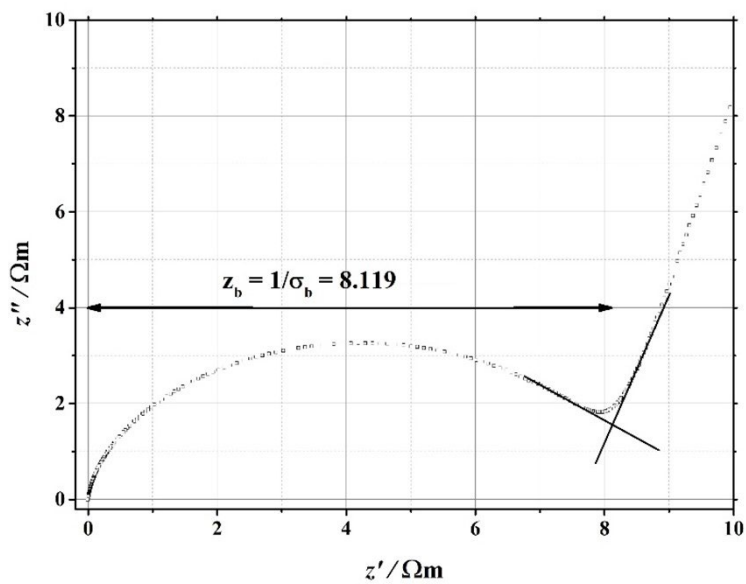
Fig. 43 Complex impedance plot of the bulk part for lithium lanthanum titanate at 27 °C
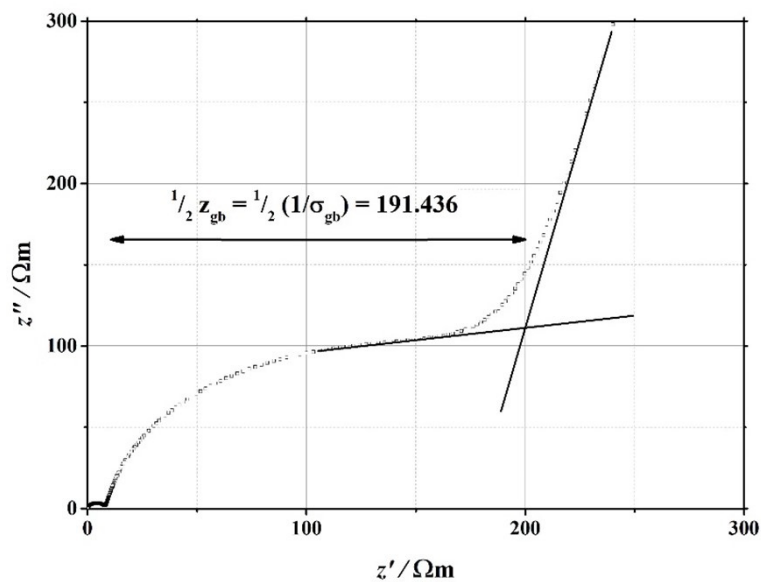
Fig. 44 Complex impedance plot of the grain boundary part for lithium lanthanum titanate at 27 °C
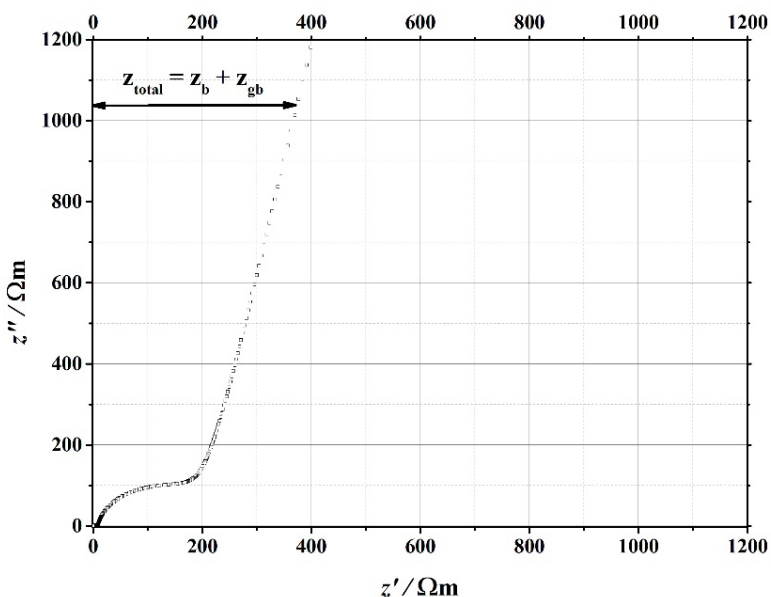
Fig. 45 Complex impedance plot of the total conductivity for lithium
lanthanum titanate at 27 °C

For comparison with other works, the ionic conductivity values for the
$La_{2/3-x}Li_{3x}TiO_3$ system are placed in Table 11 [154-158].

Table 11 The ionic conductivity at 27 °C for lanthanum lithium titanates

Starting composition	Ionic conductivity of bulk part at 27 °C / S·m^{-1}	Ref.
$Li_{0.35}La_{0.55}TiO_3$	0.10	[154]
$Li_{0.35}La_{0.55}TiO_3$	0.080	[155]
$Li_{0.5}La_{0.5}TiO_3$	0.141	[156]
$Li_{0.31}La_{0.41}TiO_3$ (thin film)	0.00525	[157]
$Li_{0.35}La_{0.55}TiO_3$ (nanofiber)	0.053	[158]

Meanwhile, the grain boundary resistance is relatively high, which results
in a significant decrease in the total ionic conductivity of the resulting Li–La–
Ti–O system. This result confirms the assumption that the formation of
crystallites, which sizes remain in the nanometric scale, leads to the relatively
low total conductivity at 27 °C. The grain boundary conductivity increases
linearly by increasing the temperature, however, the dependence of bulk

conductivity versus temperature is exponential. This is due to the different conductivity of lithium ions within the crystallites and in the grain boundary. It seems that the large area of the intergranular space distorts the temperature dependence of the grain boundary conductivity values and creates favorable conditions for its dominance. This effect is largely determined by the size of the crystallites in the Li–La–Ti–O system. From such results, it is likely that the larger crystallites would increase the total conductivity of Li–La–Ti–O system even without changing the element ratio during the synthesis procedure. In addition, the decrease of the conductivity of grain boundary at elevated temperature is directly related to both partial phase transition from orthorhombic to tetragonal phase, and the distortion of chemical bonds in the corresponding crystal structure.

3.6. Electrical conductivity properties of $5Bi_2O_3 \cdot V_2O_5$ system

Thermal decomposition of the Bi–V–O tartrate gel precursors and detailed characterization of the $5Bi_2O_3 \cdot V_2O_5$ materials revealed that the amount of the tartaric acid plays a crucial role to both the final composition of obtained ceramic, and the features of the surface morphology. Taking into account that only for $5Bi_2O_3 \cdot V_2O_5$ (synthesis 1) sample it was possible to form a pellet with stable dimensions, the measurements of the conductivity were undertaken only for this sample. The corresponding temperature dependence of the conductivity was evidenced from Arrhenius plots σ v/s $f(10^3/T)$. The representation of the first cooling (350 ºC – 110 ºC) and the second heating (110 ºC – 350 ºC) stages overlaps, and only the second heating data are represented for clarity in Fig. 46.
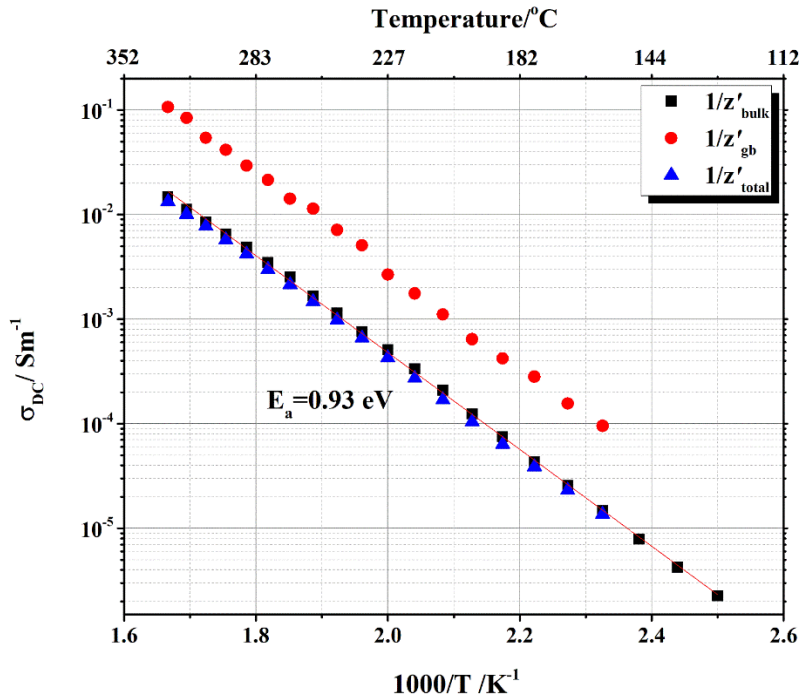
Fig. 46 Arrhenius plot of temperature dependencies of standard deviation for $5Bi_2O_3 \cdot V_2O_5$ ceramic (synthesis 1)

The $5Bi_2O_3 \cdot V_2O_5$ ceramic displays an Arrhenius type of electrical conduction behaviour, i.e. a linear dependence versus temperature in the whole investigated range for both the bulk, and the grain boundary. From the value of slope recalculated activation energy (E_a) is equal to 0.93 eV for all sorts of conductivities.

It is also interesting to note that obtained values of the total conductivity (σ_{total}) at the temperature of 330 ℃ are similar comparing with systems for $Pb_{10}Bi_{36}V_8O_{84}$, $Sr_{10}Bi_{36}V_8O_{84}$, $Ca_{10}Bi_{36}V_8O_{84}$, $Cd_{10}Bi_{36}V_8O_{84}$, and $Bi_4V_2O_{11-\delta}$ ceramics even at 800 ℃ [145, 159, 160]. Thus, the chosen synthesis technique probably determines the uniqueness of the obtained ceramics from both structural and compositional points.

CONCLUSIONS

1. The aqueous sol-gel synthesis method is suitable for obtaining single-phase crystalline phases of composition for $LiAlMo_2O_8$, $Li_{0.35}La_{0.55}TiO_3$, and $5Bi_2O_3 \cdot V_2O_5$ with a small fraction of additional phases.

2. The obtained homogeneous Li–Al–Mo–O, Li–La–Ti–O, and Bi–V–O tartrate gels are composed of a mixture of tartaric acid and metal tartrates.

3. The decomposition process of tartaric acid takes place in the temperature range of 30 ºC – 320 ºC, the mechanism of which is described in detail and confirmed by the specific characteristics of the mass change and thermal transformations of TGA and DSC.

4. The formation of crystalline phases is most influenced by the heating temperature in the case of Li-Al-Mo-O, and the molar ratio of individual elements in the final gel precursor in the case of Li-La-Ti-O.

5. The morphology of the surface of the obtained ceramics and the formation of pores or cracks are most influenced by the temperature and the method of preparing the ceramics for heating.

REFERENCES

1. S. Sorokina, R. Enjalbert, P. Baules, A. Castro, J. Galy. Structural Study of Modified $Bi_4V_2O_{10+ \delta}$ Phases (δ= 0, 0.5, 1): Influence of Antimony Contribution. *Journal of Solid State Chemistry* **1999**, 144 (2), 379-387. https://doi.org/10.1006/jssc.1999.8169

2. D. Qian, B. Xu, H. M. Cho, T. Hatsukade, K. J. Carroll, Y. S. Meng. Lithium lanthanum titanium oxides: a fast ionic conductive coating for lithium-ion battery cathodes. *Chemistry of Materials* **2012**, 24 (14), 2744-2751. https://doi.org/10.1021/cm300929r

3. A. G. Belous, O. I. V'yunov, L. L. Kovalenko, O. Bohnke, C. Bohnke. Synthesis of thin-film electrodes based on LiPON and LiPON-LLTO-LiPON. *Russian Journal of Electrochemistry* **2014**, 50, 523-530. https://doi.org/10.1134/S1023193514060020

4. D. S. Khaerudini, G. Guan, P. Zhang, X. Hao, A. Abudula. Prospects of oxide ionic conductivity bismuth vanadate-based solid electrolytes. *Reviews in Chemical Engineering* **2014**, 30 (6), 539-551. https://doi.org/10.1515/revce-2014-0020

5. J. Wang, L. Luo, B. Huang, J. He, W. Zhang, W. Zhao, J. Wang. The preparation and optical properties of novel $LiLa(MoO_4)_2$:Sm^{3+}, Eu^{3+} red phosphor. *Materials* **2018**, 11 (2), 297. https://doi.org/10.3390/ma11020297

6. C. Bohnke, H. Duroy, J. L. Fourquet. pH sensors with lithium lanthanum titanate sensitive material: applications in food industry. *Sensors and Actuators B: Chemical* **2003**, 89 (3), 240-247. https://doi.org/10.1016/S0925-4005(02)00473-2

7. S. Lorant, O. Bohnke, J. Brévière, C. Bohnke. All-Solid-State pH Sensor Used in Oil Drilling Mud. *Electroanalysis* **2013**, 25 (1), 223-229. https://doi.org/10.1002/elan.201200367

8. J. Luo, P. Fu, Y. Qu, Z. Lin, W. Zeng. The n-butanol gas-sensing properties of monoclinic scheelite $BiVO_4$ nanoplates. *Physica E: Low-dimensional Systems and Nanostructures* **2018**, 103, 71-75. https://doi.org/10.1016/j.physe.2018.05.030

9. J. H. Kim, J. S. Lee. Elaborately modified $BiVO_4$ photoanodes for solar water splitting. *Advanced Materials* **2019**, 31 (20), 1806938. https://doi.org/10.1002/adma.201806938

10. Y. Heng, W. Wang, Q. Li, X. Li, M. Dai, C. Yu, Z. Xue, J. Xia, G. Zhou, D. Jiang. All-solid-state reference electrode based on a solid-state electrolyte of high densified Lithium lanthanum titanium oxide (LLTO). *Journal of Electroceramics* **2021**, 47 (1), 23-30. https://doi.org/10.1007/s10832-021-00262-7

11. H. E. A. Mohamed, S. Afridi, A. T. Khalil, T. Zohra, M. M. Alam, A. Ikram, Z. K. Shinwari, M. Maaza. Phytosynthesis of $BiVO_4$ nanorods using Hyphaene thebaica for diverse biomedical applications. *AMB Express* **2019**, 9, 1-14. https://doi.org/10.1186/s13568-019-0923-1

12.Y. Zhang, L. Wang, Z. Guo, Y. Xu, Y. Wang, H. Peng. High-performance lithium–air battery with a coaxial-fiber architecture. *Angewandte Chemie International Edition* **2016**, 55 (14), 4487-4491.

13.W. Zhang. Crisis PR study on Samsung Galaxy Note 7 explosion incident. *International Journal of Business and Management* **2020**, 15 (7), 68-76. https://doi.org/10.5539/ijbm.v15n7p68

14.M. Itoh, Y. Inaguma, W. H. Jung, L. Y. Chen, T. Nakamura. High lithium ion conductivity in the perovskite-type compounds $Ln_{12}Li_{12}TiO_3$ (Ln= La, Pr, Nd, Sm). *Solid State Ionics* **1994**, 70, 203-207. https://doi.org/10.1016/0167-2738(94)90310-7

15.R. G. Hendrickson, A. Chang, R. J. Hamilton. Co-worker fatalities from hydrogen sulfide. *American journal of industrial medicine* **2004**, 45 (4), 346-350. https://doi.org/10.1002/ajim.10355

16.G. R. Milner, J. L. Boldsen. Population trends and the transition to agriculture: Global processes as seen from North America. *Proceedings of the National Academy of Sciences* **2023**, 120 (4), e2209478119. https://doi.org/10.1073/pnas.2209478119

17.J. D. Lloyd, R. Butryn, S. Pearman-Gillman, T. D. Allison. Seasonal patterns of bird and bat collision fatalities at wind turbines. *Plos one* **2023**, 18 (5), e0284778. https://doi.org/10.1371/journal.pone.0284778

18.E. L. Welsh. Solar Farms in Georgia: Why We Need To Start Thinking About the End. *Georgia State University Law Review* **2023**, 39 (4), 1131. https://readingroom.law.gsu.edu/gsulr/vol39/iss4/13

19.N. Obaid, A. A. N. A. S. Study on Phase Stability of Mn (IV) Doped Bismuth Vanadate and its Visible-Light Photocatalytic Activity for Degradation of Organic Dye.

20.J. H. Kim, J. S. Lee. $BiVO_4$-based heterostructured photocatalysts for solar water splitting: a review. *Energy and Environment Focus* **2014**, 3 (4), 339-353. https://doi.org/10.1166/eef.2014.1121

21.W. Paraguassu, A. G. Souza Filho, M. Maczka, P. T. C. Freire, F. E. A. Melo, J. Mendes Filho, J. Hanuza. Raman scattering study of $NaAl (MoO_4)_2$ crystal under high pressures. *Journal of Physics: Condensed Matter* **2004**, 16 (28), 5151. https://doi.org/10.1088/0953-8984/16/28/033

22.Y. Hua, S. K. Hussain, J. S. Yu. Samarium (iii) and terbium (iii) ion-doped $NaLa(MoO_4)_2$ phosphors for versatile applications. *New Journal of Chemistry* **2019**, 43 (26), 10645-10657. https://doi.org/10.1039/C9NJ01751H

23.G. Wang, X. Han, M. Song, Z. Lin, G. Wang, X. Long. Growth and spectral properties of Cr^{3+}:$KAl(MoO_4)_2$ crystal. *Materials Letters* **2007**, 61 (18), 3886-3889. https://doi.org/10.1016/j.matlet.2006.12.080

24.M. Maczka, K. Hermanowicz, P. E. Tomaszewski, J. Hanuza. Lattice dynamics and phase transitions in $KAl(MoO_4)_2$, $RbAl(MoO_4)_2$ and $CsAl(MoO_4)_2$ layered crystals. *Journal of Physics: Condensed Matter* **2004**, 16 (20), 3319. https://doi.org/10.1088/0953-8984/16/20/003

25.K. Hermanowicz, M. Mączka, P. J. Dereń, J. Hanuza, W. Stręk, H. Drulis. Optical properties of chromium (III) in trigonal $KAl(MoO_4)_2$ and monoclinic

$NaAl(MoO_4)_2$ hosts. *Journal of luminescence* **2000**, 92 (1-2), 151-159. https://doi.org/10.1016/S0022-2313(00)00232-5

26.M. Maczka, S. Kojima, J. Hanuza. Raman spectroscopy of $KAl(MoO_4)_2$ and $NaAl(MoO_4)_2$ single crystals. *Journal of Raman spectroscopy* **1999**, 30 (4), 339-345. https://doi.org/10.1002/(SICI)1097-4555(199904)30:4<339::AID-JRS378>3.0.CO;2-8

27.A. Žalga, A. Diktanaitė, G. Gaidamavičienė. Aqueous sol–gel synthesis, thermoanalytical, structural and vibrational studies of lithium aluminium molybdate ($LiAlMo_2O_8$). *chemija* **2022**, 33 (4). https://doi.org/10.6001/chemija.v33i4.4806

28.M. Wang, J. You, A. Sobol, L. Lu, J. Wang, Y. Xie. In-situ studies of structure transformation and Al coordination of $KAl(MoO_4)_2$ during heating by high temperature Raman and ^{27}Al NMR spectroscopies. *Materials* **2017**, 10 (3), 310. https://doi.org/10.3390/ma10030310

29.P. E. Tomaszewski, A. Pietraszko, M. Maczka, J. Hanuza. $CsAl(MoO_4)_2$. *Acta Crystallographica Section E: Structure Reports Online* **2002**, 58 (12), i119-i120. https://doi.org/10.1107/S1600536802020950

30.G. Wang, L. Zhang, Z. Lin, G. Wang. Growth and spectroscopic characteristics of Cr^{3+}:$CsAl(MoO_4)_2$ crystal. *Journal of Alloys and Compounds* **2010**, 489 (1), 293-296. https://doi.org/10.1016/j.jallcom.2009.09.076

31.X. Gao, C. A. J. Fisher, T. Kimura, Y. H. Ikuhara, H. Moriwake, A. Kuwabara, H. Oki, T. Tojigamori, R. Huang, Y. Ikuhara. Lithium atom and A-site vacancy distributions in lanthanum lithium titanate. *Chemistry of Materials* **2013**, 25 (9), 1607-1614. https://doi.org/10.1021/cm3041357

32.S. Stramare, V. Thangadurai, W. Weppner. Lithium lanthanum titanates: a review. *Chemistry of Materials* **2003**, 15 (21), 3974-3990. https://doi.org/10.1021/cm0300516

33.X. Gao, C. A. J. Fisher, T. Kimura, Y. H. Ikuhara, A. Kuwabara, H. Moriwake, H. Oki, T. Tojigamori, K. Kohama, Y. Ikuhara. Domain boundary structures in lanthanum lithium titanates. *Journal of Materials Chemistry A* **2014**, 2 (3), 843-852. https://doi.org/10.1039/C3TA13726K

34.S. Kashida, T. Hori, K. Nakamura. X-Ray Study of the Superstructure in the Bi_2O_3–V_2O_5 System. *Journal of the Physical Society of Japan* **1994**, 63 (12), 4422-4426. https://doi.org/10.1143/JPSJ.63.4422

35.M. Touboul, C. Vachon. The Bi_2O_3-V_2O_5 system and crystal data about some bismuth vanadates. *Thermochimica Acta* **1988**, 133, 61-66. https://doi.org/10.1016/0040-6031(88)87137-5

36.S. Beg, S. Haneef, N. A. S. Al-Areqi. Study of electrical conductivity and phase transition in Bi_2O_3–V_2O_5 system. *Phase Transitions* **2010**, 83 (12), 1114-1125. https://doi.org/10.1080/01411594.2010.509642

37.L. P. Soloveva, S. V. Borisov. Crystal structure of $LiAl(MoO_4)_2$. *Kristallographia* **1970**, 15, 577-580.

38. D. E. Bugaris, H. C. Loye. $Li_3Al(MoO_4)_3$, a lyonsite molybdate. *Acta Crystallographica Section C: Crystal Structure Communications* **2012**, 68 (6), i34-i36. https://doi.org/10.1107/S0108270112020513

39. S. F. Solodovnikov, E. G. Khajkina, Z. A. Solodovnikova, Y. M. Kadyrova, K. M. Khal'baeva, E. S. Zolotova. New families of lithium containing triple molybdates and a stabilizing role of lithium in their structure formation. *Doklady Akademii Nauk-Rossijskaya Akademiya Nauk* **2007**, 416. https://doi.org/10.1134/S0012500807090029

40. U. Kolitsch, M. Maczka, J. Hanuza. $NaAl(MoO_4)_2$: a rare structure type among layered yavapaiite-related $AM(XO_4)_2$ compounds. *Acta Crystallographica Section E: Structure Reports Online* **2003**, 59 (2), i10-i13. https://doi.org/10.1107/S1600536803000990

41. P. V. Klevtsov, L. P. Kozeeva, R. F. Klevtsova. Synthese et symetrie des cristaux des molybdates doubles de na et fe, al, cr de composition $NaR^{3+}(MoO_4)_2$. *Zhurnal Neorganicheskoi Khimii* **1975**, 20, 2999-3002.

42. R. Klevtsova, P. Klevtsov. Synthesis and crystal structure of double molybdates $KR(MoO_4)_2$ FOR R^{3+}= A1, Sc, and Fe and tungstate $KSc(WO_4)_2$. *Soviet Physics Crystallography, USSR* **1971**, 15 (5), 829-+.

43. K. Hermanowicz. Spectroscopic properties of the rubidium and cesium aluminum double molybdate crystals. *Journal of luminescence* **2004**, 109 (1), 9-18. https://doi.org/10.1016/j.jlumin.2003.12.048

44. P. E. Tomaszewski, A. Pietraszko, M. Maczka, J. Hanuza. $CsAl(MoO_4)_2$. *Acta Crystallographica Section E: Structure Reports Online* **2002**, 58 (12), i119-i120. https://doi.org/10.1107/S1600536802020950

45. J. Brous, I. Fankuchen, E. Banks. Rare earth titanates with a perovskite structure. *Acta crystallographica* **1953**, 6 (1), 67-70. https://doi.org/10.1107/S0365110X53000156

46. J. L. Fourquet, H. Duroy, M. P. Crosnier-Lopez. Structural and microstructural studies of the series $La_{2/3-x}Li_{3x\square 1/3-2x}TiO_3$. *Journal of Solid State Chemistry* **1996**, 127 (2), 283-294. https://doi.org/10.1006/jssc.1996.0385

47. M. Sommariva, M. Catti. Neutron diffraction study of quenched $Li_{0.3}La_{0.567}TiO_3$ lithium ion conducting perovskite. *Chemistry of Materials* **2006**, 18 (9), 2411-2417. https://doi.org/10.1021/cm060120r

48. C. A. Kirk, A. R. West. Crystal structure of $La_{24}Li_{20}Ti_5O_{56}$: A pseudo-close-packed, columnar intergrowth stucture. *Journal of Solid State Chemistry* **2001**, 162 (2), 379-388. https://doi.org/10.1006/jssc.2001.9328

49. Y. Inaguma, T. Katsumata, M. Itoh, Y. Morii. Crystal structure of a lithium ion-conducting perovskite $La_{2/3-x}Li_{3x}TiO_3$ (x= 0.05). *Journal of Solid State Chemistry* **2002**, 166 (1), 67-72. https://doi.org/10.1006/jssc.2002.9560

50. M. Yashima, M. Itoh, Y. Inaguma, Y. Morii. Crystal structure and diffusion path in the fast lithium-ion conductor $La_{0.62}Li_{0.16}TiO_3$. *Journal of the American Chemical Society* **2005**, 127 (10), 3491-3495. https://doi.org/10.1021/ja0449224

51.C. A. Kirk, A. R. West. Crystal structure of the perovskite-related phase of approximate composition $LaLi_{1/3}Ti_{2/3}O_3$. *Solid State Sciences* **2002**, 4 (9), 1163-1166. https://doi.org/10.1016/S1293-2558(02)01386-9

52.A. Y. Borisevich, P. K. Davies. $La(Li_{1/3}T_{i2/3})O_3$: a new 1: 2 ordered perovskite. *Journal of Solid State Chemistry* **2003**, 170 (1), 198-201. https://doi.org/10.1016/S0022-4596(02)00064-6

53.J. Sanz, A. Varez, J. A. Alonso, M. T. Fernandez. Structural changes produced during heating of the fast ion conductor $Li_{0.18}La_{0.61}TiO_3$. A neutron diffraction study. *Journal of Solid State Chemistry* **2004**, 177 (4-5), 1157-1164. https://doi.org/10.1016/j.jssc.2003.10.036

54.S. García-Martín, M. A. Alario-Franco, H. Ehrenberg, J. Rodríguez-Carvajal, U. Amador. Crystal structure and microstructure of some $La_{2/3-x}Li_{3x}TiO_3$ oxides: an example of the complementary use of electron diffraction and microscopy and synchrotron X-ray diffraction to study complex materials. *Journal of the American Chemical Society* **2004**, 126 (11), 3587-3596. https://doi.org/10.1021/ja038410l

55.S. Tokunaga, H. Kato, A. Kudo. Selective preparation of monoclinic and tetragonal $BiVO_4$ with scheelite structure and their photocatalytic properties. *Chemistry of Materials* **2001**, 13 (12), 4624-4628. https://doi.org/10.1021/cm0103390

56.W. Wrobel, F. Krok, I. Abrahams, A. Kozanecka-Szmigiel, M. Malys, S. C. M. Chan, J. R. Dygas. $Bi_8V_2O_{17-a}$ Stable Phase in the Bi_2O_3-V_2O_5 System. *Materials Science-Poland* **2006**, 24, 23-30.

57.S. Kashida, T. Hori. X-Ray Study of the Cation Distribution in the Ternary Oxide, 6 Bi_2O_3–V_2O_5. *Journal of Solid State Chemistry* **1996**, 122 (2), 358-363. https://doi.org/10.1006/jssc.1996.0127

58.O. Joubert, A. Jouanneaux, M. Ganne. Crystal structure of low temperature form of $Bi_6V_3O_{16}$ determined by Rietveld refinement of synchrotron radiation powder diffraction data: A new mixed valence Aurivillius phase. *Nuclear Instruments and Methods in Physics Research Section B: Beam Interactions with Materials and Atoms* **1995**, 97 (1-4), 119-122. https://doi.org/10.1016/0168-583X(94)00383-1

59.E. Capoen, M. C. Steil, N. Tancret, G. Nowogrocki, J. C. Boivin, G. Mairesse, R. N. Vannier, M. Anne, O. Isnard. Time resolved in-situ neutron diffraction investigation of the electrochemical reduction of BIMEVOX. *Solid State Ionics* **2004**, 175 (1-4), 419-424. https://doi.org/10.1016/j.ssi.2004.03.052

60.A. Watanabe. Preparation and characterization of a new triclinic compound $Bi_{3.5}V_{1.2}O_{8.25}$ to show the known phase $Bi_4V_2O_{11}$ to be nonexistent as a single phase. *Journal of Solid State Chemistry* **2001**, 161 (2), 410-415. https://doi.org/10.1006/jssc.2001.9356

61.J. Darriet, J. C. Launay, F. J. Zúniga. Crystal structures of the ionic conductors $Bi_{46}M_8O_{89}$ (M= P, V) related to the fluorite-type structure. *Journal of Solid State Chemistry* **2005**, 178 (6), 1753-1764. https://doi.org/10.1016/j.jssc.2005.03.013

62.A. W. Sleight, H. Y. Chen, A. Ferretti, D. E. Cox. Crystal growth and structure of $BiVO_4$. *Materials Research Bulletin* **1979**, 14 (12), 1571-1581. https://doi.org/10.1016/0025-5408(72)90227-9

63.J. W. E. Mariathasan, R. M. Hazen, L. W. Finger. Crystal structure of the high-pressure form of $BiVO_4$. *Phase Transitions: A Multinational Journal* **1986**, 6 (3), 165-173. https://doi.org/10.1080/01411598608218306

64.R. N. Vannier, E. Pernot, M. Anne, O. Isnard, G. Nowogrocki, G. Mairesse. $Bi_4V_2O_{11}$ polymorph crystal structures related to their electrical properties. *Solid State Ionics* **2003**, 157 (1-4), 147-153. https://doi.org/10.1016/S0167-2738(02)00202-3

65.G. Mairesse, P. Roussel, R. N. Vannier, M. Anne, C. Pirovano, G. L. Nowogrocki. Crystal structure determination of α, β and γ-$Bi_4V_2O_{11}$ polymorphs. Part I: γ and β-$Bi_4V_2O_{11}$. *Solid State Sciences* **2003**, 5 (6), 851-859. https://doi.org/10.1016/S1293-2558(03)00015-3

66.G. Mairesse, P. Roussel, R. N. Vannier, M. Anne, G. Nowogrocki. Crystal structure determination of α-, β-and γ-$Bi_4V_2O_{11}$ polymorphs. Part II: crystal structure of α-$Bi_4V_2O_{11}$. *Solid State Sciences* **2003**, 5 (6), 861-869. https://doi.org/10.1016/S1293-2558(03)00016-5

67.O. Joubert, A. Jouanneaux, M. Ganne. Crystal structure of low-temperature form of bismuth vanadium oxide determined by rietveld refinement of X-ray and neutron diffraction data (α-$Bi_4V_2O_{11}$). *Materials Research Bulletin* **1994**, 29 (2), 175-184. https://doi.org/10.1016/0025-5408(94)90138-4

68.C. H. Chen, K. Amine. Ionic conductivity, lithium insertion and extraction of lanthanum lithium titanate. *Solid State Ionics* **2001**, 144 (1-2), 51-57. https://doi.org/10.1016/S0167-2738(01)00884-0

69.E. M. Valliant, J. R. Jones. Softening bioactive glass for bone regeneration: sol–gel hybrid materials. *Soft Matter* **2011**, 7 (11), 5083-5095. https://doi.org/10.1039/C0SM01348J

70.C. J. Brinker, G. W. Scherer. Sol-gel science: the physics and chemistry of sol-gel processing: Academic press; 2013.

71.M. Ebelmen. Chimie sur une production artificielle de silice diaphane. *Comptes rendus de l'Académie des Sciences* **1845**, 21, 502-505.

72.J. Zarzycki. Past and present of sol-gel science and technology. *Journal of Sol-Gel Science and Technology* **1997**, 8, 17-22. https://doi.org/10.1023/A:1026480424495

73.W. C. Lepry, S. N. Nazhat. A review of phosphate and borate sol–gel glasses for biomedical applications. *Advanced NanoBiomed Research* **2021**, 1 (3), 2000055. https://doi.org/10.1002/anbr.202000055

74.H. Dislich, P. Hinz. History and principles of the sol-gel process, and some new multicomponent oxide coatings. *Journal of Non-Crystalline Solids* **1982**, 48 (1), 11-16. https://doi.org/10.1016/0022-3093(82)90242-3

75.H. Dislich, E. Hussmann. Amorphous and crystalline dip coatings obtained from organometallic solutions: procedures, chemical processes and products. *Thin solid films* **1981**, 77 (1-3), 129-140. https://doi.org/10.1016/0040-6090(81)90369-2

76.G. M. Pajonk. A short history of the preparation of aerogels and carbogels. *Sol-Gel Processing and Applications* **1994**, 201-219. https://doi.org/10.1007/978-1-4615-2570-7_18

77.D. M. Roy, R. Roy. An experimental study of the formation and properties of synthetic serpentines and related layer silicate minerals. *American Mineralogist: Journal of Earth and Planetary Materials* **1954**, 39 (11-12), 957-975.

78.S. J. Teichner, G. A. Nicolaon, M. A. Vicarini, G. E. E. Gardes. Inorganic oxide aerogels. *Advances in Colloid and Interface Science* **1976**, 5 (3), 245-273. https://doi.org/10.1016/0001-8686(76)80004-8

79.K. Hermanowicz. Temperature-dependent ESR studies on the Cr^{3+} ion-doped $KAl(MoO_4)_2$ crystal. *Journal of Alloys and Compounds* **2002**, 341 (1-2), 179-182. https://doi.org/10.1016/S0925-8388(02)00065-8

80.A. Peña, R. Solé, J. Gavaldà, J. Massons, F. Díaz, M. Aguiló. Primary crystallization region of $NaAl(MoO_4)_2$, Cr^{3+} doping, crystal growth, and characterization. *Chemistry of Materials* **2006**, 18 (2), 442-448. https://doi.org/10.1021/cm052054j

81.G. Wang, X. Long, L. Zhang, G. Wang. Growth and thermal properties of Cr^{3+}: $KAl(MoO_4)_2$ crystal. *Journal of crystal growth* **2008**, 310 (3), 624-628. https://doi.org/10.1016/j.jcrysgro.2007.11.098

82.M. Maczka, K. Hermanowicz, P. E. Tomaszewski, M. Zawadzki, J. Hanuza. Vibrational and luminescence studies of $MIIn(MoO_4)_2$ (MI= K, Rb) and $MIAl(MoO_4)_2$ (MI= K, Na) molybdates doped with chromium (III) prepared via the Pechini method. *Optical Materials* **2008**, 31 (2), 167-175. https://doi.org/10.1016/j.optmat.2008.02.010

83.I. Koseva, V. Nikolov, A. Yordanova, P. Tzvetkov, D. Kovacheva. Preparation of nanosized sodium–aluminum tungstate, $NaAl(WO_4)_2$. *Journal of Alloys and Compounds* **2011**, 509 (25), 7022-7026. https://doi.org/10.1016/j.jallcom.2011.04.027

84.M. Mączka, K. Hermanowicz, L. Kępiński, J. Hanuza, A. Yordanova, I. Koseva. Raman spectroscopy and optical properties of nanocrystalline $NaAl(WO_4)_2:Cr^{3+}$ powders prepared by co-precipitation/calcination method. *Optical Materials* **2013**, 35 (3), 338-346. https://doi.org/10.1016/j.optmat.2012.09.003

85.M. Nagao. Crystal growth techniques for layered superconductors. *Condensed Matter* **2017**, 2 (4), 32. https://doi.org/10.3390/condmat2040032

86.K. Tonsuaadu, A. Žalga, A. Beganskienė, A. Kareiva. Thermoanalytical study of the YSZ precursors prepared by aqueous sol–gel synthesis route. *Journal of Thermal Analysis and Calorimetry* **2012**, 110 (1), 77-83. https://doi.org/10.1007/s10973-011-2184-3

87.G. Braziulis, R. Stankeviciute, A. Zalga. Sol-gel derived europium doped $CaMoO_4:Eu^{3+}$ with complex microstructural and optical properties. *Materials Science* **2014**, 20 (1), 90-96. https://doi.org/10.5755/j01.ms.20.1.4797

88.G. Braziulis, G. Janulevičius, R. Stankevičiutė, A. Žalga. Aqueous sol–gel synthesis and thermoanalytical study of the alkaline earth molybdate

precursors. *Journal of Thermal Analysis and Calorimetry* **2014**, 118, 613-621. https://doi.org/10.1007/s10973-013-3579-0

89. A. Žalga, A. Kareiva, A. Žarkov, S. Tautkus, B. Abakevičienė. UV-Vis spectroscopical investigations of the YSZ thin films on corundum, silicon and silica substrates. *chemija* **2014**, 25 (1), 29-33.

90. R. Stankevičiutė, A. Žalga. Sol–gel synthesis, crystal structure, surface morphology, and optical properties of Eu_2O_3-doped $La_2Mo_3O_{12}$ ceramic. *Journal of Thermal Analysis and Calorimetry* **2014**, 118, 925-935. https://doi.org/10.1007/s10973-014-3882-4

91. A. Žalga, Z. Moravec, J. Pinkas, A. Kareiva. On the sol–gel preparation of different tungstates and molybdates. *Journal of Thermal Analysis and Calorimetry* **2011**, 105 (1), 3-11. https://doi.org/10.1007/s10973-011-1367-2

92. M. H. Bhat, A. Miura, P. Vinatier, A. Levasseur, K. J. Rao. Microwave synthesis of lithium lanthanum titanate. *Solid state communications* **2003**, 125 (10), 557-562. https://doi.org/10.1016/S0038-1098(02)00852-9

93. Y. Huang, X. Liu, Y. Jiang, X. Zhu. Synthesis of textured $Li_{0.33}La_{0.55}TiO_3$ solid electrolytes by molten salt method. *Ceramics International* **2021**, 47 (8), 11654-11661. https://doi.org/10.1016/j.ceramint.2021.01.003

94. Y. J. Huang, Yue, Y. Zhou, X. Liu, X. Zeng, X. Zhu. One-step low-temperature synthesis of $Li_{0.33}La_{0.55}TiO_3$ solid electrolytes by tape casting method. *Ionics* **2021**, 27, 145-155. https://doi.org/10.1007/s11581-020-03823-y

95. C. Bohnke, B. Regrag, F. Le Berre, J. L. Fourquet, N. Randrianantoandro. Comparison of pH sensitivity of lithium lanthanum titanate obtained by sol–gel synthesis and solid state chemistry. *Solid State Ionics* **2005**, 176 (1-2), 73-80. https://doi.org/10.1016/j.ssi.2004.06.010

96. M. Vijayakumar, Y. Inaguma, W. Mashiko, M. P. Crosnier-Lopez, C. Bohnke. Synthesis of Fine Powders of $Li_{3x}La_{2/3-x}TiO_3$ Perovskite by a Polymerizable Precursor Method. *Chemistry of Materials* **2004**, 16 (14), 2719-2724. https://doi.org/10.1021/cm049869x

97. I. Carazeanu P., E. Chirila, V. Popescu, V. Ciupina, G. Prodan. Sol–gel preparation and characterization of perovskite lanthanum lithium titanate. *Journal of materials science* **2007**, 42, 3373-3377. https://doi.org/10.1007/s10853-006-0683-6

98. M. Romero, R. Faccio, S. Vázquez, S. Davyt, Á. W. Mombrú. Experimental and theoretical Raman study on the structure and microstructure of $Li_{0.30}La_{0.57}TiO_3$ electrolyte prepared by the sol-gel method in acetic medium. *Ceramics International* **2016**, 42 (14), 15414-15422. https://doi.org/10.1016/j.ceramint.2016.06.192

99. C. K. Lee, D. C. Sinclair, A. R. West. Stoichiometry and stability of bismuth vanadate, $Bi_4V_2O_{11}$, solid solutions. *Solid State Ionics* **1993**, 62 (3-4), 193-198. https://doi.org/10.1016/0167-2738(93)90372-A

100. J. Exner, P. Fuierer, R. Moos. Aerosol codeposition of ceramics: mixtures of Bi_2O_3–TiO_2 and Bi_2O_3–V_2O_5. *Journal of the American Ceramic Society* **2015**, 98 (3), 717-723. https://doi.org/10.1111/jace.13364

101.   J. Li, P. Lu, W. Deng, Z. Zeng, L. Lin, G. Zhao. Facile synthesis of sheet-like $BiVO_4/Bi_4V_2O_{11}$ composite for enhanced photocatalytic properties. *Materials Chemistry and Physics* **2020**, 254, 123489. https://doi.org/10.1016/j.matchemphys.2020.123489

102.   S. Kumar, P. D. Sahare. Synthesis of α-$Bi_4V_2O_{11}$ and its Sonocatalytic Activity for the Degradation of Rhodamine B. *Journal of luminescence* **2014**, 1 (2), 73-86. https://doi.org/10.7726/jla.2014.1007

103.   P. Pookmanee, S. Kojinok, R. Puntharod, S. Sangsrichan, S. Phanichphant. Preparation and characterization of $BiVO_4$ powder by the sol-gel method. *Ferroelectrics* **2013**, 456 (1), 45-54. https://doi.org/10.1080/00150193.2013.846197

104.   W. H. Suh, A. R. Jang, Y. H. Suh, K. S. Suslick. Porous, hollow, and ball-in-ball metal oxide microspheres: preparation, endocytosis, and cytotoxicity. *Advanced Materials* **2006**, 18 (14), 1832-1837. https://doi.org/10.1002/adma.200600222

105.   S. S. Dunkle, R. J. Helmich, K. S. Suslick. $BiVO_4$ as a visible-light photocatalyst prepared by ultrasonic spray pyrolysis. *The Journal of Physical Chemistry C* **2009**, 113 (28), 11980-11983. https://doi.org/10.1021/jp903757x

106.   M. Maczka, J. Hanuza, E. T. G. Lutz, J. H. Van der Maas. Infrared Activity of $KAl(MoO_4)_2$ and $NaAl(MoO_4)_2$. *Journal of Solid State Chemistry* **1999**, 145 (2), 751-756. https://doi.org/10.1006/jssc.1999.8300

107.   V. Chornii, Y. Hizhnyi, S. Nedilko, P. Nagornyi, R. Boiko. VUV spectroscopy and electronic structure of the Cr-doped $NaAl(MoO_4)_2$ double molybdates.

108.   G. J. Wang, Y. S. Huang, L. Z. Zhang, Z. B. Lin, G. F. Wang. Growth and spectral properties of $Cr^{3+}/RbAl(MoO_4)_2$ crystal. *Materials Research Innovations* **2011**, 15 (3), 167-171. https://doi.org/10.1179/143307511X12998222919191

109.   J. Z. Lee, Z. Wang, H. L. Xin, T. A. Wynn, Y. S. Meng. Amorphous lithium lanthanum titanate for solid-state microbatteries. *Journal of the Electrochemical Society* **2016**, 164 (1), A6268. https://doi.org/10.1149/2.0411701jes

110.   L. Fan, S. Wei, S. Li, Q. Li, Y. T. Lu. Recent progress of the solid-state electrolytes for high-energy metal-based batteries. *Advanced Energy Materials* **2018**, 8 (11), 1702657. https://doi.org/10.1002/aenm.201702657

111.   Y. Chen, Y. Kang, Y. Zhao, L. Wang, J. Liu, Y. Z. Li, Z. Liang, X. He, X. Li, N. Tavajohi. A review of lithium-ion battery safety concerns: The issues, strategies, and testing standards. *Journal of Energy Chemistry* **2021**, 59, 83-99. https://doi.org/10.1016/j.jechem.2020.10.017

112.   A. R. Symington, M. Molinari, J. A. Dawson, J. M. Statham, J. Purton, P. Canepa, S. C. Parker. Elucidating the nature of grain boundary resistance in lithium lanthanum titanate. *Journal of Materials Chemistry A* **2021**, 9 (10), 6487-6498. https://doi.org/10.1039/D0TA11539H

113.   B. Jinisha, K. M. Anilkumar, M. Manoj, V. S. Pradeep, S. J. E. A. Jayalekshmi. Development of a novel type of solid polymer electrolyte for

solid state lithium battery applications based on lithium enriched poly (ethylene oxide)(PEO)/poly (vinyl pyrrolidone)(PVP) blend polymer. *Electrochimica Acta* **2017**, 235, 210-222. https://doi.org/10.1016/j.electacta.2017.03.118

114.   Q. Lei, J. Guo, A. Noureddine, A. Wang, S. Wuttke, C. J. Brinker, W. Zhu. Sol–gel-based advanced porous silica materials for biomedical applications. *Advanced Functional Materials* **2020**, 30 (41), 1909539. https://doi.org/10.1002/adfm.201909539

115.   C. K. Rhee, Y. B. Chun, S. H. Kang, W. W. Kim, G. Cao. Lithium-Ion Conductive Film Membrane of $Li_{0.3}La_{0.57}TiO_2$ Perovskite Structure and its Application in Li-Air Batteries. *Archives of Metallurgy and Materials* **2023**, 191-194-191-194. https://doi.org/10.24425/amm.2023.141493

116.   A. Suryatna, I. Raya, L. Thangavelu, F. R. Alhachami, M. M. Kadhim, U. S. Altimari, Z. H. Mahmoud, Y. F. Mustafa, E. Kianfar. A review of high-energy density lithium-air battery technology: investigating the effect of oxides and nanocatalysts. *Journal of Chemistry* **2022**, 2022. https://doi.org/10.1155/2022/2762647

117.   Y. H. Cho, J. Wolfenstine, E. Rangasamy, H. Kim, H. Choe, J. Sakamoto. Mechanical properties of the solid Li-ion conducting electrolyte: $Li_{0.33}La_{0.57}TiO_3$. *Journal of materials science* **2012**, 47, 5970-5977. https://doi.org/10.1007/s10853-012-6500-5

118.   P. Upreti, L. E. Metzger, P. Bühlmann. Glass and polymeric membrane electrodes for the measurement of pH in milk and cheese. *Talanta* **2004**, 63 (1), 139-148. https://doi.org/10.1016/j.talanta.2003.12.020

119.   Z. Wiśniewski, R. Wiśniewski, J. L. Nowiński. Application of foil strain gauges in high pressure research. *Review of Scientific Instruments* **2001**, 72 (6), 2829-2831. https://doi.org/10.1063/1.1367365

120.   J. W. Kim, K. B. Kim, J. H. Kim, N. K. Min. Bulk-micromachined, SOI-based half-bridge silicon strain gauges for high pressure applications. *Journal of Micromechanics and Microengineering* **2018**, 28 (12), 125004. https://doi.org/10.1088/1361-6439/aae592

121.   K. Arshak, R. Perrem. Fabrication of a thin-film strain-gauge transducer using Bi_2O_3 - V_2O_5. *Sensors and Actuators A: Physical* **1993**, 36 (1), 73-76. https://doi.org/10.1016/0924-4247(93)80143-5

122.   M. G. Walter, E. L. Warren, J. R. McKone, S. W. Boettcher, Q. Mi, E. A. Santori, N. S. Lewis. Solar water splitting cells. *Chemical reviews* **2010**, 110 (11), 6446-6473. https://doi.org/10.1021/cr1002326

123.   W. Wang, P. J. Strohbeen, D. Lee, C. Zhou, J. K. Kawasaki, K. S. Choi, M. Liu, G. Galli. The role of surface oxygen vacancies in $BiVO_4$. *Chemistry of Materials* **2020**, 32 (7), 2899-2909. https://doi.org/10.1021/acs.chemmater.9b05047

124.   Z. Zheng, J. He, C. Dong, I. M. C. Lo. Photoelectrochemical sewage treatment by sulfite activation over an optimized $BiVO_4$ photoanode to simultaneously promote PPCPs degradation, H_2 evolution and E. coli

disinfection. *Chemical Engineering Journal* **2021**, 419, 129418. https://doi.org/10.1016/j.cej.2021.129418

125. S. Ghotekar, K. Pagar, S. Pansambal, H. A. Murthy, R. Oza. A review on eco-friendly synthesis of $BiVO_4$ nanoparticle and its eclectic applications. *Advanced Journal of Science and Engineering* **2020**, 1 (4), 106-112. https://doi.org/10.22034/AJSE2014106

126. Q. H. Alijani, S. Iravani, R. S. Varma. Bismuth Vanadate ($BiVO_4$) Nanostructures: Eco-Friendly Synthesis and Their Photocatalytic Applications. *Catalysts* **2022**, 13 (1), 59. https://doi.org/10.3390/catal13010059

127. J. J. Cruywagen, J. B. B. Heyns, E. A. Rohwer. Molybdenum (VI) complex formation. Part 4. Equilibria and thermodynamic quantities for the reactions with tartrate in 1.0 mol dm-3 sodium chloride. **1990**.

128. A. Žalga, G. Gaidamavičienė, Ž. Gricius, E. Užpurvytė, J. Gadeikis, A. Diktanaitė, M. Barre, T. Šalkus, A. Kežionis, E. Kazakevičius. Aqueous sol-gel synthesis, thermoanalytical study and electrical properties of $La_2Mo_2O_9$. *Journal of Thermal Analysis and Calorimetry* **2018**, 132 (3), 1499-1511. https://doi.org/10.1007/s10973-018-7120-3

129. E. C. Housecroft, A. A. Sharpe. Inorganic chemistry. Fourth ed: Pearson Education Limited; 2012. 1257 p.

130. W. Frank, G. J. Reiss, J. Schneider. The nonaaquabismuth(III) cation. *Angewandte Chemie-International Edition in English* **1995**, 34 (21), 2416-2417. https://doi.org/10.1002/anie.199524161

131. C. C. Pye, C. M. Gunasekara, W. W. Rudolph. An ab initio investigation of bismuth hydration. *Canadian Journal of Chemistry-Revue Canadienne De Chimie* **2007**, 85 (11), 945-950. https://doi.org/10.1139/v07-108

132. E. Kazakevicius, A. Kezionis, S. Kazlauskas, A. Zalga, M. Barre, R. Juskenas. Phase transformations in $La_{2-x}Y_xMo_2O_9$ (x=0.05, x=0.075): Temperature cycling and DRT analysis. *Solid State Ionics* **2019**, 339. https://doi.org/10.1016/j.ssi.2019.05.024

133. A. Diktanaite, G. Gaidamaviciene, E. Kazakevicius, A. Kezionis, A. Zalga. Aqueous sol-gel synthesis, thermal analysis, characterization and electrical properties of V_2O_5 doped Bi_2O_3 system. *Thermochimica Acta* **2020**, 685. https://doi.org/10.1016/j.tca.2020.178511

134. A. Kezionis, E. Kazakevicius, S. Kazlauskas, A. Zalga. Metal-like temperature dependent conductivity in fast Li^+ ionic conductor Lithium Lanthanum Titanate. *Solid State Ionics* **2019**, 342. https://doi.org/10.1016/j.ssi.2019.115060

135. M. L. Ruiz, I. D. Lick, M. I. Ponzi, E. R. Castellón, A. Jiménez-López, E. N. Ponzi. Thermal decomposition of supported lithium nitrate catalysts. *Thermochimica Acta* **2010**, 499 (1-2), 21-26. https://doi.org/10.1016/j.tca.2009.10.016

136.   F. D. Chattaway, F. E. Ray. II.—The decomposition of tartaric acid by heat. *Journal of the Chemical Society, Transactions* **1921**, 119, 34-37. https://doi.org/10.1039/CT9211900034

137.   G. Gaidamavičienė, A. Žalga. Synthesis, a structural and thermoanalytical study of $Ca_{1-x}Sr_xMoO_4$ ceramic. *Materials Chemistry and Physics* **2020**, 241. https://doi.org/10.1016/j.matchemphys.2019.122339

138.   Y. Inaguma, T. Katsumata, M. Itoh, Y. Morii, T. Tsurui. Structural investigations of migration pathways in lithium ion-conducting $La_{2/3−x}Li_{3x}TiO_3$ perovskites. *Solid State Ionics* **2006**, 177 (35-36), 3037-3044. https://doi.org/10.1016/j.ssi.2006.08.012

139.   T. Sato, S. Takagi, S. Deledda, B. C. Hauback, S.-i. Orimo. Extending the applicability of the Goldschmidt tolerance factor to arbitrary ionic compounds. *Scientific reports* **2016**, 6 (1), 1-10. https://doi.org/10.1038/srep23592

140.   W.-C. Lee, C.-Y. Huang, L.-K. Tsao, Y.-C. Wu. Chemical composition and tolerance factor at the morphotropic phase boundary in $(Bi_{0.5}Na_{0.5})TiO_3$-based piezoelectric ceramics. *Journal of the European Ceramic Society* **2009**, 29 (8), 1443-1448. https://doi.org/10.1016/j.jeurceramsoc.2008.08.028

141.   R. D. Shannon. Revised effective ionic radii and systematic studies of interatomic distances in halides and chalcogenides. *Acta crystallographica section A: crystal physics, diffraction, theoretical and general crystallography* **1976**, 32 (5), 751-767. https://doi.org/10.1107/S0567739476001551

142.   A. S. Bhalla, R. Y. Guo, R. Roy. The perovskite structure - a review of its role in ceramic science and technology. *Materials Research Innovations* **2000**, 4 (1), 3-26. https://doi.org/10.1007/s100190000062

143.   R. Ketkaew, Y. Tantirungrotechai, P. Harding, G. Chastanet, P. Guionneau, M. Marchivie, D. J. Harding. OctaDist: a tool for calculating distortion parameters in spin crossover and coordination complexes. *Dalton Transactions* **2021**, 50 (3), 1086-1096. https://doi.org/10.1039/d0dt03988h

144.   M. Catti, M. Sommariva, R. M. Ibberson. Tetragonal superstructure and thermal history of $Li_{0.3}La_{0.567}TiO_3$ (LLTO) solid electrolyte by neutron diffraction. *Journal of Materials Chemistry* **2007**, 17 (13), 1300-1307. https://doi.org/10.1039/B614345H

145.   O. Labidi, M. Drache, P. Roussel, J.-P. Wignacourt. $(MBi)_{46}V_8O_y$-family type (M= Pb, Sr, Ca, Cd, $Na_{0.5}Bi_{0.5}$): Syntheses, crystal structures and conductivity properties. *Solid State Sciences* **2008**, 10 (8), 1074-1082. https://doi.org/10.1016/j.solidstatesciences.2007.11.014

146.   L. S. Cavalcante, J. C. Sczancoski, J. W. M. Espinosa, J. A. Varela, P. S. Pizani, E. Longo. Photoluminescent behavior of $BaWO_4$ powders processed in microwave-hydrothermal. *Journal of Alloys and Compounds* **2009**, 474 (1-2), 195-200. https://doi.org/10.1016/j.jallcom.2008.06.049

147.   B. Fu, Q. Shen, W. Qian, Y. Zeng, X. Sun, M. Hannig. Interfacial interaction of tartaric acid with hydroxyapatite and enamel. *Journal of Materials Science-Materials in Medicine* **2005**, 16 (9), 827-831. https://doi.org/10.1007/s10856-005-3581-6

148.   V. Sasikala, D. Sajan, N. Vijayan, K. Chaitanya, M. S. B. Raj, B. H. S. Joy. Growth, molecular structure, NBO analysis and vibrational spectral analysis of L-tartaric acid single crystal. *Spectrochimica Acta Part a-Molecular and Biomolecular Spectroscopy* **2014**, 123, 127-141. https://doi.org/10.1016/j.saa.2013.12.045

149.   Z. Dega-Szafran, G. Dutkiewicz, Z. Kosturkiewicz, M. Szafran. Structure of complex of N-methylpiperidine betaine with p-hydroxybenzoic acid studied by X-ray, FT-IR and DFT methods. *Journal of Molecular Structure* **2008**, 875 (1-3), 346-353. https://doi.org/10.1016/j.molstruc.2007.05.013

150.   M. Maczka, J. Hanuza, A. Pietraszko. Vibrational and X-ray studies of the polymorphic forms of $LiIn(MoO_4)_2$. *Journal of Solid State Chemistry* **2000**, 154 (2), 498-506. https://doi.org/10.1006/jssc.2000.8870

151.   J. Hanuza, M. Maczka. Vibrational properties of the double molybdates $MX(MoO_4)_2$ family (M=Li,Na,K,Cs, X=Bi,Cr). *Vibrational Spectroscopy* **1994**, 7 (1), 85-96. https://doi.org/10.1016/0924-2031(94)85044-5

152.   V. P. M. Pillai, T. Pradeep, M. J. Bushiri, R. S. Jayasree, V. U. Nayar. Vibrational spectroscopic studies of $FeClMoO_4$, Na_2MoO_4 and Na_2MoO_4 center dot $2H_2O/D_2O$. *Spectrochimica Acta Part a-Molecular and Biomolecular Spectroscopy* **1997**, 53 (6), 867-876. https://doi.org/10.1016/S1386-1425(96)01853-7

153.   A. I. Ruiz, M. L. Lopez, M. L. Veiga, C. Pico. Electrical properties of $La_{1.33-x}Li_{3x}Ti_2O_6$ (0.1 < x < 0.3). *Solid State Ionics* **1998**, 112 (3-4), 291-297. https://doi.org/10.1016/S0167-2738(98)00220-3

154.   Y. Inaguma, L. Q. Chen, M. Itoh, T. Nakamura. Candidate compounds with perovskite structure for high lithium ionic conductivity. *Solid State Ionics* **1994**, 70, 196-202. https://doi.org/10.1016/0167-2738(94)90309-3

155.   M. Kotobuki, S. Okuda, H. Munakata, K. Kanamura. Fabrication of $Li_{0.35}La_{0.55}TiO_3$ solid electrolyte with two-layered structure for all-solid-state Li battery by a colloidal crystal templating method. *Journal of the Ceramic Society of Japan* **2011**, 119 (1387), 189-193. https://doi.org/10.2109/jcersj2.119.189

156.   K. P. Abhilash, P. C. Selvin, B. Nalini, P. Nithyadharseni, B. C. Pillai. Investigations on pure and Ag doped lithium lanthanum titanate (LLTO) nanocrystalline ceramic electrolytes for rechargeable lithium-ion batteries. *Ceramics International* **2013**, 39 (2), 947-952. https://doi.org/10.1016/j.ceramint.2012.07.011

157.   Y. L. Xiong, H. Z. Tao, J. A. Zhao, H. Cheng, X. J. Zhao. Effects of annealing temperature on structure and opt-electric properties of ion-conducting LLTO thin films prepared by RF magnetron sputtering. *Journal of Alloys and Compounds* **2011**, 509 (5), 1910-1914. https://doi.org/10.1016/j.jallcom.2010.10.086

158.   B. Y. Li, Q. M. Su, L. T. Yu, D. Wang, S. K. Ding, M. Zhang, G. H. Du, B. S. Xu. $Li_{0.35}La_{0.55}TiO_3$ Nanofibers Enhanced Poly(vinylidene fluoride)-Based Composite Polymer Electrolytes for All-Solid-State Batteries. *Acs*

Applied Materials & Interfaces **2019**, 11 (45), 42206-42213. https://doi.org/10.1021/acsami.9b14824

159. D. S. Khaerudini, G. Guan, P. Zhang, A. Abudula. Oxide ion conductors based on niobium-doped bismuth vanadate: conductivity and phase transition features. *Ionics* **2016**, 22 (1), 93-97. https://doi.org/10.1007/s11581-015-1518-8

160. Y. T. Lu, L. Y. Chen, Y. Z. Li, H. D. Xie, H. Cheng, H. J. Seo. A new bismuth vanadate photocatalyst of $Bi_{23}V_4O_{44.5}$ nanoplates with layered delta-Bi_2O_3 based fluorite-type superstructures. *Materials Letters* **2016**, 164, 308-311. https://doi.org/10.1016/j.matlet.2015.08.044

SANTRAUKA

ĮVADAS

Tikriausiai sunku būtų rasti tokią pramonę, kuri vienu ar kitu būdu neturėtų naudos iš daugiakomponenčių kristalinių oksidų. Mobilieji telefonai, nešiojamieji kompiuteriai, elektriniai ir hibridiniai automobiliai, slėgio jutikliai, optiniai lazeriai, maisto fermentacija, pH indikatoriai, dujų jutikliai, vandens skaidymas, vandenynų tyrinėjimai, medicina ar net branduolinė įranga – tai tik keletas galimų ličio aliuminio molibdatų, ličio lantano titanatų ir bismuto vanadatų panaudijimo sričių. Šios medžiagos vaidina svarbų vaidmenį daugelyje skirtingų mokslo sričių ir pramonės šakų dėl savo unikalios struktūros ir vertinamų savybių, galinčių padaryti mūsų kasdienį gyvenimą saugesniu, prieinamesniu ir tvaresniu.

Šiuo metu plačiai naudojamos ličio baterijos, kuriose yra degių tirpiklių, ir kurios prisideda prie aplinkos atliekų, galėtų būti pakeistos 5–10 kartų patvaresnėmis ir saugesnėmis baterijomis, patobulintomis ličio lantano titano oksidais (LLTO). Perovskito struktūros LLTO turi labai aukštą joninį laidumą ir mažą aktyvacijos energiją, todėl puikiai tinka saugesnei energijos kaupimo prietaisų gamybai. Jų cheminis stabilumas ir gebėjimas atlaikyti atšiaurias pH sąlygas leidžia LLTO medžiagas naudoti ir naftos gręžimo pramonėje, nustatyti vandenilio sulfido dujas ir taip užkirsti kelią mirtiniems atvejams, kurie įvyko visai netolimoje praeityje.

Pasaulio gyventojų skaičius jau siekia aštuonis milijardus, todėl rasti būdų, kaip gaminti švarią, atsinaujinančią energiją, tapo neišvengiama užduotis. Vėjo ir saulės energijos gamyba yra veiksmingi atsinaujinančios energijos gamybos būdai, tačiau jie vis dar kenkia aplinkai – žinoma, kad dėl vėjo turbinų miršta paukščiai laukinėje gamtoje, o saulės energija gaminama naudojant tirpiklius, naftą ir pavojingas atliekas, kurie prisideda prie aplinkos taršos. Monoklininis šelitas $BiVO_4$ galėtų būti naudojamas kaip fotoanodas šioms problemoms spręsti - gaminant atsinaujinančią energiją vandens skaidymo būdu. Dėl gero laidumo ir didelio cheminio stabilumo bismuto vanadžio oksidas gali atlikti pagrindinį vaidmenį gaminant švarią, atsinaujinančią energiją, kuri nedaro neigiamo poveikio aplinkai.

Šarminių metalų aliuminio molibdatai, nors dar nėra plačiai ištirti, dėl savo optinių ir feroelastinių savybių turi daug potencialo optinių įrenginių gamyboje. Jie yra legiruoti retųjų žemių jonais, todėl juos galima naudoti derinamuosiuose lazeriuose, kai reikia itin didelio tikslumo ir pakartojamumo.

Šie daugiakomponenčiai oksidai suteikia galimybę efektyviai pagerinti mūsų gyvenimą, tačiau visa tai įmanoma tik supratus jų struktūrą, savybes ir paruošimo sintezę.

Pagrindinis šio daktaro disertacijos tikslas – vandeninių zolių-gelių paruošimo technikos taikymas homogeninių metalų tartratų gelio pirmtakų gamybai ir skirtingų vienfazių daugiakomponentių oksidų tyrimas. Remiantis šiuo tikslu, issikeltos pagrindinės tyrimo užduotys:

1. Trijų skirtingų daugiakomponenčių sistemų ($LiAlMo_2O_8$, $Li_{0.35}La_{0.55}TiO_3$ ir $5Bi_2O_3 \cdot V_2O_5$) paruošimas naudojant vandeninį zolių-gelių metodą ir vyno rūgštį.
2. Vyno rūgšties skilimo mechanizmo projektavimas ir išsamus atitinkamų metalinių tartratų gelio pirmtakų terminio skilimo tyrimas termogravimetrinės ir diferencinės skenavimo kalorimetrijos analizėmis.
3. Galutinių daugiakomponenčių metalų oksidų kristalinių fazių susidarymo tyrimas taikant rentgeno spindulių difrakcijos metodą.
4. Gautos keramikos, kaitinamos skirtingomis temperatūromis, paviršiaus morfologijos nustatymas skenuojančia elektronine mikroskopija.
5. Gautos keramikos atitinkamos kristalinės sudėties fizinių savybių demonstravimas ir patvirtinimas naudojant impedanso spektroskopiją.

Darbo rezultatai, leidžia ginti šiuos disertacijos ginamuosius teiginius:

1. Pirmą kartą sėkmingai pasiūlyta ir pritaikyta vandeninės vyno rūgšties zolių-gelių sintezės technika $LiAlMo_2O_8$, $Li_{0.35}La_{0.55}TiO_3$ ir $5Bi_2O_3 \cdot V_2O_5$ daugiakomponenčių oksidų gamybai.
2. TGA–DSC yra naudingas ir tinkamas įrankis tiek Li–Al–Mo–O, Li–La–Ti–O ir Bi–V–O tartratų gelių pirmtakų skilimo mechanizmų tyrimams, tiek galutinių $LiAlMo_2O_8$, $Li_{0.35}La_{0.55}TiO_3$ ir $5Bi_2O_3 \cdot V_2O_5$ keraminių medžiagų kristalizacijos įvertinimui.
3. Ligando pobūdis yra kritiškai svarbus zolių-gelių procesams, nes jis stipriai įtakoja gautų junginių morfologines, struktūrines ir elektrines savybes.
4. Terminis apdorojimas turi reikšmingos įtakos tiek sintezuotų gelio pirmtakų skilimui, tiek galutinės keramikos kristalizacijai.

5. Terminės analizės ir skirtingų charakterizavimo metodų derinimas yra naudinga priemonė, leidžianti parodyti gautos keramikos cheminių ir fizikinių savybių ryšius.

EKSPERIMENTO METODIKA

Šiame skyriuje aprašomi būdingi vandeninių zolių-gelių metodo technikos ypatumai. Taip pat pridedamas naudotų medžiagų, reagentų ir įrangos aprašymas.

MEDŽIAGOS IR REAGENTAI

Medžiagos ir reagentai atitinkamoms sintezėms buvo perkami iš tiekėjų, išvardytų kiekvienos medžiagos aprašyme. Toliau pateikiamas junginio pavadinimas, formulė, grynumas ir tiekėjas: aliuminio (III) nitratas nonahidratas, $Al(NO_3)_3 \cdot 9H_2O$, 99 %, Alfa Aesar; bismuto (III) oksidas, Bi_2O_3, 99,99%, Alfa Aesar; lantano (III) oksidas, La_2O_3, 99,9 %, Alfa Aesar; ličio nitratas, $LiNO_3$, 99 %, Alfa Aesar; molibdeno (VI) oksidas, MoO_3, 99,95%, Alfa Aesar; titano milteliai, Ti, 99,4 %, Alfa Aesar; vanadžio (V) oksidas, V_2O_5, 99,8%, Alfa Aesar.

Kompleksus su metalais sudarantis agentas ir reagentai pH reguliuoti vandeniniame tirpale pateikiami taip: L–(+)–vyno rūgštis, $C_4H_6O_6$, 99,5%, Roth; amoniako vandeninis tirpalas $NH_3 \cdot H_2O$, 25 %, Penta; druskos rūgštis, HCl, 35 – 38 % Chempur; azoto rūgštis, HNO_3, 66 % Reachem.

SINTEZĖS METODIKA

Įvairių metalo tartrato gelio pirmtakų $LiAl(MoO_4)_2$, $Li_{0.35}La_{0.55}TiO_3$ ir $5Bi_2O_3 \cdot V_2O_5$ keramikai sintezės buvo gautos vandeniniu zolių-gelių sintezės būdu, naudojant vyno rūgštį kaip kompleksus su metalais sudarantį reagentą, kuris sąveikauja kaip molekulinio lygio ligandas su reakcijos mišiniu tiek tirpstant vandenyje, tiek formuojantis zoliui-geliui.

Li–Al–Mo–O TARTRATO GELIO PIRMTAKO PARUOŠIMAS

Bendra Li–Al–Mo–O tartrato gelio pirmtako $LiAlMo_2O_8$ keramikai sintezės schema pavaizduota ir pateikta 22 pav. Pirmajame šio paruošimo technikos etape nedideliame kiekyje buvo ištirpinti molibdeno (VI) oksido milteliai nedideliame kiekyje koncentruoto amoniako vandeninio tirpalo.

117

Kaip parodyta 1 lygtyje, molibdeno (VI) oksidas ištirpsta karštame koncentruotame amoniako tirpale, sudarydamas NH_4^+ ir MoO_4^{2-} jonus.

$$MoO_3 \text{ (k)} + 2\, NH_3 \cdot H_2O \text{ (aq)} \rightarrow 2\, NH_4^+ \text{ (aq)} + MoO_4^{2-} \text{ (aq)} + 2\, H_2O \text{ (s)} \quad (1)$$
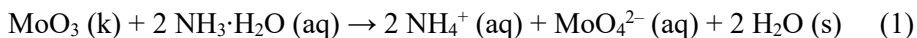
Amoniako perteklius iš reakcijos mišinio pašalinamas toliau kaitinant reakcijos mišinį, kol išgaruoja 90 % vandens. Į reakcijos mišinį įdėjus vyno rūgšties (TA), susidaro koordinacinis junginys $[(MoO_4)_p(C_4H_4O_6)_qH_r]^{(2p+2q-r)}$. Paprastai cheminė reakcija, įvykusi po šios procedūros, gali būti parašyta taip, kaip parodyta antroje lygtyje.

$$p\, (NH_4)_2MoO_4 \text{ (aq)} + q\, C_4H_6O_6 \text{ (aq)} \rightarrow$$
$$\rightarrow [(MoO_4)_p(C_4H_4O_6)_qH_r]^{(2p+2q-r)-} \text{ (aq)} + 2p\, NH_4^+ \text{ (aq)} \quad (2)$$

Tokią apsauginę aplinką nuo pH pokyčių nesunkiai sukuria vyno rūgštis, kuri koordinuoja atitinkamus molibdato kompleksus ir neleidžia įvykti hidrolizės reakcijai dėl kurios susidarytų nuosėdos. Be to, į reakcijos mišinį įpylus ličio (I) nitrato ir aliuminio (III) nitrato nonahidrato, gautas skaidrus tirpalas papildomai keletą valandų maišomas atviroje stiklinėje 85 ºC – 90 ºC temperatūroje. Gaunamas skaidrus blyškiai gelsvas atitinkamų metalų jonų zolis, kuris vėliau yra sukoncentruotas lėtai garin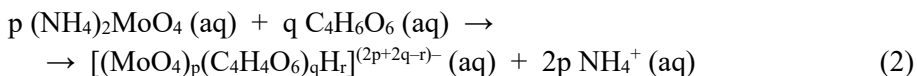ant reakcijos mišinį 90 ºC temperatūroje. Išdžiovinus orkaitėje 120 ºC temperatūroje gauti smulkūs šviesiai geltoni gelio milteliai.

Li–La–Ti–O TARTRATO GELIO PIRMTAKO PARUOŠIMAS

Bendra Li-La-Ti-O tartrato gelio pirmtako $Li_{0.35}La_{0.55}TiO_3$ keramikai sintezės schema atitinkamai pavaizduota ir pateikta 23 pav.

Pirmajame šio paruošimo technikos etape titano milteliai buvo ištirpinti koncentruotame vandeniniame druskos rūgšties tirpale. Kaip parodyta 3 lygtyje, titaną veikia karštas HCl, sudarydamas Ti(III) ir H_2 dujas.

$$2\, Ti \text{ (k)} + 6\, HCl \text{ (aq)} \rightarrow 2\, Ti^{3+} \text{ (aq)} + 6\, Cl^- \text{ (aq)} + 3\, H_2 \text{ (d)} \quad (3)$$

Šį cheminį procesą patvirtina reakcijos mišinyje susidaręs purpurinis $[Ti(OH_2)_6]^{3+}$ jonas. Žinant, kad ši koordinacinė dalelė yra stiprus reduktorius (4 lygtis), vandeniniai Ti(III) tirpalai turi būti apsaugoti nuo oksidacijos ore.

$$[TiO]^{2+} \text{ (aq)} + 2\, H^+ \text{ (aq)} + e^- \leftrightarrow Ti^{3+} \text{ (aq)} + H_2O \text{ (s)}\, (E^o = +0.1 \text{ V}) \quad (4)$$
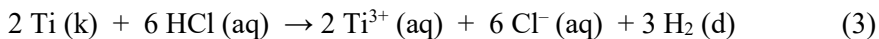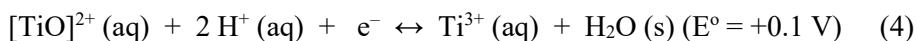
Tokią apsauginę aplinką nuo oksidacijos nesunkiai sukuria vyno rūgštis, kuri koordinuoja atitinkamus titano kompleksus ir neleidžia įvykti hidrolizei bei susidaryti nuosėdoms $TiO_2 \cdot 2H_2O$ pavidalu. Nepaisant to, Ti^{3+} jonų oksidacija įvyko iškart po ličio nitrato pridėjimo į reakcijos mišinį. Dėl to išsiskyrė daug azoto dioksido dujų ir dingo purpurinė tirpalo spalva. Šis skaidraus bespalvio vandeninio tirpalo susidarymas apibūdinamas 5 lygtimi.

$$Ti^{3+} (aq) + 2 H^+ (aq) + NO_3^- (aq) \rightarrow Ti^{4+} (aq) + NO_2 (d) + H_2O (s) \quad (5)$$
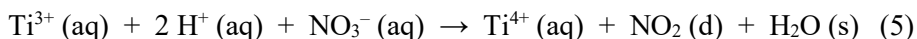
Nuosėdų nebuvimas reakcijos mišinyje patvirtino vyno rūgšties, kaip ligando, svarbą stabilizuojant Ti(IV) joną vandeniniame tirpale ir užkertant kelią jo hidrolizei, kurią aprašo 6 lygtis.

$$[Ti(OH_2)_6]^{4+} (aq) + 4 H_2O (s) \rightarrow TiO_2 \cdot 4 H_2O (k) + 4 H_3O^+ (aq) \quad (6)$$

Tikslų vyno rūgšties, koordinuojančios Ti^{4+} joną, kiekį galima sėkmingai nustatyti termiškai skaidant Li-La-Ti-O tartrato gelio pirmtaką. Be to, pridėjus lantano (III) oksido, susidarė galutinės sudėties Li-La-Ti-O tartrato gelio pirmtakas, skirtas $La_{0.55}Li_{0.35}TiO_3$. Gautas skaidrus bespalvis atitinkamų metalų jonų vandeninis tirpalas, kuris vėliau sukoncentruotas lėtai garinant reakcijos mišinį 90 ºC temperatūroje. Išdžiovinus džiovinimo krosnyje 120 ºC temperatūroje gauti smulkūs šviesiai geltoni gelio milteliai.

Bi–V–O TARTRATO GELIO PIRMTAKO PARUOŠIMAS

Pirmajame Bi–V–O tartrato gelio pirmtakų $5Bi_2O_3 \cdot V_2O_5$ keramikos sintezės etape bismuto (III) oksidas ir vanadžio (V) oksidas buvo ištirpinti koncentruotoje azoto rūgštyje (HNO_3, 66 % Reachem). Labai rūgštiniuose tirpaluose bismutas (III) egzistuoja $[Bi(H_2O)_9]^{3+}$ pavidalu, kuris yra panašus į vandeninius lantanido jonų kompleksus. Dėl dalinės bismuto (III) druskų hidrolizės susidaro bismuto okso klasteriai, kurių tirpumas vandenyje atitinkamai žymiai sumažėja. Taigi, nuolat maišant ir kaitinant apie 80 ºC – 85 ºC temperatūroje, galima ištirpinti Bi_2O_3 koncentruotoje azoto rūgštyje, kaip aprašyta 7 lygtyje.

$$Bi_2O_3 (k) + 6 HNO_3 (aq) + 15 H_2O (s) \rightarrow$$
$$\rightarrow 2 [Bi(H_2O)_9]^{3+} (aq) + 6 NO_3^- (aq) \quad (7)$$
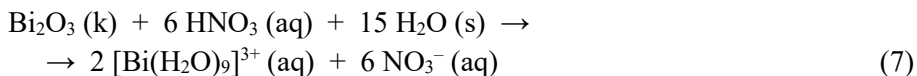
Tuo tarpu vanadžio (V) oksidas yra raudoni milteliai, kurie mažai tirpsta vandenyje, bet stipriai rūgštiniame tirpale sudaro $[VO_2]^+$ kompleksus. Veikiant koncentruota azoto rūgštimi, vanadžio oksido ištirpimas atitinka 8 lygtį.

$$V_2O_5 \text{ (k)} + 2\,HNO_3 \text{ (aq)} \rightarrow 2\,[VO_2]^+ \text{ (aq)} + 2\,NO_3^- \text{ (aq)} + H_2O \text{ (s)} \quad (8)$$
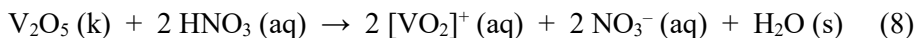
Šis virsmo į $[VO_2]^+$ joną procesas yra gana greitas, o V_2O_5 ištirpinti rūgštiniame vandeniniame tirpale 80 ºC – 85 ºC temperatūroje užtrunka vos keletą minučių. Šviesiai geltono tirpalo susidarymas rodo, kad pervanadilo katijonas yra apsuptas nitratų jonų.

Nitratų jonų koordinavimo geba vandeniniame tirpale yra mažesnė nei atitinkamų vandens ligandų, todėl ištirpus metalų oksidams numatoma arba $(Bi(H_2O)_9)^{3+}$, arba $[VO_2]^+$ kompleksų sudėtis. Didėjant reakcijos mišinio kaitinimo temperatūrai, šie jonai linkę reaguoti vienas su kitu sudarydami mažiau tirpius daugiabranduolius kompleksus, todėl vyno rūgštis, kurios molinis santykis Bi/TA = 0.25 (1 sintezė) ir Bi/TA = 0.125 (2 sintezė), buvo pridėta į reakcijos mišinį nuolat maišant toje pačioje temperatūroje. Toks ligando pridėjimas reikalingas tirpumui padidinti koordinuojant pradinius junginius reakcijos mišinyje, ypač, kai vyksta pH pakitimai ir garavimas prieš zolio-gelio susidarymą.

Pridėjus vyno rūgšties reakcijos mišinio spalva pasikeitė iš šviesiai geltonos į šviesiai žalią. Nuolatinis maišymas ir kaitinimas 80 ºC – 85 ºC temperatūroje vandeninio tirpalo išvaizdą pamažu pakeitė iš žalios į ryškiai mėlyną spalvą. Toks reakcijos mišinio virsmas atitinka metalo katijonų koordinavimą tartratais. Sugertos šviesos bangos ilgio sumažėjimas, kurį rodo tirpalo spalvos pasikeitimas, patvirtina padidėjusį metalo jonų koordinavimo laipsnį su vyno rūgšties liekana.

Po to skaidrus tirpalas koncentruojamas išgarinant reakcijos mišinį 90 ºC temperatūroje. Mėlynas tirpalas palaipsniui pasikeitė į tamsiai žalią skaidrų zolį po to, kai beveik 95% vandens išgaravo nuolat maišant. Galiausiai, išdžiovinus džiovinimo krosnyje 120 ºC temperatūroje, gauti smulkūs raudonai rusvi (1 sintezė) ir ryškiai geltoni (2 sintezė) gelio milteliai.

ĮVAIRIŲ METALŲ TARTRATŲ GELIŲ PIRMTAKŲ TERMINIS APDOROJIMAS

Norint susintetinti galutinius kristalinius junginius, gauti skirtingi metalo gelio pirmtakai buvo papildomai termiškai apdoroti aukštoje temperatūroje.

Pavyzdžiui, norint parodyti kristalų augimo tendenciją, gerai sumaltas Li–Al–Mo–O tartrato gelio pirmtakas buvo termiškai apdorotas 400 ºC, 450 ºC, 500 ºC, 550 ºC, 600 ºC, 650 ºC ir 700 ºC.

Gerai sumalto Li–La–Ti–O tartrato gelio pirmtako terminis apdorojimas buvo atliktas siekiant parodyti gautų miltelių kristalų augimo tendenciją ir padidinti galutinio keramikos kompaktiškumą. Šiuo atveju atitinkamas mėginys buvo termiškai apdorotas 800 ºC, 900 ºC, 1000 ºC ir 1100 ºC oro atmosferoje. Galiausiai gauti keramikos milteliai buvo papildomai termiškai apdoroti 1250 ºC temperatūroje.

Bi–V–O tartrato gelio pirmtakai $5Bi_2O_3 \cdot V_2O_5$ keramikai buvo termiškai apdoroti 5 valandas 800 ºC temperatūroje. Gauti gelsvi keramikos milteliai buvo granuliuoti ir papildomai termiškai apdoroti 870 ºC temperatūroje 5 valandas ore.

PRIETAISAI IR ĮRANGA MĖGINIAMS ANALIZUOTI

Li–Al–Mo–O tartrato gelio pirmtako TG/DSC matavimas buvo atliktas naudojant TG–DSC, STA 6000 Perkin-Elmer prietaisą, naudojant maždaug 5 mg mėginio svorį ir kaitinant 20 °min^{-1} greičiu nuolatiniame oro sraute (20 cm^3/min) esant aplinkos slėgiui nuo kambario temperatūros iki 950 ºC.

Rentgeno spindulių difrakcijos (XRD) modeliai buvo užfiksuoti oro atmosferoje kambario temperatūroje, naudojant miltelinį rentgeno difraktometrą Rigaku MiniFlex II, naudojant Cu Kα spinduliuotę. XRD modeliai buvo registruojami standartiniu 1.5 2θ min^{-1} greičiu. Mėginys buvo paskleistas ant stiklo laikiklio tam, kad būtų pasiektas didžiausias XRD difraktogramų būdingų smailių intensyvumas. Siekiant įvertinti kristalinės fazės sudėtį, gautų XRD modelių Rietveld įvertinimas atliktas naudojant X'Pert HighScore Plus programinę įrangą.

Gautų keramikos mėginių paviršiaus morfologijai ir mikrostruktūrai tirti buvo naudojami skenuojantys elektroniniai mikroskopai (SEM) Hitachi SU-70 ir Hitachi TM3000. $Bi_2O_3 \cdot V_2O_5$ keramikos elementinei sudėčiai nustatyti buvo pritaikyta energijos dispersinė rentgeno spektroskopija (EDS).

Būdingos funkcinių grupių vibracijos visuose termiškai apdorotuose mėginiuose buvo įvertintos naudojant Perkin-Elmer Frontier FTIR spektrometrą.

Elektrinių savybių matavimai buvo atlikti naudojant dvi skirtingas varžos spektroskopijos technologijas naujai sukurtu impedanso spektrometru. Termiškai paveikta keramika buvo apdorota naudojant Pt pastos elektrodus, gauti maždaug 1.5 mm aukščio ir iki 3 mm skersmens cilindriniai pavyzdžiai.

Šiame skyriuje pateikiami susintetintos keramikos analizės rezultatai, kurie aiškiai parodo vandeninio zolių-gelių metodo galimybes.

TERMINIS Li–Al–Mo–O PIRMTAKO SKILIMAS

Terminė analizė buvo panaudota tirti paruošto gelio pirmtako degimo ir pirolizės procesus, kurie atlieka svarbų vaidmenį formuojant galutinę keramiką. Li–Al–Mo–O gelio $LiAlMo_2O_8$ keramikai terminio apdorojimo procesas buvo atliktas oro atmosferoje.

Li-Al-Mo-O tartrato gelio pirmtako skilimą galima apytiksliai suskirstyti į penkis pagrindinius etapus. Pirmasis masės pokytis yra tiesiogiai susijęs su vyno rūgšties pertekliumi. Vyno rūgštis buvo pridėta į reakcijos mišinį tam, kad būtų išvengta nuosėdų iškritimo geliacijos metu. Ši skilimo stadija gerai matoma iš TGA kreivės temperatūrų diapazone nuo 30 ºC iki 320 ºC. Nors susintetintas gelis buvo džiovinamas 120 ºC temperatūroje, vandens molekulės, susidariusios vyno rūgšties dimerų susidarymo metu (9 lygtis), išgaravo iki 125 ºC. Tokį drėgmės pašalinimą iš gelio miltelių galima patvirtinti plačia endotermine juosta DSC kreivėje.

$$\text{(9)}$$
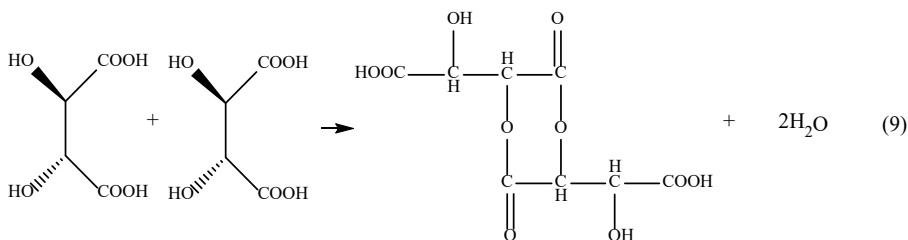
Toliau didėjant temperatūrai, išgaruoja acto rūgštis, kuri susidaro irstant vyno rūgšties dimerui. Šis procesas prasideda apie 130 ºC ir baigiasi 175 ºC temperatūroje. Tai taip pat patvirtina gerai išreikšta endoterminė smailė DSC kreivėje arba aštri juosta TGA kreivėje. Vandenilio keitimas hidroksilo grupe, žinomas kaip Beckmann transformacija, ir susidariusio vyno rūgšties dimero skilimas atitinkamai pateikti 10 lygtyje.

$$(10)$$
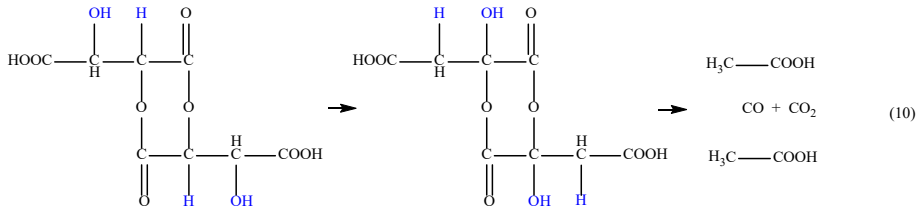
Toliau didinant kaitinimo temperatūrą, susidaręs vyno rūgšties dimeras suyra kitaip. Šis procesas prasideda 200 ºC temperatūroje ir baigiasi aukštesnėje nei 300 ºC temperatūroje. Anglies dioksido išsiskyrimą patvirtina plati egzoterminė juosta DSC kreivėje. Tuo tarpu piruvo rūgšties susidarymo mechanizmas parodytas 11 lygtyje.

$$(11)$$
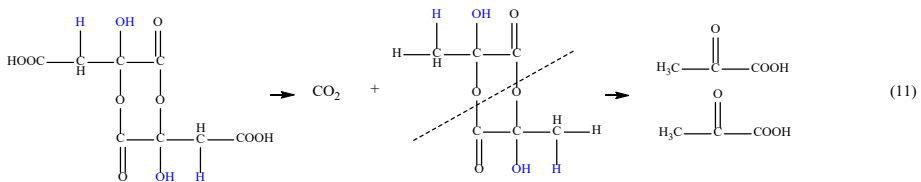
30 ºC – 320 ºC temperatūrų intervale bendras masės pokytis sudaro apie 50%, o tai gerai sutampa su vyno rūgšties kiekiu, kuris buvo pridėtas į reakcijos mišinį reakcijos pradžioje. Tolesnis temperatūros kilimas nuo maždaug 320 ºC iki 500 ºC yra tiesiogiai susijęs su terminiu metalo tartratų skilimu. Tai iš dalies patvirtina mažos ir plačios egzoterminės juostos DSC kreivėje. Taip pat svarbu pažymėti, kad nuo 450 ºC temperatūros DSC kreivėje išskiriamas endoterminis procesas, kuris siejamas su daugiakomponenčių oksidų kristalizacijos pradžia. Temperatūrų intervale nuo 540 ºC iki 679 ºC vykstantis masės pokytis (9.2 %) yra tiesiogiai susijęs su neorganinės anglies, susidariusios dalinio metalo tartratų irimo žemesnėje temperatūroje, degimo procesais. Gelio pirmtako likučio masės padidėjimas temperatūros intervale nuo 679 ºC iki 700 ºC yra siejamas su ličio peroksido susidarymu, kuris sugeria deguonies dujas iš ličio oksido kaip priemaišos fazę. Toliau didinant kaitinimo temperatūrą virš 730 ºC, mėginio masė tampa stabili. Tačiau nuo 850 ºC stebimas gelio likučio masės pokytis, kuris priskiriamas aliuminio molibdato irimui bei molibdeno oksido išgaravimui.

Apibendrinant terminės analizės rezultatus, akivaizdu, kad gautos LiAlMo$_2$O$_8$ keramikos susidarymas labai priklauso nuo pradinių reagentų molinio santykio reakcijos mišinyje. Santykinai žema Al$_2$Mo$_3$O$_{12}$ kristalizacijos temperatūra sudaro sąlygas susidaryti priemaišiniams junginiams, kurių egzistavimą liudija Li–Al–Mo–O tartrato gelio pirmtako

likučio masės padidėjimas apie 679 ºC temperatūroje. Be to, mėginio miltelių masės sumažėjimas virš 850 ºC patvirtina aliuminio molibdato, kaip priemaišos fazės, susidarymą kristaliniame mišinyje.

Li–La–Ti–O TARTRATO GELIO PIROLIZĖ IR DEGINIMAS

Šiame darbe siūloma sintezės technika yra pagrįsta metalų jonų sąveika su vyno rūgštimi vandeninėje terpėje. Vyno rūgštis veikia kaip ligandas geliacijos procese siekiant išvengti nuosėdų susidarymo. Susintetinto Li–La–Ti–O tartrato gelio pirmtakas turi didelę įtaką tiek jo terminio skilimo mechanizmui, tiek galutinio daugiakomponenčio oksido cheminėms ir fizinėms savybėms. Termogravimetrinė ir diferencinė skenuojanti kalorimetrinė analizė leidžia įvertinti tiek ličio lantano titano tartrato gelio skilimo procesą, tiek galutinio daugiakomponentinio oksido kristalizacijos kelią. Todėl šiuo atveju skirtingomis sąlygomis išmatuotos Li–La–Ti–O tartrato gelio pirmtako TG–DTG–DSC kreivės.

Gauti duomenys parodė du svarbius dalykus: organometalinių junginių skilimo mechanizmą ir galutinių keraminių fazių formavimosi ypatumus terminio apdorojimo metu. Be to, mėginių terminis apdorojimas skirtingose atmosferose atskleidė įdomias gelio elgesio tendencijas, ypač esant aukštesnei nei 300 ºC temperatūrai. Gautų gelių terminį skilimą galima apytiksliai suskirstyti į tris pagrindinius etapus.

Kita vertus, priklausomai nuo kaitinimo atmosferos, šiluminio poveikio etapų skaičius gali šiek tiek skirtis dėl organinių junginių degimo, kuris yra labiau skatinamas oru prisodrintoje aplinkoje, o inertinės sąlygos inicijuoja vidinius gelio pirmtako persitvarkymus ir lakiųjų komponentų išgaravimą šiek tiek aukštesnėje temperatūroje. Nepaisant to, pirmajame temperatūrų intervale nuo 30 ºC iki 300 ºC atitinkamų metalų tartratų druskos yra gana stabilios, tačiau nesureagavusios vyno rūgšties skilimas vyko identiškai, nepriklausomai nuo oksidacinės arba inertinės aplinkos.

Toliau kylant temperatūrai, kaitinimo atmosferos įtaka atskleidžia skirtingas atitinkamų metalo tartratų skilimo tendencijas. Iš gautų rezultatų matyti, kad Li–La–Ti–O tartrato gelio pirmtako terminio skilimo proceso panašumas baigiasi esant apie 254 ºC temperatūrai. Egzoterminio proceso pobūdis nuo 253.71 ºC oro atmosferoje ir 254.84 ºC azoto atmosferoje rodo aplinkos sąlygų dominavimo pradžią iki tolesnio pradinio gelio pirmtako irimo. Ši plati egzoterminė terminio skilimo proceso juosta DSC kreivėje konkuruoja su vėlesniu endoterminiu efektu, kuris prasideda atitinkamai 305.80 ºC (N_2 atmosfera) ir 320.79 ºC (oro atmosfera) temperatūroje. Be to,

šis endoterminis procesas persidengia su egzoterminiu pokyčiu, prasidedančiu temperatūros diapazone nuo maždaug 410.68 ºC iki 415.92 ºC, priklausomai nuo kaitinimo atmosferos. Šis pokytis yra susijęs su metalo tartrato likučių intramolekuliniu persitvarkymu Li–Ti–O, La–Ti–O ir Li–La–Ti–O daugiakomponenčių oksidų kristalizacijos pradžia.

Li–La–Ti–O tartrato gelio pirmtako terminis apdorojimas oro atmosferoje nuo 415.92 ºC iki 577.41 ºC sukelia ryškų jo likutinės organinės dalies, kuri yra 5.65 kartus šviesesnė, degimo procesą, nei analogiškas platus egzoterminis efektas, kurį rodo DSC kreivė azoto aplinkoje. Toks stiprus atmosferos dominavimas terminio apdorojimo metu aiškiai rodo, kad galutinė metalo tartrato likučių oksidacija, kuri prasideda 450 ºC temperatūroje, ir jos kitimo mechanizmas labai priklauso nuo aplinkos oksidacinės galios.

Tuo tarpu atitinkamų metalų titanatų kristalizacija vyksta maždaug 500 ºC temperatūroje, tačiau toks pat endoterminis efektas DSC kreivėje Li–La–Ti–O pirmtakui, kuris buvo termiškai apdorotas oro atmosferoje, prasideda kiek vėlesnėje stadijoje, 550 ºC temperatūroje dėl intensyvaus gelio likučių degimo. Be to, remiantis XRD rezultatais ir DSC kreivių tendencijų įvertinimu, ličio lantano titanato kristalizacija paprastai prasideda 550 ºC temperatūroje. Labiausiai tikėtina, kad ryškus paskutinio endoterminio efekto atsiradimas DSC kreivėse, temperatūros diapazone nuo 800 ºC iki 850 ºC, yra priskiriamas ličio lantano titanato likučių kristalizacijos procesui, kaip parodyta 12 lygtyje.

x Li–Ti–O (k) + y La–Ti–O (k) → x Li–yLa–(x + y)Ti–O (k)   (12)
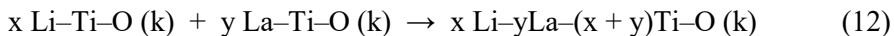
Apibendrinant gautus Li–La–Ti–O tartrato gelio pirmtako terminio skilimo skirtingose kaitinimo atmosferose rezultatus, akivaizdu, kad terminė analizė yra labai naudingas ir reikalingas įrankis, leidžiantis pagrįsti ir paaiškinti galutinių kristalinių oksidų medžiagų susidarymo ypatumus. Šiluminės analizės ir rentgeno spindulių difrakcijos kombinacija suteikia galimybę paaiškinti kristalinių fazių susidarymo priežastis ir pobūdį.

Bi–V–O TARTRATO GELIO PIRMTAKO TERMINIS SKILIMAS

Lakiųjų junginių cheminis stabilumas Bi–V–O tartrato gelio pirmtakuose, paruoštuose zolių-gelių būdu naudojant skirtingą vyno rūgšties kiekį, nustatomas iš TG–DTG–DSC kreivių.

Nepaisant to, kad Bi–V–O gelio pirmtakų šiluminio elgesio tendencijos DSC kreivėje yra panašios, bendras masės pokytis visiškai skiriasi. Mėginys, paruoštas taikant 1 sintezės būdą, geriausiai atitinka 64.6 % masės likutį 800 ºC temperatūroje, jį lyginant su teoriniu atveju (62.1 %). Kito Bi–V–O gelio pirmtako (2 sintezės) galutinis skilimas sudaro 68.9 % likusios masės ir visiškai neatitinka teorinio masės pokyčio, dėl kurio susidaro ne mažiau kaip 29.0 % keramikos likučių. Toks skirtumas paaiškinamas stabilių metalų karbonatų arba atitinkamų anglies pagrindu pagamintų junginių, įstrigusių Bi–V–O tinkle, susidarymu garinimo ir terminio apdorojimo metu. Šios keraminės sistemos išlieka stabilios net aukštesnėje nei 800 ºC temperatūroje.

Kaip žinoma iš ankstesnių tyrimų, vyno rūgšties terminis skilimas vyksta iki 300 ºC temperatūros. Nepaisant to, kad vyno rūgšties kiekis pagal sintezės būdą skiriasi du kartus, masės pokytis abiem atvejais buvo beveik vienodas. Šis rezultatas rodo, kad padidėjęs vyno rūgšties kiekis 2 sintezėje stipriai veikia Bi–V–O sistemą geliacijos proceso metu. Atitinkamų gelio pirmtakų spalvos pokytis patvirtina šią išvadą, o stiprus DSC kreivės endoterminis pobūdis ($\Delta H=45.581$ J g^{-1}) ir masės pokytis, kuris yra apie 5%, patvirtina padidėjusį atitinkamo gelio pirmtako hidrataciją.

Tolesnis terminis apdorojimas temperatūrų intervale nuo 100 ºC iki 200 ºC lemia ir didesnį, apie 10%, masės pokytį gelio pirmtakui, gautame 1 sintezėje. Tuo tarpu 2 sintezės atveju masės pokytis sumažėja tik 2%. Didžiausias Bi–V–O tartrato gelio pirmtako (2 sintezės) masės pokytis stebimas temperatūros intervale nuo 220 ºC iki 300 ºC, kai masė sumažėja apie 25%. Toks skirtingas abiejų TG kreivių elgesys temperatūros intervale nuo 30 ºC iki 300 ºC rodo nevienodą tartratų koordinuojamos Bi–V–O sistemos įtaką vyno rūgšties, kuri liko nesureagavusi reakcijos mišinyje, stabilumui. Tolesnis temperatūros kilimas nuo 300 ºC iki 470 ºC rodo tipišką 1 sintezės metalų tartratų skilimą, kuomet masė sumažėjo apie 5.428%. 2 sintezės atveju masės pokytis buvo tik apie 1.5%. Toks santykinai mažas tartratų kiekis Bi–V–O tartrato gelio pirmtakuose šiai sintezės metodikai yra nebūdingas ir tai galima paaiškinti tik stabilių metalo-anglies-deguonies junginių susidarymu, kurie nesuyra net aukštesnėse temperatūrose.

Paskutinis masės pokytis temperatūros intervale nuo 470 ºC iki 540 ºC atitinka tartratų likučių skilimą. Apie 4.049 % (1 sintezė) ir 2.198 % (2 sintezė)

masės pokyčiai sutampa su metalo tartratų masės praradimo reikšmėmis temperatūros intervale nuo 300 ºC iki 470 ºC. Visa tai parodo, kad vyno rūgšties kiekis yra svarbus Bi-V-O tartrato gelio pirmtakų formavimosi metu.

Tuo remiantis, galima teigti, jog vyno rūgšties trūkumas zolių-gelių proceso metu sukuria nuosėdas, kurios stipriai veikia galutinio gelio pirmtako homogeniškumą. Tuo tarpu dėl ligando pertekliaus susidaro nemažas kiekis Bi–V–O keramikos, integruotos su anglies pagrindo priemaišomis, kurios išlaiko savo stabilumą net aukštesnėje nei 815 ºC temperatūroje.

RENTGENO SPINDULIŲ DIFRAKCIJOS MODELIAI

Rentgeno spindulių difrakcinė analizė (XRD) – neardomasis kristalinių struktūrų tyrimo metodas, kuriuo galima apibūdinti medžiagos kristalinę struktūrą, nustatyti cheminius junginius ir jų rūšis bei defektus, apskaičiuoti kristalitų dydžius. Šiame darbe XRD metodas yra sėkmingai derinamas su sintetintų gelių termine analize. Kristalinių fazių sudėtis mėginyje leidžia patvirtinti kristalizacijos procesus, vykstančius terminio apdorojimo metu.

$LiAlMo_2O_8$ KERAMIKOS KRISTALITŲ AUGIMO TENDENCIJOS

Šiame darbe atlikti Li–Al–Mo–O tartrato gelio pirmtako XRD tyrimai $LiAlMo_2O_8$ pradinės sudėties keramikai, termiškai apdorotai skirtingomis temperatūromis.

Gautos keramikos fazių sudėtis ir kristalitų dydžių įvertinimas buvo nustatytas Rietveldo analize. Susintetinto gelio pirmtako homogeniškumas buvo įrodytas difraktograma, kurioje nebuvo jokių smailių, būdingų kristaliniams junginiams. Kaip matyti iš terminės analizės rezultatų, po vyno rūgšties pertekliaus skilimo procesų yra išskiriama kristalinių junginių kristalizacijos pradžia. Žinant, kad aliuminio molibdatas pradeda formuotis aukštesnėje nei 400 ºC temperatūroje, termiškai apdorojant mėginį 450 ºC temperatūroje susidaro mažiausiai dvi skirtingos kristalinės fazės. Nepaisant to, likusių Li–Al–Mo–O gelio pirmtako, termiškai apdoroto aukštesnėje temperatūroje, kristalinių fazių sudėtis rodo triklininio $LiAlMo_2O_8$ junginio dominavimą, kurio kiekis linkęs didėti didinant terminio apdorojimo temperatūrą.

Kristalitų dydis eksponentiškai didėja nuo 36.75 nm bandinyje, termiškai apdorotame 500 ºC temperatūroje, iki 126.11 nm esant 700 ºC temperatūrai. Priemaišos $Al_2Mo_3O_{12}$ kristalinės fazės egzistavimas patvirtina išvadas, gautas analizuojant terminės analizės rezultatus – esant didesnei nei 900 ºC

temperatūrai, pastebėtas bandinio masės sumažėjimas, kuris yra susijęs su aliuminio molibdato skilimu ir MoO_3 pašalinimu iš reakcijos mišinio.

Apibendrinant XRD difraktogramų rezultatus, galima daryti išvadą, kad galutinių kristalinių fazių sudėtis reakcijos mišinyje labai priklauso nuo pradinių reagentų molinės sudėties. Terminio apdorojimo temperatūros padidėjimas sumažina priemaišų fazių skaičių reakcijos mišinyje, tačiau vienfazio $LiAlMo_2O_8$ junginio sintezė žemesnėje temperatūroje išlieka sudėtinga.

KRISTALINIŲ LLTO FAZIŲ RENTGENO DIFRAKCIJOS TYRIMAI

Šiame darbe taip pat buvo atlikti Li–La–Ti–O tartrato gelio pirmtako XRD tyrimai $Li_{0.35}La_{0.55}TiO_3$ pradinės sudėties keramikai, termiškai apdorotai skirtingomis temperatūromis.

Iš XRD modelių aiškiai matyti, kad terminio apdorojimo temperatūrą padidinus iki 1000 ºC, visiškai išnyko būdingos smailės, priskirtinos priemaišų kristalinėms fazėms. Apskaičiuota, kad $Li_{0.3}La_{0.567}TiO_3$ keramikos tetragoninės kristalinės fazės kristalitų dydis padidėjo nuo 61.48 nm iki 97.71 nm. Šiame terminio apdorojimo etape ličio ir lantano titanatų likučiai reaguoja su lantano karbidu. Atitinkamos kompozicijos smailės buvo sėkmingai nustatytos Rietveldo analize.

Titano trūkumą kristalinių junginių mišinyje galima kompensuoti titano oksidu. Nedidelis TiO_2 kiekis identifikuotas mėginio, kuris buvo termiškai apdorotas 800 ºC temperatūroje, rentgenogramoje. Šiuo atveju smailės, priskiriamos kristaliniam titano oksidui, persikloja su jau nustatytomis smailėmis, priskiriamomis ličio ir lantano titanatams. Svarbu pažymėti, kad mėginį termiškai apdorojus aukštesnėje nei 1000 ºC temperatūroje, buvo stebimas laipsniškas vienfazio $Li_{0.3}La_{0.567}TiO_3$ trikomponenčio oksido virsmas į $Li_{0.,35}La_{0.55}TiO_3$ kristalinę fazę.

Tokiais atvejais gautą keramiką daugiausia sudaro ortorombinė $Li_{0.35}La_{0.55}TiO_3$ fazė, kurios masės dalis mišinyje sudaro 91.3%

Nustatytame mišinyje ličio ir lantano molinis santykis (n(Li)/n(La)=0.648) yra artimas $Li_{0.35}La_{0.55}TiO_3$ keramikos molinei sudėčiai. Ličio jonų perteklius (x=0.67) yra pašalinamas iš oksidų mišinio perkristalizuojant galutinį kristalinį junginį 1250 ºC temperatūroje. Iš šio rezultato aišku, kad $Li_{0.35}La_{0.55}TiO_3$ keramikos cheminių elementų santykį kontroliuoja joje esantis lantano kiekis.

Papildomai termiškai apdorojant gautą keramiką 1250 ºC temperatūroje 5 valandas oro atmosferoje, buvo gautas vienfazis $Li_{0.35}La_{0.55}TiO_3$ sudėties

oksidas, kuriame apskaičiuotas kristalitų dydis atitinka 110.64 nm. Apibendrinant XRD rezultatus, akivaizdu, kad galutinė ličio lantano titanato keramika pradeda formuotis esant gana aukštai, aukštesnei nei 500 °C temperatūrai. Šiuo atveju pradinė ličio titanato tarpinio produkto kristalizacija leidžia sumažinti ličio jonų lakumą, ypač temperatūros intervale nuo 500 °C iki 1000 °C. Tuo tarpu papildomas tabletės (presuotos iš miltelių, termiškai apdorotų 1 000 °C temperatūroje) terminis apdorojimas 1250 °C temperatūroje didelio masės pokyčio nesukelia, o tai leidžia manyti, kad galimas ličio jonų perteklius yra pašalinamas iš susintetintos oksidų sistemos po pakartotinio ilgalaikio kaitinimo, kai buvo nustatytas galutinis daugiakomponentis oksidas, turintis $Li_{0.35}La_{0.55}TiO_3$ sudėtį.

Teisingas galutinio $Li_{0.35}La_{0.55}TiO_3$ keramikos pradinės stechiometrijos pasirinkimas buvo iš dalies patvirtintas $Li_{3x}La_{2/3-x}TiO_3$ (x=0.10, 0.12, 0.14 ir 0.16) mėginių, termiškai apdorotų 1000 °C temperatūroje XRD rezultatais.

Remiantis Rietveldo analizės rezultatais, buvo nustatytas $Li_{0.3}La_{0.567}TiO_3$ keramikos tetragoninės kristalinės fazės dominavimas, tačiau pastebėta ir ortorombinės kristalinės fazės kiekio didėjimo tendencija $Li_{0.35}La_{0.55}TiO_3$ junginiui. Tai rodo, kad pradinis ličio ir lantano molinis santykis yra svarbus parametras, lemiantis atitinkamo ličio lantano titanato kristalinės sudėties susidarymą aukštesnėje temperatūroje.

LLTO KRISTALINIŲ FAZIŲ STRUKTŪRINĖ ANALIZĖ

Kaip buvo nustatyta iš XRD modelių, pradinis Li/La atomų molinis santykis yra svarbus parametras, įtakojantis galutinės kristalinės fazės formavimąsi. Bendrą informaciją apie atitinkamų junginių kristalinę struktūrą galima sėkmingai gauti iš tolerancijos koeficiento (t) reikšmių. Šis parametras parodo Goldschmidt pateiktą tarpusavyje besiskverbiančių dodekaedrų ir oktaedrų išdėstymo ABO_3 perovskito struktūroje koncepciją, kurią pateikia 13 lygtis:

$$t = \frac{R_a + R_o}{(2)^{1/2}(R_b + R_o)} \qquad (13)$$

kur R_a, R_b ir R_o yra atitinkamai katijono A, B ir deguonies joniniai spinduliai. Sudėtingoje perovskito sistemoje R_a ir R_b yra sudarytų jonų joniniai spinduliai, normalizuoti pagal atominį santykį .

Perovskito struktūra yra stabili srityje 0.880 < t < 1.090, o simetrija yra tuo didesnė, kuo t vertė yra arčiau 1. Reikšmė t taip pat rodo, kiek toli atomai gali

pasislinkti nuo idealių pakavimo padėčių ir vis dar būti „toleruojami" perovskito struktūroje. Tai atspindi struktūrinius pokyčius, tokius kaip oktaedro iškraipymas, sukimasis, posvyris.

Panašios išvados buvo padarytos iš oktaedrų tempimo, kampinių ir sukimo iškraipymų ABO_3 perovskito struktūroje $Li_{0.3}La_{0.567}TiO_3$ ir $Li_{0.35}La_{0.55}TiO_3$ keramikai. ζ ir Σ yra bendri metalo jonų komplekso nuokrypiai nuo idealios oktaedrinės struktūros, o Θ reiškia iškraipymą nuo tobulos oktaedrinės (O_h) iki trigonalinės prizminės (D_{3h}) geometrijos. ζ, Σ ir Θ parametrų matematinės išraiškos pateikiamos tokiomis lygtimis:

$$\zeta = \sum_{i=1}^{6} |d_i - d_{mean}| \qquad (14)$$

$$\Delta = \frac{1}{6} \sum_{i=1}^{6} \left(\frac{d_i - d}{d}\right)^2 \qquad (15)$$

$$\Sigma = \sum_{i=1}^{12} |\phi_i - 90| \qquad (16)$$

$$\Theta = \sum_{i=1}^{24} |\theta_i - 60| \qquad (17)$$

Tempimo iškraipymo parametro Δ reikšmė turi tą pačią reikšmę kaip ζ, bet nepriklauso nuo cheminės jungties ilgio matavimo vienetų. ζ, Δ, Σ ir Θ parametrų struktūriniai duomenys pateikti atitinkamai 6 – 9 lentelėse 3.2.3 skyriuje.

Tetragoninės kristalinės fazės iškraipymo parametrų reikšmės yra didesnės nei ortorombinės struktūros. Šis rezultatas gerai koreliuoja su atitinkamų kompozicijų tolerancijos koeficientu.

$Bi_{23}V_4O_{44}$ JUNGINIO KRISTALIZACIJA IŠ $5Bi_2O_3 \cdot V_2O_5$ MIŠINIO

Siekiant patvirtinti kristalinę sudėtį termiškai apdorotuose Bi–V–O gelio pirmtakuose $5Bi_2O_3 \cdot V_2O_5$ keramikai buvo atlikta rentgeno difrakcija (XRD). Abiejų Bi–V–O tartrato gelio pirmtakų, termiškai apdorotų 870 ºC temperatūroje, XRD duomenys atitinka būdingus atspindžius, kurie priskiriami ortorombinei $Bi_{23}V_4O_{44}$ sistemų kristalų struktūrai.

Atitinkamų mėginių Rietveldo patikslinimo analizė patvirtino ortorombinio $Bi_{23}V_4O_{44}$ (ICSD Nr.: 418368) kristalinio junginio dominavimą.

Taip pat buvo nustatytos monoklininės $Bi_{46}V_8O_{89}$ (ICSD Nr.: 415113) ir triklininės $Bi_{46}V_8O_{89}$ (ICSD Nr.: 87271) sistemų fazės pėdsakų. Pagal šį rezultatą akivaizdu, kad pradinė $5Bi_2O_3 \cdot V_2O_5$ sudėtis gerai atitinka gautas kristalines fazes.

Taip pat svarbu pažymėti, kad panašios kristalizacijos tendencijos buvo stebimos gelio pirmtakams, paruoštiems 1 sintezės metu ir termiškai apdorotiems 800 °C temperatūroje. Toks rezultatas yra glaudžiai susijęs su paruošto Bi–V–O tartrato gelio pirmtako homogeniškumu, kurį patvirtino XRD modelio amorfinis pobūdis.

PAVIRŠIAUS MIKROSTRUKTŪROS TYRIMAS SEM METODU

Metalų tartratų gelio pirmtakų paviršiaus morfologija atitinkamoms keraminėms medžiagoms, susintetintoms vandeniniu zolių-gelių metodu ir termiškai apdorotoms skirtingomis temperatūromis, buvo ištirta naudojant skenuojančią elektroninę mikroskopiją (SEM). Šis analizės metodas tinka medžiagos paviršiaus morfologijai tirti dėl žymiai didesnės skiriamosios gebos ir vaizdo raiškumo lyginant su optiniu mikroskopu.

TEMPERATŪROS POVEIKIS Li–Al–Mo–O TARTRATO GELIO PIRMTAKO PAVIRŠIAUS MORFOLOGIJAI

Siekiant parodyti gautos keramikos dalelių augimo tendenciją didinant terminio apdorojimo temperatūrą, buvo ištirta jų paviršiaus morfologija. Li–Al–Mo–O tartrato gelio pirmtako, termiškai apdoroto 400 °C, 500 °C, 600 °C ir 700 °C temperatūroje, SEM nuotraukos pateiktos 3.3.1 skyriuje. Mėginio, termiškai apdoroto 400 °C temperatūroje, bandinio paviršius yra vienalytis, susidedantis iš netaisyklingų formų darinių, susidariusių irstant nesureagavusiai vyno rūgščiai. Šis rezultatas gerai sutampa su XRD duomenimis, kai galutinės keramikos susidarymas 400 °C temperatūroje nebuvo aiškiai išreikštas. Mėginio terminio apdorojimo temperatūros padidėjimas iki 500 °C parodo paviršiaus morfologijos pokyčius, susijusius su mažesnių nei 200 nm dydžio sferinių dalelių augimo pradžia. Beveik identiškas vaizdas stebimas ir 600 °C temperatūroje – išskiriamas gerai matomas smulkesnių dalelių susibūrimas į didelius agregatus. Termiškai apdorojant mėginį 700 °C temperatūroje, susidaro taisyklingos formos dalelės su aiškiai apibrėžtais kraštais, kurių dydis svyruoja nuo 4 µm iki 10 µm.

SEM rezultatai rodo, kad galutinės keramikos dalelių augimas vyksta dvejais etapais. Pirmajame etape išskiriamas kristalitų, kurių skersmuo

neviršija 100 nm, aglomeratų susidarymas. Tuo tarpu, esant aukštesnei nei 600 ºC temperatūrai, susidariusios dalelės pradeda jungtis į 4 μm - 10 μm dydžio darinius, turinčius taisyklingą struktūrą, aiškias plokštumas ir gerai išreikštus kraštus. Remiantis XRD analizės rezultatais, galima daryti išvadą, kad taisyklingos formos dalelės daugiausia susideda iš kristalitų, kurių vidutinis dydis atitinka 126.11 nm vertę.

TANKIOS STRUKTŪROS FORMAVIMAS LLTO KERAMIKOJE

Pirminis koreliacijos tarp SEM rezultatų ir XRD duomenų nebuvimas rodo, kad gautos dalelės ant tabletės paviršiaus yra sudarytos iš glaudžiai supakuotų kristalitų. Nepaisant tolygios dalelių formos ir aiškiai apibrėžtų kraštų, platus dydžių pasiskirstymas rodo, kad kristalitų parametrai yra mažesni nei atitinkamų dalelių tabletės paviršiuje, o tai puikiai dera su XRD rezultatais.

Susintetinto $Li_{0.35}La_{0.55}TiO_3$ kristalinio junginio, kuris buvo termiškai apdorotas 1250 ºC temperatūroje 5 valandas oro atmosferoje, paviršiaus morfologija susideda iš taisyklingos formos dalelių, kurios dydis svyruoja nuo 1 μm iki 10 μm. Be to, reikia paminėti, kad tabletės viduje, lūžio vietoje, buvo nustatytas tankus susintetintų kristalitų susikaupimas monolitiniame paviršiuje be gerai matomų įtrūkimų ir ertmių.

Žinant tai, kad glaudžiai išsidėstę kristalitai ir tanki vienkristalinio daugiakomponentinio oksido struktūra smarkiai pagerina gauto mėginio laidumo savybes, galima teikti, kad atskirų dalelių dydis gali turėti įtakos grūdelių ribinių verčių laidumo sumažėjimui, ypač esant žemai temperatūrai, kai ličio jonų mobilumas yra palyginti mažas.

SEM IR EDS ANALIZĖS $5Bi_2O_3 \cdot V_2O_5$ KERAMIKAI

Paviršiaus morfologinės savybės, kurios turi didelę įtaką sintezuotos keramikos elektrinėms savybėms, taip pat buvo tiriamos skenuojančia elektronine mikroskopija (SEM). SEM nuotraukos Bi-V-O tartrato gelio prekursoriui, kaitintame 870 ºC temperatūroje, yra pateiktos 3.3.3 skyriuje.

Pirmosios nuotraukos (Bi-V-O tartrato gelis, paruoštas pirmosios sintezės būdu) rezultatai rodo, jog mėginio paviršius yra tankus, be įtrūkimų ir ertmių. Padidinus SEM vaizdą, matosi, kad dalelės susijungia su iš dalies ištirpusia medžiaga, o tai padidina keramikos kietumą ir mechaninį stiprumą. Šiek tiek kitoks $5Bi_2O_3 \cdot V_2O_5$ keramikos (Bi-V-O tartrato gelis, paruoštas antrosios sintezės būdu) SEM nuotraukuose matomas vaizdas, kur paviršių daugiausia

sudaro masyvūs monolitai su aštriais kraštais ir mažomis ertmėmis, kurių skersmuo skiriasi nuo 500 nm iki 3 μm.

Be abiejų mėginių morfologinių ypatumų, pažymėtina ir tai, kad mechaninis apdorojimas, kuris buvo pritaikytas įterpiant jį į zondą varžos analizei, kardinaliai skyrėsi. Mechaninis $5Bi_2O_3 \cdot V_2O_5$ keramikos apdorojimas, paruoštas naudojant 1 sintezę, buvo lengvai valdomas, todėl buvo gauta norima forma ir matmenys su lygiu bandinio paviršiumi. Tačiau kito pavyzdžio paruošimas buvo daug sudėtingesnis dėl įtrūkimų susidarymo ir lengvo trupėjimo.

Gauti rezultatai atskleidė, kad mažesnis vyno rūgšties kiekis zolių-gelių proceso metu pirmoje sintezėje lemia bismuto (10.996) ir vanadžio (2.000) molinį santykį, artimą tiek pradiniam elementų kiekiui ($5Bi_2O_3 \cdot V_2O_5$), tiek kristalinio junginio $Bi_{23}V_4O_{44}$ kompozicijai, kuris buvo priskirtas pagal XRD duomenis. Padidėjęs deguonies atomų kiekis mėginyje gali būti paaiškintas tiek organinėmis priemaišomis, ypač esant žemai temperatūrai, tiek nestechiometrija kristalų oksiduose arba amorfinėse fazėse termiškai apdorotame mėginyje 870 ºC temperatūroje.

Bismuto ir vanadžio molinis santykis antrojoje sintezėje išliko panašus, nepaisant terminio apdorojimo temperatūros. Toks rezultatas puikiai sutampa su terminės analizės išvada apie padidėjusio vyno rūgšties kiekio įtaką keramikos sudėčiai.

FT-IR TYRIMAI $LiLaMo_2O_8$ KERAMIKAI

Paprastai neorganinių medžiagų infraraudonųjų spindulių juostos yra platesnės, jų yra mažiau ir jų bangų skaičius yra mažesnis nei organinių medžiagų. Nepaisant to, mėginio, termiškai apdoroto 400 ºC temperatūroje, FT-IR spektre matoma plati juosta su silpnai išreikštomis smailėmis nuo 1600 cm^{-1} iki 1050 cm^{-1} yra siejama su atitinkamų tartratų cheminių ryšių būdingomis vibracijomis. Šiuo atveju smailė ties 1589 cm^{-1} atitinka –COO funkcinės grupės asimetrinį tempimą. Tuo tarpu smailės padėtis esant 1380 cm^{-1} apibūdina arba –OH lenkimą plokštumoje, arba –COO simetrinį tempimą. Smailės, atitinkančios 1256 cm^{-1}, 1121 cm^{-1} ir 1074 cm^{-1} reikšmes, priskiriamos C–H tempimui plokštumoje, C–OH ir CH–OH tempimui. Santykinai mažas smailių, priskiriamų organiniams junginiams, intensyvumas gali būti paaiškintas visišku vyno rūgšties skilimu ir susidariusių lakiųjų komponentų išgaravimu bei iš dalies suirusių metalų tartratų egzistavimu.

Didinant terminio apdorojimo temperatūrą, organinių junginių smailės nuo 1600 cm^{-1} iki 1050 cm^{-1} linkusios išnykti. Tuo tarpu naujai suformuotos

charakteringos smailės, nustatytos bangų skaičiaus diapazone nuo 1000 cm^{-1} iki 500 cm^{-1}, atitinka metalo ir deguonies jungties virpesius. Šiuo atveju smailės, priskiriamos ~957 cm^{-1} ir ~935 cm^{-1} bangos skaičiams, atitinka būdingus simetrinio MoO_4 tetraedro virpesius. Tuo tarpu trigubai išsigimęs (v3) F2 simetrijos režimas vas (MoO_4) ir v (Mo_2O_2) tilto virpesiams atitinka smailes ties ~916 cm^{-1}, ~846 cm^{-1}, ~765 cm^{-1} ir ~693 cm^{-1}.

Smailių intensyvumas, plotis ir forma nuo 1000 cm^{-1} iki 500 cm^{-1} priklauso nuo keramikos pirmtako kristališkumo laipsnio, paviršiaus ploto ir kristalų struktūros. Didinant terminio apdorojimo temperatūrą, didėja ir kristalinių junginių kristališkumas. Tuo tarpu, kai kristalitai ir dalelės yra linkę augti, o paviršiaus plotas turi tendenciją mažėti, pastebimas priešingas poveikis. Tai yra pagrindinė priežastis, lemianti 700 ºC temperatūroje termiškai apdoroto gelio pirmtako būdingų smailių intensyvumo mažėjimą.

LLTO KERAMIKOS ELEKTRINIO LAIDUMO SAVYBĖS

Ličio jonų joninis laidumas Li–La–Ti–O sistemoje labai priklauso nuo trikomponenčio oksido junginio kristalinės struktūros. Tūrinio laidumo mechanizmą tetragoninei $Li_{3x}La_{1.33-x}Ti_2O_6$ sistemai (P4/mmm) pasiūlė Ruiz ir kt., kuris atitinka parabolinę x funkciją su didžiausia Li^+ reikšme, kurios kiekis lygus 0.25, kaip pasiūlė Inaguma ir kt. Inaguma ir kt. taip pat pasiūlė joninį mechanizmą Li-turtingai $Li_{3x}La_{2/3-x}TiO_3$, krosnyje aušinamai $Li_{0.35}La_{0.55}TiO_3$ sistemai. Manoma, kad TiO_6 oktaedrų pakreipimas ir La tvarka lemia greitesnį ličio jonų laidumą La-skurdžiame sluoksnyje nei La turtingame sluoksnyje ir kontroliuoja perkoliatyvinį difuzijos kelią nuo dvimačio iki beveik trijų dimensijų. Didėjant terminio apdorojimo temperatūrai, keičiasi ir ličio jonų lakumas. Šis poveikis turi įtakos tiek Li/La jonų santykiui, tiek kristalų fazių sudėčiai oksido mišinyje. Tokiomis aplinkybėmis ličio lantano titanato kristalinės fazės dominavimas taip pat linkęs keistis. Priklausomai nuo elementų skaičiaus tokioje multisistemoje, nenutrūkstama rekristalizacija vyksta esant santykinai aukštai temperatūrai, todėl kristalitų dydis reikšmingai nedidėja, kartais net linkęs mažėti, o dažniausiai neviršija 110 nm. Tai yra pagrindinė priežastis, kodėl tokioje daugiakomponentėje oksidų sistemoje padidėjęs tarpgranulinis atsparumas yra santykinai didelis ir sumažina bendrą joninį laidumą, ypač esant žemai temperatūrai. Norint patvirtinti šiuos teiginius ir naudojant ankstesniuose skyriuose pateiktą informaciją, šiame darbe buvo įvertintos ir gautos $La_{0.55}Li_{0.35}TiO_3$ keramikos joninio laidumo reikšmės.

Tuo tarpu grūdelių ribos varža yra santykinai didelė, todėl labai sumažėja susidarančios Li–La–Ti–O sistemos bendras joninis laidumas. Šis rezultatas patvirtina prielaidą, kad kristalitų, kurių dydžiai išlieka nanometrinėje skalėje, susidarymas priveda prie santykinai žemo bendras laidumo 27 ℃ temperatūroje. Taip pat reikėtų pažymėti, kad grūdelių ribos laidumas didėja tiesiškai didėjant temperatūrai, tačiau tūrinio laidumo priklausomybė nuo temperatūros yra eksponentinė. Tai galima paaiškinti skirtingu ličio jonų laidumu kristalituose ir grūdelių ribose. Galima teigti, kad didelis tarpkristalinės erdvės plotas iškreipia grūdelių ribos laidumo reikšmių priklausomybę nuo temperatūros ir sudaro palankias sąlygas jai dominuoti. Šį poveikį daugiausia lemia kristalitų dydis Li–La–Ti–O sistemoje. Iš tokių rezultatų tikėtina, kad didesni kristalitai padidintų bendrą Li–La–Ti–O sistemos laidumą net nekeičiant elementų santykio sintezės metu. Be to, grūdelių ribos laidumo sumažėjimas aukštesnėje temperatūroje yra tiesiogiai susijęs su daliniu fazės perėjimu iš ortorombinės į tetragoninę fazę ir cheminių ryšių iškraipymu atitinkamoje kristalinėje struktūroje.

$5Bi_2O_3 \cdot V_2O_5$ SISTEMOS ELEKTRINIS LAIDUMAS

Terminis Bi–V–O tartrato gelio pirmtakų skaidymas ir detalus $5Bi_2O_3 \cdot V_2O_5$ medžiagų charakterizavimas atskleidė, kad vyno rūgšties kiekis terminio apdorojimo metu turi didžiulę įtaką tiek galutinei gautos keramikos sudėčiai, tiek paviršiaus morfologijos ypatybėms. Atsižvelgiant į tai, kad tik $5Bi_2O_3 \cdot V_2O_5$ junginiui (paruoštam pirmos sintezės būdu) pavyko suformuoti stabilių matmenų mėginį, laidumo matavimai atlikti tik šiam bandiniui. Atitinkama laidumo priklausomybė nuo temperatūros buvo įrodyta iš Arrhenius diagramų σ v/s $f(10^3/T)$. Pirmojo vėsinimo (350 ℃ – 110 ℃) ir antrojo šildymo (110 ℃ – 350 ℃) etapų vaizdavimas sutampa, todėl 3.6 skyriuje pateiktas tik antrojo šildymo vaizdavimas. $5Bi_2O_3 \cdot V_2O_5$ keramika rodo Arrhenius tipo elektrinio laidumo elgseną, t.y. linijinę priklausomybę nuo temperatūros visame tiriamame diapazone. Apskaičiuota aktyvavimo energija (E_a) yra lygi 0.93 eV visų rūšių laidumui.

Verta paminėti, kad gautos bendrojo laidumo (σ_{total}) reikšmės esant 330 ℃ temperatūrai yra panašios lyginant su sistemomis $Pb_{10}Bi_{36}V_8O_{84}$, $Sr_{10}Bi_{36}V_8O_{84}$, $Ca_{10}Bi_{36}V_8O_{84}$, $Cd_{10}Bi_{36}V_8O_{201}$ ir $Bi_4V_8O_{201}$ esant 800 ℃ temperatūrai. Taigi, pasirinkta sintezės technika greičiausiai nulemia gautos keramikos išskirtinumą tiek struktūriniu, tiek kompoziciniu aspektu.

IŠVADOS

1. Vandeninis zolių-gelių sintezės metodas yra tinkamas gauti $LiAlMo_2O_8$, $Li_{0,35}La_{0,55}TiO_3$ vienfazes kristalines kompozicijos fazes ir $5Bi_2O_3 \cdot V_2O_5$ vienfazę kristalines kompozicijos fazę su nedidelėmis priemaišomis.

2. Gauti homogeniški Li–Al–Mo–O, Li–La–Ti–O ir Bi–V–O tartrato geliai yra sudaryti iš vyno rūgšties ir metalo tartratų mišinio.

3. Vyno rūgšties skilimo procesas vyksta 30 ºC – 320 ºC temperatūrų intervale, kurio mechanizmas yra detaliai aprašytas ir patvirtintas specifinėmis TGA ir DSC masės kitimo ir šiluminių transformacijų charakteristikomis.

4. Kristalinių fazių susidarymui didžiausią įtaką turi galutinė kaitinimo temperatūra (Li-Al-Mo-O atveju) ir atskirų elementų molinis santykis galutiniame gelio pirmtake (Li-La-Ti-O) atveju.

5. Didžiausią įtaką gautos keramikos paviršiaus morfologijai ir porų ar įtrūkimų susidarymui turi galutinė temperatūra ir keramikos paruošimo kaitinimui būdas.

GYVENIMO APRAŠYMAS

CURRICULUM VITAE

Asmeninė informacija	
Vardas, pavardė	Austėja Diktanaitė
Gimimo data	1992-09-28
Adresas	Gilužio g. 43-15, Vilnius
Telefono numeris	+37064899589
El. pašto adresas	austeja.diktanaite@gmail.com

Išsilavinimas ir kvalifikacija	
2011 – 2015	Nanotechnologijų ir medžiagotyros bakalauro kvalifikacinis laipsnis, Vilniaus universitetas
2016 – 2017	Biotechnologijų magistro kvalifikacinis laipsnis, Heriot-Watt University

Darbo patirtis		
2014-06 – 2014-11	Micronit Microfluidics BV	Mokslininkė praktikantė
2017-10 – 2019-04	Thermo Fisher Scientific Baltics	Jaunesnioji biotechnologė
2019-04 – 2019 07	Thermo Fisher Scientific Baltics	Biotechnologė
2019-07 – 2021-04	Thermo Fisher Scientific Baltics	Kapiliarinės elektrofozerės grupės vadovė
2021-04 – 2021-05	Northway Biotech	Stabilumo tyrimų grupės vadovė
2021-05 – 2021 08	Northway Biotech	Fizikocheminių metodų sektoriaus vadovė

ACKNOWLEDGEMENTS

I would like to extend my uttermost gratitude and profound appreciation to my supervisor **Dr. Artūras Žalga** for their exceptional guidance and support throughout the process of completing this dissertation. Their unconditional support, expert knowledge, and insightful feedback have been indispensable in shaping the outcome of this research. Without their presence and guidance, this work would not have reached its completion.

Additionally, I am immensely grateful to my colleagues who worked together on the articles that contributed to this research. Their collaborative spirit, dedication, and insightful notes have been invaluable, and I am very thankful for their shared efforts.

Finally, I would like to express my gratitude to my cherished family and friends. Their encouragement, patience, and belief in me have been instrumental in reaching this significant milestone.

LIST OF PUBLICATIONS

Articles in journals included in this thesis

I. Artūras Žalga, **Austėja Diktanaitė**, Giedrė Gaidamavičienė, Aqueous sol–gel synthesis, thermoanalytical, structural and vibrational studies of lithium aluminium molybdate (LiAlMo$_2$O$_8$). *Chemija* Vol. **33**. No. 4. (2022) 103-109. *doi: https://doi.org/*10.6001/chemija.v33i4.4806

II. **Austėja Diktanaitė**, Giedrė Gaidamavičienė, Edvardas Kazakevičius, Algimantas Kežionis, Artūras Žalga, Aqueous sol-gel synthesis, structural, thermoanalytical studies, and conductivity properties of lithium lanthanum titanate, *Thermochimica Acta* **715** (2022) 179268. *doi: https://doi.org/10.1016/j.tca.2022.179268*

III. **Austėja Diktanaitė**, Giedrė Gaidamavičienė, Edvardas Kazakevičius, Algimantas Kežionis, Artūras Žalga, Aqueous sol-gel synthesis, thermal analysis, characterization, and electrical properties of V$_2$O$_5$ doped Bi$_2$O$_3$ system. *Thermochimica Acta*. Amsterdam: Elsevier. 2020, vol. **685**, art. no. 178511, p. [1-7]. *doi: https://doi.org/10.1016/j.tca.2020.178511*

Article not included in the thesis

Artūras Žalga, Giedrė Gaidamavičienė, Žygimantas Gricius, Emilija Užpurvytė, Jonas Gadeikis, **Austėja Diktanaitė**, Maud Barré, Tomas Šalkus, Algimantas Kežionis, Edvardas Kazakevičius, Aqueous sol-gel synthesis, thermoanalytical study and electrical properties of La$_2$Mo$_2$O$_9$, *Journal of Thermal Analysis and Calorimetry* 132(3) (2018) 1499–1511. *doi: https://doi.org/10.1007/s10973-018-7120-3*

Published contributions to academic conferences

1. **Diktanaitė Austėja**; Žalga Artūras, Sol- gel synthesis and thermoanalytical study of Li-Al-Mo-O tartrate gel precursors. COINS 2019 - 14th international conference of life sciences, [February 26-28, 2019, Vilnius, Lithuania] : abstract book. Vilnius : Vilniaus universiteto leidykla. 2019. p. 39.

2. **Diktanaitė Austėja**; Žalga Artūras, Aqueous sol-gel synthesis, structural and thermoanalytical study of a lithium lanthanum titanate ($Li_{3x}La_{2/3-x}TiO_3$, LLTO) solid electrolyte. Book of abstracts of the 5th Central and Eastern European Conference on Thermal Analysis and Calorimetry (CEEC-TAC5) and 14th Mediterranean Conference on Calorimetry and Thermal Analysis (Medicta2019). Rome : Central and Eastern European Committee for Thermal Analysis and Calorimetry (CEEC-TAC), 2019. p. 297.

3. **Diktanaitė Austėja**; Kazakevičius Edvardas; Žalga Artūras, Sol-gel synthesis and thermoanalytical study of $xBi_2O_3 \cdot V_2O_5$ ceramics. Book of abstracts of the 5th Central and Eastern European Conference on Thermal Analysis and Calorimetry (CEEC-TAC5) and 14th Mediterranean Conference on Calorimetry and Thermal Analysis (Medicta2019). Rome : Central and Eastern European Committee for Thermal Analysis and Calorimetry (CEEC-TAC), 2019. p. 296.

4. **Diktanaitė, Austėja**; Žalga, Artūras, Vibrational spectroscopic and X-Ray diffraction studies of lithium molybdates prepared by sol-gel method. Open readings 2015 : 58th scientific conference for students of physics and natural sciences, Vilnius, March 24-27 : programme and abstracts. Vilnius : Vilniaus universitetas. 2015. p. 146.

5. **Austėja Diktanaitė**, Artūras Žalga, Vibrational spectroscopic and X-Ray diffraction studies of lithium molybdates prepared by sol-gel method. 58th Scientific Conference for Students of Physics and Natural Sciences "Open Readings 2015", Vilnius, Lithuania.

6. **Austėja Diktanaitė**, Artūras Žalga, Synthesis and characterization of $LiAlMo_2O_8$ and $Li_3AlMo_3O_{12}$ ceramics. The Coins 2015 - International Conference of Natural and Life Sciences. 2015. Vilnius, Lithuania.

7. **Diktanaitė Austėja**, Žalga Artūras, Sol-gel synthesis and characterization of lithium aluminium molybdate. Chemistry and chemical technology 2015: international conference of Lithuanian Chemical Society, dedicated to Professor Vitas Daukšas on his 80th birth anniversary, Vilnius, Lithuania, 2 p. 78.

8. **Austėja Diktanaitė**, Artūras Žalga, Vibrational spectroscopic and X-ray diffraction studies of lithium molybdates prepared by sol-gel method. 58th

Scientific Conference for Students of Physics and Natural Sciences "Open Readings 2015", March 24-27, 2015 Vilnius, Lithuania.

9. **Austėja Diktanaitė**, Artūras Žalga, Synthesis and characterization of $LiAlMo_2O_8$ and Li3AlMo3O12 ceramics. The Coins 2015 - International Conference of Natural and Life Sciences. 3-7th March 2015. Vilnius, Lithuania.

10. **Diktanaitė Austėja**, Žalga Artūras, Sol-gel synthesis and characterization of lithium aluminium molybdate. Chemistry and chemical technology 2015: international conference of Lithuanian Chemical Society, dedicated to Professor Vitas Daukšas on his 80th birth anniversary, Vilnius, Lithuania, January 2 p. 78.

NOTES

NOTES